NUCLEAR MAGNETIC RESONANCE METHODS FOR CHARACTERIZATION OF BIOCHEMICAL TRANSFORMATIONS

A Dissertation

by

MENGXIAO LIU

Submitted to the Office of Graduate and Professional Studies of
Texas A&M University
in partial fulfillment of the requirements for the degree of

DOCTOR OF PHILOSOPHY

Chair of Committee,	Christian B. Hilty
Committee Members,	Simon W. North
	Renyi Zhang
	Joseph H. Ross Jr.
Head of Department,	Simon W. North

August 2019

Major Subject: Chemistry

ABSTRACT

As an analytical technique for structure determination and quantitative analysis, nuclear magnetic resonance (NMR) spectroscopy is widely used to characterize reactions or interactions. However, NMR is not readily applicable to probe fast processes because of its low sensitivity which requires long averaging time. This sensitivity issue can be solved using dissolution dynamic nuclear polarization (DNP), a hyperpolarization technique that enhances NMR signals by factors of 10^3 – 10^4. In this dissertation, DNP assisted NMR methods were developed to measure biochemical interactions and reactions on a rapid time scale, including protein-ligand interactions, enzymatic reactions, and in-cell metabolism. Through these measurements, information about kinetics and structures was obtained, which cannot be easily acquired through other methods. It was demonstrated that protein-ligand binding kinetics can be characterized rapidly by measuring relaxation dispersion from a single hyperpolarization. Moreover, the high sensitivity from DNP can reduce the acquisition interval to follow real-time biochemical reactions that complete within a few minutes. Modeling the time evolution of the reactant and product signals can result in detailed kinetic and relaxation parameters that contain structural information. In a reaction catalyzed by a metalloenzyme, the fitted relaxation rates due to paramagnetic relaxation enhancement (PRE) were used to calculate intermolecular distances in the enzyme-product complex structure, showing that real-time NMR together with PRE can be used to obtain kinetic and structural information simultaneously. Similar experiments are also applicable in live cells. An electroporator was hyphenated to facilitate the fast introduction of hyperpolarized precursors. Since arbitrary substrates can be introduced

into cells within the detection time window, DNP-NMR can be used to access a broader range of in-cell reactions or interactions. The reaction time resolution in real-time NMR is limited primarily by the signal acquisition time. In the final part of this thesis, it is shown on the example of an enzymatic reaction that, this limit can be overcome by imaging the entire reaction progress in a continuos-flow mode. The higher time resolution achieved by this method can be used to acquire the kinetic profile of short-lived reaction intermediates.

DEDICATION

To my mother and father.

ACKNOWLEDGEMENTS

I would like to express my sincere gratitude to my graduate advisor, Dr. Christian Hilty. His supervision guided me through the Ph.D. program. He introduced me to a new research area and helped me find projects of interest. When I had encountered tough problems in experiments, his broad knowledge and critical thinking always inspired a solution. His feedback constantly improved my skill sets and promoted my transition to a professional. He also offered me expert advice for my future career path.

I appreciate the suggestions and support from other committee members, Dr. Simon W. North, Dr. Renyi Zhang, and Dr. Joseph H. Ross Jr.

I am grateful to the degree program of the chemistry department. The curricular courses kept me in the right track of my Ph.D. study. The student seminars improved my ability in literature search and presentation. The preliminary exam helped me to find feasible projects. I remember the help from the staff members as well.

Thanks also go to my colleagues and friends. I could learn something from every one of them. Their genuine care and encouragement made the bad time hopeful.

Finally, I would like to thank my parents and boyfriend in China for their unconditional support and love. Without them being my secure base, I would not have the courage to explore a bigger world.

CONTRIBUTORS AND FUNDING SOURCES

Contributors

This work was supervised by a dissertation committee consisting of Professor Christian B. Hilty (Chemistry), Professor Simon W. North (Chemistry), Professor Renyi Zhang (Atmospheric Sciences and Chemistry) and Professor Joseph H. Ross Jr. (Physics) from the Texas A&M University.

In Section 2, the dual-channel NMR probe was built by Dr. Yaewon Kim. In Section 3, the hyperpolarized and thermal titration NMR experiments were performed by Dr. Youngbok Lee and Dr. Guannan Zhang, respectively; Dr. Nilkamal Mahanta provided the metalloenzyme and measured the isothermal titration calorimetry. In Section 5, Dr. Guannan Zhang assisted in the fabrication of the mixer device; the ultrafast imaging pulse sequence was set up by Michael Jaroszewicz from the Weizmann Institute of Science; Guannan Zhang and Jihyun Kim aided with the experiments.

All other work was performed by the student under the supervision of the committee chair, Professor Christian Hilty.

Funding Sources

The funding sources supporting this dissertation include National Institutes of Health (Grant R21-GM107927), the National Science Foundation (Grant CHE-0846402), the Welch Foundation (Grant A-1658), the Ji and Li Family Foundation, and the United States-Israel Binational Science Foundation (Grant 2014316).

NOMENCLATURE

1D	One-Dimensional
2D	Two-Dimensional
BAEE	N-α-Benzoyl Arginine Ethyl Ester
BBO	Broad-Band Observe
CNC	Computer Numerical Control
CPMG	Carr-Purcell-Meiboom-Gill
D-DNP	Dissolution Dynamic Nuclear Polarization
DMSO	Dimethyl Sulfoxide
DNP	Dissolution Dynamic Nuclear Polarization
DTPA	Diethylenetriamine Pentaacetic Acid
E.coli	Escherichia Coli
EG	Ethylene Glycol
EPSI	Echo Planar Spectroscopic Imaging
FID	Free Induction Decay
INPHARMA	Interligand NOE for Pharmacophore Mapping
MRI	Magnetic Resonance Imaging
NMR	Nuclear Magnetic Resonance
NOE	Nuclear Overhauser Effect
NOESY	Nuclear Overhauser Effect Spectroscopy
OD	Optical Density
OX063	tris[8-carboxyl-2,2,6,6-tetrakis[2-(1-hydroxethyl)]-benzo(1,2-d:4,5-d')bis(1,3)dithiole-4-yl]methyl free radical sodium salt

PDB	Protein Data Bank
PEEK	Polyether Ether Ketone
ppm	Parts Per Million
PRE	Paramagnetic Relaxation Enhancement
R_1	Longitudinal Relaxation Rate
R_2	Transverse Relaxation Rate
R5P	Ribose-5-Phosphate
RD	Relaxation Dispersion
RF	Radio Frequency
RNA	Ribonucleic Acid
SE	Standard Error
SNR	Signal-to-Noise Ratio
STD	Saturation Transfer Difference
TEMPOL	4-hydroxy-2,2,6,6-tetramethylpiperidine-1-oxyl
TFA	Trifluoroacetic Acid
TFBC	4-(trifluoromethyl)benzene-1-carboximidamide
TFE	Trifluoroethanol
TXI	Inverse Triple Resonance
UMP	Uridine 5'- Monophosphate
UV	Ultraviolet
UV-Vis	Ultraviolet–Visible
ΨMP	Pseudouridine Monophosphate
ΨMPG	Pseudouridine Monophosphate Glycosidase

TABLE OF CONTENTS

Page

LIST OF FIGURES

Page

LIST OF TABLES

Page

1. INTRODUCTION

Nuclear magnetic resonance (NMR) spectroscopy is an invaluable technique for structural elucidation and species quantitation. The NMR signal is sensitive to the chemical environment of the nuclear spin, which is reflected in different observables like the chemical shift, J-coupling, and spin relaxation.[1,2] The interpretation of NMR signals can yield highly detailed structural information, even including the stereochemical configuration and conformation.[3,4] NMR can also be used in quantitative analysis owing to the proportional relationship between the signal intensity and the concentration of a species.[5]

In addition to structural and quantitative analysis, NMR can characterize chemical transformation processes on different time scales.[6] The picosecond–nanosecond dynamics of molecular tumbling or internal motions can be probed by measurement of spin relaxation rates.[7,8] The chemical exchange kinetics occurring on the millisecond timescale can be measured by relaxation dispersion.[9] For reactions that occur within seconds to days, real-time NMR can be applied to sample the ongoing processes at different intervals, and yield the time profiles of reactions.[10]

Although NMR can provide rich information about chemical changes, it has an intrinsically low sensitivity that often requires averaging of multiple scans. Because of the averaging time, NMR cannot follow transient reactions or screen interactions rapidly. Recently, hyperpolarization techniques that can provide sensitivity enhancement by orders of magnitude have been developed.[11,12] Such techniques include, but are not limited to dynamic nuclear polarization (DNP),[13,14] parahydrogen induced polarization (PHIP),[15,16]

signal amplification by reversible exchange (SABRE),[17,18] and photochemically induced DNP (photo-CIDNP).[19–21] Coupled with a hyperpolarization technique, NMR can achieve rapid measurements, which is especially useful for monitoring non-equilibrium processes.

1.1. Overview of Basic NMR Theory

The NMR signal originates from the magnetization of nuclear spins. The spin magnetic moment can interact with an external magnetic field and result in energy level splitting due to the Zeeman effect.[22] The nuclei of commonly used isotopes in NMR, such as ^{1}H, ^{13}C, and ^{15}N, have a spin number *s* of 1/2. For *s* = 1/2, there are two energy levels, associated with the magnetic quantum number m_z, −1/2 and 1/2, respectively. The polarization, *P*, quantifies the population difference of the two energy levels, defined as

$$P = \frac{n_{-1/2} - n_{1/2}}{n_{-1/2} + n_{1/2}} \tag{1.1}$$

where $n_{-1/2}$ and $n_{1/2}$ are the corresponding numbers of spins.

The bulk nuclear spin magnetization in the NMR sample, *M*, is proportional to *P*.[23] The magnetization is aligned with the direction of the external magnetic field, which is defined as the z axis. In order to detect the magnetization of nuclear spins, a radio frequency pulse is used to generate a coherence, which results in nuclear spin magnetization precessing in the xy plane. A basic pulse sequence is depicted in Figure 1.1, where the experiment is repeated *n* times for signal averaging.

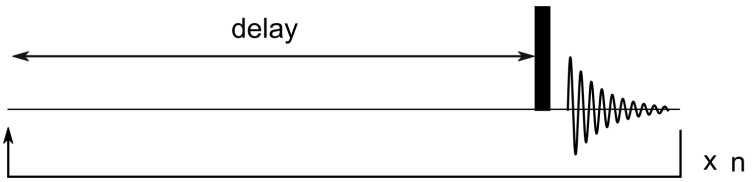

Figure 1.1. A basic pulse sequence for NMR measurement. The black rectangle denotes the radio frequency pulse, and the decaying wave form represents the acquired NMR signal. n is the number of averaging scans.

Nuclear spin relaxation characterizes the return of the magnetization to thermal equilibrium. The z-component of the magnetization, M_z, changes according to Equation 1.2.

$$M_z(t) = M_z^{eq} + \left[M_z(0) - M_z^{eq}\right] \times e^{-R_1 t} \tag{1.2}$$

Here, the superscript *eq* indicates the equilibrium level, and R_1 is the longitudinal or spin-lattice relaxation rate. Therefore, after the magnetization is depleted, a time delay on the order of $1/R_1$ is needed to regenerate M_z^{eq} (Figure 1.1). When the magnetization is precessing in the xy plane, M_{xy} decays as in Equation 1.3, where R_2 is the transverse or spin-spin relaxation rate.

$$M_{xy}(t) = M_{xy}(0) \times e^{-R_2 t} \tag{1.3}$$

1.2. Real-Time NMR of Non-Equilibrium Systems

Real-time NMR in the context of this dissertation refers to a series of NMR spectra that are measured during the occurrence of a chemical reaction or other change. It can track the reaction progress directly from the appearance and disappearance of resonance

signals. The mechanistic and kinetic analysis of real-time NMR signals facilitates the understanding of reaction processes.

1.2.1. Approaches to Measure Real-Time NMR

The simplest way to measure real-time NMR is to record a series of one-dimensional (1D) spectra *in situ* after the reaction starts. This method is usually applied when the reaction duration is long, from several tens of minutes to hours. Using this approach, the time interval between acquisitions is limited by the averaging time. As in Figure 1.1, a delay time is required in each averaging scan to allow for the generation of magnetization. The need for averaging depends on the concentration of the target species. High concentrations can afford smaller time intervals. More information about the chemical structures can be obtained from two-dimensional (2D) correlation spectroscopy, but the acquisition time is longer than for 1D measurements. To integrate 2D NMR into more rapid real-time monitoring, one of several techniques can be used, including a specially designed excitation scheme to rapidly regenerate the magnetization,[24] an ultrafast pulse sequence that spatially encodes the indirect spectral dimension using pulsed field gradient,[25] and compressed sensing that recovers signal from fewer data than Nyquist theory would dictate.[26,27]

When the desired time interval is smaller than the averaging time, NMR can be measured *ex situ* to sample the time course of the entire reaction progress. Aliquots are removed from the reaction mixture at different time points and then analyzed by NMR. This approach can be used when the reaction completes within a few minutes or longer. For example, in reference 28, a polymerization reaction was quenched at intervals of several tens of seconds to obtain the reaction kinetics.

When real-time NMR is measured *in situ*, there is a dead time after the mixing or the start of the reaction and prior to the NMR measurement. In order to measure rapid reactions *in situ* with a short dead time, the stopped-flow technique was introduced by Ernst and coworkers.[29] In this technique, different reactant solutions flow into a mixer, which is connected to a flow NMR tube. The flow is stopped after the mixture reaches the detection region, and the acquisition starts after a short delay time.[29–31] Therefore, the first measured reaction time point is determined by the transfer time from the mixer to the NMR tube, and the post-stop delay. By repeating the same experiment with varying delay time, the progress of a reaction can be monitored, such as the unfolding of a protein.[32] To capture the initial time points of rapid reactions, the dead time has to be minimized. The mixing volume can be reduced by maintaining turbulent flow.[30] In a recent application, Christianson and coauthors have achieved a dead time of about 35 ms using a rapid pneumatic injection system, and measured the initiation process of a polymerization reaction.[31]

Inhomogeneity in reaction rates may arise spatially when measuring the mixed samples, due to insufficient mixing or uneven temperature, which makes it difficult to obtain repeatable and accurate kinetic results. This difficulty can be circumvented by continuous-flow NMR experiments, in which data is acquired during the flow.[33,34] To control the temperature in these experiments, Foley *et al.* have reported a design of a flow NMR tube that can fit into a standard 5 mm NMR probe.[35] The assembly consisted of four concentric tubular channels. The inner two channels were used for the inflow and outflow of the reaction mixture, and the outer two for the flow of ethylene glycol to maintain the desired temperature.

Magnetic resonance imaging (MRI) provides spatial resolution in the monitoring of ongoing reactions. In addition to the ability to separate chemical components through the resonance frequency, MRI can image opaque samples in three dimensions, in a noninvasive way. Several applications to real-time NMR have been reported, such as in chemical reactors, polymerizations, and electrochemical processes.[36,37] For example, the MRI approach was used by Akpa and coauthors to visualize the distribution of reaction kinetics in heterogeneous catalysis.[38] As the reactant flowed through a fixed-bed reactor, two product species were formed. The imaging results showed different conversion rates and selectivity along the radial and axial directions. The smaller conversion rate near the reactor wall was found consistent with the faster flow rate towards the wall, which resulted in a shorter feed-catalyst contact time.[38] MRI can also resolve physical properties spatially, such as diffusion and relaxation. Relaxation weighted contrast of the solvent has been used as an indirect way to image the chemical waves from paramagnetic species.[39]

1.2.2. Mechanistic and Kinetic Analysis

Real-time NMR acquires reaction time profiles in combination with chemical shift resolution at the atomic level, which can facilitate insights into protein-folding, enzyme catalysis, polymerization, and organic reactions.[40–42] First, NMR signals that appear at different reaction time allow for conclusions on the reaction mechanisms.[43,44] Second, quantitative analysis of the time-dependent NMR signals offers information on reaction kinetics. To extract the kinetic parameters, fitting or modeling is often applied. In some cases, the reaction progress is simply linear with time. One example is an enzyme catalyzed reaction where the substrate concentration is comparably high relative to the Michaelis constant. In this situation, the slopes of substrate or product signals versus time

directly reflect the turnover number of the involved enzymes.[45] For photochemical reactions occurring in NMR tubes, the overall signals also change linearly with time, which can be used to determine the reaction rates and quantum yields.[46]

In a more complicated kinetic analysis, reaction orders can be determined from the time profiles or from the relationship between the initial reaction velocity and concentrations.[28,47,48] Activation energies can also be derived, by measuring the reaction rate constants at different temperatures.[47] Based on these kinetic results, reaction mechanisms can be proposed and verified. For example, in the copolymerization reaction of cyclohexene oxide and CO_2 catalyzed by a dizinc complex, the zeroth order dependence for CO_2 suggested that CO_2 inserts rapidly into the zinc-alkoxide bond in the catalyst.[47] The calculated activation energies were used to construct an energetic map for the polymer and a side product.[47] In another example of an aqueous free-radical polymerization, the reaction order for the initiator was found to be close to 0.5, in agreement with the classic initiation theory.[48]

1.3. Relaxation Methods to Probe Macromolecular Interactions with Small Molecules

The biological function of macromolecules often involves the interaction with small molecules that are known as ligands.[49] Protein-ligand interactions can be represented by a two-state reaction with no intermediate states.

$$P + L \underset{k_{\text{off}}}{\overset{k_{\text{on}}}{\rightleftharpoons}} PL \tag{1.4}$$

In the above model, P represents a protein, L is the ligand, and PL is the protein-ligand complex. k_{on} and k_{off} are the association and dissociation rate constants. The free ligand or

protein is in exchange with the bound complex. The exchange rate k_{ex} equals to $k_{on}[P] + k_{off}$ or $k_{on}[L] + k_{off}$ with respect to the ligand or the protein, respectively. There are three exchange regimes, separated by the relative magnitude of k_{ex} and the resonance frequency difference of the two states ($\Delta\nu$).[22] When the exchange is slow ($k_{ex} << \Delta\nu$), two resonance peaks will be observed for the two states. If $k_{ex} \approx \Delta\nu$, the exchange is on an intermediate time scale and the peaks coalesce. In the fast exchange regime ($k_{ex} >> \Delta\nu$), the two peaks collapse into a single peak. In the following subsections, relaxation based methods that can characterize protein-ligand interactions will be discussed.

1.3.1. Polarization Transfer

The magnetization of one spin affects nearby spins through the magnetic dipolar interaction, which can be described by the Solomon equations.[22]

$$\frac{d}{dt}\begin{bmatrix} S(t) - S^{eq} \\ I(t) - I^{eq} \end{bmatrix} = \begin{bmatrix} -\rho_S & -\sigma_{SI} \\ -\sigma_{IS} & -\rho_I \end{bmatrix}\begin{bmatrix} S(t) - S^{eq} \\ I(t) - I^{eq} \end{bmatrix} \tag{1.5}$$

S and I represent the magnetizations of the two spins, and ρ and σ are the auto and cross relaxation rates. This magnetization transfer is known as the nuclear Overhauser effect (NOE). The cross peaks in multi-dimensional NOE (NOESY) spectra can be used to identify the spins with polarization transfer.[50] The sign of the cross relaxation rate depends on the correlation time, which is related with the molecular size and local flexibility. When the small ligand molecule binds to a large macromolecule, positive cross peaks will be observed.[51] Based on this observation, protein-ligand interactions can be diagnosed. Since the dipolar relaxation mechanism shows a strong dependence on the distance between interacting spins, NOESY contributes to the structural determination of protein-ligand complexes.[50]

In addition to NOESY, saturation transfer difference (STD) is a polarization transfer method used to characterize protein-ligand interactions. In NMR, saturation is a way to achieve zero polarization. When a ligand binds to a protein, saturation applied selectively on the protein can diffuse rapidly across the entire bound complex. The saturation on the bound ligand spreads to the free ligand because of fast exchange, attenuating the overall ligand signal.[52] STD is measured as the signal difference without and with saturation. The STD intensity at different chemical shifts can be used to identify the interacting functional groups in the ligand. Quantitative information can be obtained from the complete relaxation and conformational exchange matrix analysis (CORCEMA).[52–54] In CORCEMA, NMR signals are simulated from relaxation rates and exchange parameters, such as ρ, σ, k_{on}, and k_{off} in Equations 1.4 and 1.5. CORCEMA can be used to analyze NOESY and other polarization transfer measurements. CORCEMA adapted for STD, for example, has found a much smaller k_{on} of trehalose-6-phosphate than that of trehalose when binding to a repressor protein, implying conformational rearrangement upon binding with the phosphate form.[55]

In NOESY and STD, polarization transfers through a single step between the protein and ligand. The transfer can be achieved via multiple steps as well. For example, in water-ligand observed via gradient spectroscopy (WaterLOGSY) experiments, the bulk water magnetization is first transferred to protein through NOE or proton exchange, and then to a ligand that binds to the protein. WaterLOGSY has been used as a method to screen protein-ligand interactions where ligand signals are observed.[56,57]

Polarization can also transfer consecutively from a ligand to the protein and then to a second ligand that competes to bind in the same binding pocket. Based on this protein-

mediated NOE between ligands, the INPHARMA approach (interligand NOE for pharmacophore mapping) has been developed by the Griesinger group.[58,59] With the known orientation of one ligand in the binding pocket, the binding epitope of the competitive ligand can be determined. In practice, the docking results that compute protein-ligand binding poses, are ranked by the experimental interligand NOEs using a full relaxation matrix calculation.[60] INPHARMA has aided the fragment-based drug design[61,62] and the analysis of binding epitopes in several protein-ligand systems.[63–65]

1.3.2. R_2 Relaxation Dispersion

To characterize protein-ligand interactions in the intermediate exchange regime, R_2 based relaxation dispersion can be used. The R_2 rate measured by the Carr-Purcell-Meiboom-Gill (CPMG) pulse sequence shows dispersion at different pulsing delays when the chemical environment of the spin exchanges.[9,66,67] When there are two exchanging states (A, B), the transverse magnetization M^+ evolves in accordance with the modified Bloch-McConnell equation.[68]

$$\frac{d}{dt}\begin{bmatrix} M_A^+(t) \\ M_B^+(t) \end{bmatrix} = \begin{bmatrix} -i\Omega_A - R_2^A - p_B k_{ex} & p_A k_{ex} \\ p_B k_{ex} & -i\Omega_B - R_2^B - p_A k_{ex} \end{bmatrix} \begin{bmatrix} M_A^+(t) \\ M_B^+(t) \end{bmatrix} \tag{1.6}$$

In the equation, Ω is the Larmor precession frequency, and p denotes the population of the two states.

The R_2 dispersion measurements are sensitive to minor populations,[69,70] enabling the usage of ligands that are in excess amount.[71] This has made ligand detection by carbon NMR at natural ^{13}C abundance possible.[72] In an application with ligand detection, the binding mechanism in an RNA-ligand system was derived from a relaxation dispersion

analysis.[73] Fitting the relaxation profiles to Equation 1.6 produced a smaller population of the bound ligand than calculated from the apparent dissociation constant (K_D), providing a strong evidence for the conformational selection mechanism.[73] In general, the apparent K_D equals to $\frac{k_{off}}{k_{on}} \times \frac{k_{-1}}{k_1+k_{-1}}$ in the induced fit model and $\frac{k_{off}}{k_{on}} \times \frac{k_1+k_{-1}}{k_1}$ in the conformational selection model, respectively.[74]

$$P + L \underset{k_{off}}{\overset{k_{on}}{\rightleftharpoons}} \underline{PL} \underset{k_{-1}}{\overset{k_1}{\rightleftharpoons}} PL \tag{1.7}$$

$$\underline{P} + L \underset{k_{-1}}{\overset{k_1}{\rightleftharpoons}} P + L \underset{k_{off}}{\overset{k_{on}}{\rightleftharpoons}} PL \tag{1.8}$$

In the induced fit model (1.7), the protein and ligand first bind into an intermediate state $\underline{PL}$, and then the binding pocket will adjust to form a more stable binding complex PL. In the conformation selection model (1.8), different conformations of the protein $\underline{P}$ and P are in a pre-equilibrium, and only P can bind with the ligand.

1.3.3. Paramagnetic Relaxation Enhancement

Paramagnetic species such as radicals and metal ions contain unpaired electrons. The magnetic moment of electron spins is about 1000 times larger than of nuclear spins, significantly affecting the fluctuation of magnetic fields at the location of nearby nuclei. Therefore, the relaxation rates of nuclear spins are dramatically enhanced in the presence of paramagnetic species. This paramagnetic relaxation enhancement (PRE) effect can reveal spatial proximity at a longer distance up to 35 Å than NOE (≤ 6 Å).[75–77]

Besides applications in the determination of distances, PRE has been applied in the characterization of protein-ligand interactions.[50,78] For example, PRE profiles have been exploited to identify the interplay between conformational selection and induced fit

in protein-ligand binding.[79] For enzymes containing paramagnetic metal ions in the binding pocket, the binding affinity of ligands can also be measured from the relaxation of the bulk solvent, since the interaction between the solvent and the paramagnetic site will be interrupted upon ligand binding.[80]

1.4. NMR Sensitivity and Dissolution DNP

1.4.1. NMR Sensitivity

The signal-to-noise ratio (SNR) in the measured NMR spectra is affected by polarization, frequency, noise levels, and other factors, as in Equation 1.9.[81]

$$SNR = K\eta NPu_z[n\,\mu_0 Q\omega_0 V_c/(4FkT_c\Delta f)]^{1/2} \tag{1.9}$$

In the expression, K is a numerical factor dependent on the receiving coil geometry, η is the filling factor, N is the spin density, P is the polarization, and $u_z = \hbar\gamma m_z$, where $\hbar$ is the reduced Planck constant and γ is the gyromagnetic ratio. n is the number of averaging scans, μ_0 is the magnetic constant, Q is the quality factor of the coil, $\omega_0 = \gamma B$ is the Larmor precession frequency. Here, B is the magnetic field strength. V_c is the coil volume, F is the noise figure of the preamplifier, T_c is the temperature of the probe not the sample, and Δf is the receiver bandwidth.

The detection sensitivity is related to the nuclear spin polarization P, which is defined in Equation 1.1. According to the Boltzmann distribution,

$$\frac{n_{1/2}}{n_{-1/2}} = e^{-\Delta E/(kT)} \tag{1.10}$$

where k is the Boltzmann constant, T is the temperature, and ΔE is the energy difference in Zeeman splitting.

$$\Delta E = \hbar \gamma B \tag{1.11}$$

Therefore, P can be calculated using the follow equation.

$$P = \frac{n_{-1/2} - n_{1/2}}{n_{-1/2} + n_{1/2}} = \frac{1 - e^{-\Delta E/(kT)}}{1 + e^{-\Delta E/(kT)}} \tag{1.12}$$

P is approximately equal to $\tanh\left(\frac{\Delta E}{2kT}\right)$ in the limit of very small ΔE.

^{1}H has the largest gyromagnetic ratio γ among the commonly used isotopes. For ^{1}H at 9.4 T, P is only 3.2×10^{-5} at room temperature. When measuring ^{1}H spectra, standard NMR probes usually require more than 250 μL of samples with a concentration preferably larger than 100 μM. For other NMR-active nuclei including ^{13}C and ^{15}N, the sensitivity is lower due to the smaller gyromagnetic ratios and the low natural abundance of the corresponding isotopes.

The sensitivity in NMR can be improved in several ways, as shown in Equation 1.9. In probe selection, a large filling factor is preferred. With respect to instrumentation, efforts have been made to increase the Q and reduce the F factors. By reducing the probe temperature T_c and the F factor, SNR can increase about 4 times with the use of a cryogenic probe.[82] P and ω_0 increase with the magnetic field strength B. Magnetic fields of 45 T dc and 100 T pulsed have been achieved by combining superconducting and resistive electro-magnets.[83,84] SNR also scales with the sample concentration and the square root of the number of scans.

1.4.2. Dissolution DNP

Dynamic nuclear polarization (DNP) is a hyperpolarization technique that can enhance the polarization level to the order of 10^{-1}. The sample is first mixed with a radical compound in a solvent that can form an amorphous solid after freezing. In a magnet at low temperature of several Kelvin or below, the polarization level of electrons is close to 1.[85] The sample is irradiated with microwaves, which results in a transfer of the high polarization of the electron spins to the nuclear spins. The primary mechanisms for this solid-state transfer have been identified, namely the solid effect, cross effect, and thermal mixing.[86]

Dissolution DNP was reported by Ardenkjær-Larsen *et al.* in 2003.[14] After polarization in solid state, the sample is dissolved by a pre-heated dissolution solvent. Finally, the collected solution is rapidly transferred to the NMR probe in a second magnet for liquid-state experiments. The signal enhancement can be calculated as the SNR improvement factor, compared to the measurement from thermal NMR that uses polarization established under thermal equilibrium. Using dissolution DNP, a signal enhancement of > 10,000 can be achieved.[14] Applications of dissolution DNP have been exploited broadly in *in vivo* imaging, monitoring metabolism and rapid reactions, and characterizing protein interactions. Thorough reviews of these categories can be found in references 87–89.

The polarization generated by dissolution DNP decays to the thermal equilibrium level because of the R_1 relaxation (Equation 1.2). Researchers have used various ways to preserve the high polarization from D-DNP. To minimize the transfer time of the dissolved sample, the Hilty lab has developed automatic injectors interfaced with a dissolution DNP

instrument. Using the driving force from a high-pressure gas or liquid, the total time for dissolution and sample delivery has been reduced to less than 2 s.[90,91] To prevent the paramagnetic relaxation, the radicals used in the polarization process can be removed by a reduction reaction,[92] filtration,[93] or extraction via phase separation.[94] An alternative way to produce pure radical-free sample solutions is to generate the radicals *in situ* by UV light. These photo-induced radicals will recombine during dissolution.[95] The relaxation becomes faster when the hyperpolarized sample transfers through the low magnetic field. A magnetic tunnel can be used around the passage of the dissolved sample to alleviate this effect.[96]

1.5. Real-Time NMR Using Dissolution DNP

1.5.1. Real-Time DNP-NMR Measurement

The signal enhancement from DNP allows to split the large magnetization into multiple spectra by a series of small flip angle pulses, as shown in Figure 1.2. Compared to thermal NMR (Figure 1.1), a delay time for polarization regeneration is not needed between successive scans. This enables real-time NMR to monitor reactions that complete within seconds to minutes. Moreover, the sample concentrations can be much lower compared to thermal NMR measurements.

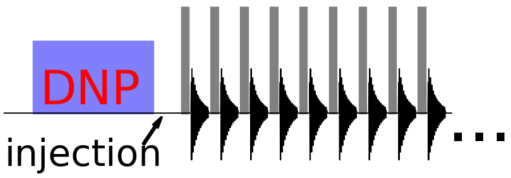

Figure 1.2. Pulse diagram of real-time DNP-NMR. The gray rectangles represent a series of small flip angle pulses.

1.5.2. Modeling of Real-Time DNP-NMR Signals

Modeling the time profile of the hyperpolarized signals aims to separate the effects of kinetics, relaxation, radio frequency pulses, and non-instantaneous mixing. Here, modeling is illustrated on the example of a simple reaction scheme.

$$R \overset{k}{\rightarrow} P \tag{1.13}$$

where R converts to P, in a first-order process with a rate constant k.

When only the reaction kinetics and relaxation are considered, the measured hyperpolarized signals follow

$$\frac{dS(t)}{dt} = KS(t) \qquad S(t) = \begin{bmatrix} S_R(t) \\ S_P(t) \end{bmatrix} \qquad K = \begin{bmatrix} -(k + r_R) & 0 \\ k & -r_P \end{bmatrix} \tag{1.14}$$

In this matrix representation, r_R and r_P denote the R_1 relaxation rates. The sum of relaxation rate and self-consumption kinetic rate constants occupies the diagonal position of the matrix K. The off-diagonal elements are the conversion rate constants to other species. Because of the hyperpolarized signal is much larger than the thermal signal, the thermal signal is neglected.

The magnetization attenuated by the small flip angle (α) pulse can be accounted for by multiplying with $\cos\alpha$ after each scan. After the p^{th} pulse at time t_p, the signals will become $(\cos\alpha)^{p-1}e^{\mathrm{K}t_p}S(0)$.[100] The pulse effect can also be treated as an additional relaxation rate, $-ln(\cos\alpha)/\Delta\mathrm{t}$, where $\Delta\mathrm{t}$ is the pulse interval.[99,100] When α is small, $-ln(\cos\alpha)/\Delta\mathrm{t}$ approximates to $(1-\cos\alpha)/\Delta\mathrm{t}$.[101,102]

In experiments where the injection is not rapid compared to the reaction, the injection process can be broken down into piecewise equations.[103,104] Decomposition of the overall signal into individual components is sometimes needed before the kinetic fitting. For example, the measured signal during protein folding can be reconstructed to the folded and unfolded components.[103]

The kinetic results using different models have been compared.[105,106] Without prior knowledge of reaction models, the reaction rate can also be evaluated in a model-free way, using the ratio of the under-curve areas or numerical integration.[107,108] The relationship between the rate constant k and the signal integrals has been derived as[108]

$$k = r_P \frac{\int_0^\infty S_P(t)dt}{\int_0^\infty S_R(t)dt} \tag{1.15}$$

The modeling outcomes contribute to the understanding of underlying reaction processes. For example, V_{max} and K_m in the Michaelis-Menten kinetics were obtained by modeling the metabolism of hyperpolarized pyruvate in human breast cancer cells.[101] The values were found typical of the monocarboxylate transporter 1, indicating that the introduction of pyruvate into the glycolytic pathway is the rate-limiting step.[101] In another example of a polymerization reaction, a better fitting result was achieved using a model with a deactivation step, which suggests the involvement of a deactivation process.[100]

DNP-NMR can obtain the kinetic profiles and determine reaction mechanisms simultaneously. Spin manipulations such as selective inversion[109] and continuous saturation during acquisition[110] can be used to follow the fate of the atoms carrying hyperpolarized spins in the reactions.[99] When the resonance peak of one atom position is

selectively inverted or saturated, peak inversion or attenuation will appear at positions where this atom goes. For example, in the polymerization of styrene, the living anionic species was identified through the J-coupling pattern and the inversion manipulation.[111]

1.6. Characterization of Protein-Ligand Interactions Using Transferred Hyperpolarization

Dissolution DNP imposes a dramatic population shift from the thermal equilibrium. The hyperpolarized spin can significantly increase the NMR signal of nearby spins via the cross relaxation mediated polarization transfer. This can be seen from the Solomon Equations 1.5. Therefore, several methods have been developed to utilize transferred hyperpolarization to characterize protein-ligand interactions.

The intermolecular NOE that arises due to protein-ligand interactions can be measured rapidly with signal enhancement by dissolution DNP. Wang and coauthors have reported the measurement of this NOE between the hyperpolarized ligand folic acid and the protein dihydrofolate reductase.[112] Using a single quantum coherence transfer, the ^{1}H spectra selected at different ^{13}C chemical shifts were measured. The spectra coincided with the isotope filtered NOESY spectra, and the enhanced methyl peaks agreed well with the spatial proximity in the crystal structure of the protein-ligand complex.[112] Using the same system, the protein peaks showed different enhancement profiles when proton signals from different ligand positions were inverted selectively.[113] In combination with CORCEMA analysis, these profiles can be used to rank the generated poses for the binding pocket from a docking program.[113]

Frequency profiles representing the protein-ligand interaction, similar to those obtained from STD experiments can be measured in a single scan with dissolution DNP.

Min *et al.* showed that the single-scan profile of the enhanced protein signal closely matched the STD intensity measured conventionally by sweeping the selective saturation frequencies.[114] The experiment demonstrated that dissolution DNP provides a rapid approach to measure the polarization transfer process.[114]

Water is the primary solvent for biochemical systems and can be hyperpolarized as the source spin reservoir for polarization transfer. Hyperpolarized water can increase the sensitivity in WaterLOGSY experiments, and the enhanced protein signal offers a way to examine if the protein is denatured.[115] The hyperpolarization of water can also be used to probe protein-water interactions.[116] Through chemical exchange, amide protons in the protein can acquire a high polarization level from the hyperpolarized water, which can be further transferred to other protons in proteins via cross relaxation. The exchange and cross relaxation rates have been determined by modeling the time-dependent proton signals in the amide and aliphatic regions.[116]

The INPHARMA experiment can be performed with hyperpolarized ligands as well. Using this method, Lee and coworkers have observed protein mediated interligand hyperpolarization transfer and derived that the signal intensity of the non-hyperpolarized ligand depends on the mixing time and cross relaxation rates.[117]

2. DETERMINATION OF CHEMICAL EXCHANGE USING RELAXATION DISPERSION OF HYPERPOLARIZED NUCLEAR SPINS[1]

Chemical exchange phenomena are ubiquitous in macromolecules, which undergo conformational change or ligand complexation. NMR relaxation dispersion (RD) spectroscopy based on a Carr-Purcell-Meiboom-Gill pulse sequence is widely applied to identify the exchange and measure the life time of intermediate states on the millisecond time scale. Advances in hyperpolarization methods improve the applicability of NMR spectroscopy when rapid acquisitions or low concentrations are required, through an increase in signal strength by several orders of magnitude. Here, we demonstrate the measurement of chemical exchange from a single aliquot of a ligand hyperpolarized by dissolution dynamic nuclear polarization (D-DNP). Transverse relaxation rates are measured simultaneously at different pulsing delays by dual-channel ^{19}F NMR spectroscopy. This two-point measurement is shown to allow the determination of the exchange term in the relaxation rate expression. For the ligand 4-(trifluoro-methyl)benzene-1-carboximidamide binding to the protein trypsin, the exchange term is found to be equal within error limits in neutral and acidic environments from D-DNP NMR spectroscopy, corresponding to a pre-equilibrium of trypsin deprotonation. This finding illustrates the capability for determination of binding mechanisms using D-DNP RD. Taking advantage of hyperpolarization, the ligand concentration in the exchange

[1] Adapted with permission from "Liu, M.; Kim, Y.; Hilty, C. Characterization of Chemical Exchange Using Relaxation Dispersion of Hyperpolarized Nuclear Spins. Anal. Chem. 2017, 89 (17), 9154–9158.".[118] Copyright (2019) American Chemical Society.

measurements can reach on the order of tens of μM and protein concentration can be below 1 μM, *i.e.* conditions typically accessible in drug discovery.

2.1. Introduction

Macromolecular functions, including ligand binding, signal transduction, and protein-protein interactions, often rely on dynamic properties of the molecules.[119–121] For ligand binding, the conformational selection or induced fit model, for example, accounts for changes that need to take place prior to or during binding. Nuclear magnetic resonance (NMR) spectroscopy is used extensively to characterize these and other dynamic processes involving both large and small molecules in solution. Owing to the long nuclear spin decoherence time, characteristic time constants such as those governing chemical exchange can be determined under equilibrium up to the second time scale.[74,119,122] In an intermediate exchange regime, where the exchange rate is approximately equal to the difference in resonance frequencies of the two exchanged states ($k_{ex} \approx \Delta\nu$), a measurement of relaxation dispersion (RD) using Carr-Purcell-Meiboom-Gill (CPMG) pulse sequences yields information on minor molecular conformations that are not directly observable.[123–125] Kay and co-workers have applied the RD measurements to study a series of invisible or excited protein conformations.[66,69,126–129] In addition to the conformational change of one macromolecule, binding interactions can also be quantitatively analyzed through the exchange between bound and free states using the RD method.[74,130,131] Binding mechanisms can then be distinguished by comparing intrinsic dissociation constants $K_{D,i} = k_{off} / k_{on}$, which can be determined from RD, with apparent K_D measured by other techniques.[73,74,131–133] In general, simple two-state, conformational selection and induced fit mechanisms follow $K_{D,i} = K_D$, $K_{D,i} < K_D$, and $K_{D,i} > K_D$ respectively.[74] In contrast to

protein-detected RD measurements, recently developed ligand-detected RD experiments[72,73,134,135] do not require protein labeling, and protein concentrations can be low compared to ligand concentrations. ^{13}C ligand-detected RD at natural abundance has been demonstrated to be viable.[72] Such RD measurements have been proposed for use in drug discovery, because the obtained exchange rates directly reflect the life time of the drug – target complex.[73] Drug discovery applications in particular are subject to stringent limitations on the sample amounts and time available, which are not always compatible with the requirements for NMR experiments. Hyperpolarization methods can in principle be used to increase the NMR signal, and thus would reduce both the needed sample concentration and averaging time. Dissolution dynamic nuclear polarization (D-DNP) offers signal gains of up to four orders of magnitude in a single NMR scan.[14] Meanwhile, the inherent single scan nature of this technique combined with the time required to hyperpolarize each sample presents its own challenges to obtain multiple measurements at different pulsing delays required for RD.

Here, we describe a method for a two-point RD measurement using a single sample of a ligand hyperpolarized by D-DNP in parallel NMR detection channels. Applied to the protein trypsin and a ligand, we illustrate that this experiment allows the measurement of the exchange contribution to the transverse relaxation rate R_2 of the ligand, leading to determination of the binding mechanism.

2.2. Experimental Section

2.2.1. Hyperpolarization

For hyperpolarization, 10 μL aliquots containing 7 mM 4-(trifluoromethyl) benzene-1-carboximidamide hydrochloride hydrate (TFBC·HCl; Maybridge, U.K.) were

prepared in D_2O/dimethyl sulfoxide (DMSO)-d_6 (v/v = 1:1) solvent, which is glass forming when frozen, with 15 mM 4-hydroxy-2,2,6,6-tetramethylpiperidine-1-oxyl (TEMPOL; Sigma-Aldrich, St. Louis, MO). These aliquots were hyperpolarized on ^{19}F in a HyperSense DNP polarizer (Oxford Instruments, Abingdon, U.K.), by irradiation with 100 mW of 94.055 GHz microwaves for 20 min, at a temperature of 1.4 K.

2.2.2. Sample Injection

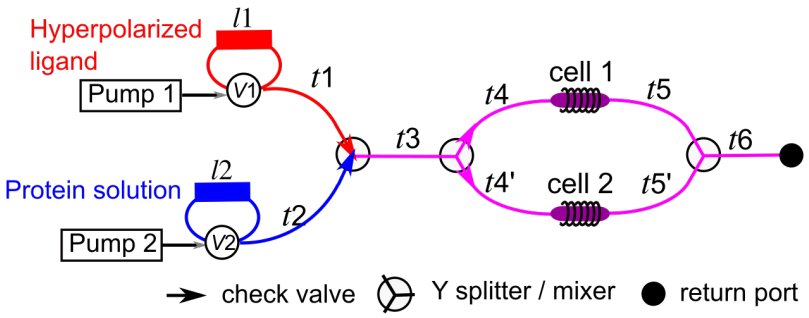

Figure 2.1. Schematic of injection pathway. *V*1 and *V*2 are two-position valves. *l*1 and *l*2 are the sample loops for hyperpolarized ligand and protein solution, respectively. Four check valves were installed at the Y connectors to prevent unwanted sample motion. Tubing lengths: *t*1, 152.4 cm; *t*2, 5 cm; *t*3, 30 cm; *t*4 / *t*4', 60 cm; *t*5 / *t*5', 60 cm; *t*6, 170 cm. Tubing inner diameters: *t*1, *t*2, *t*3 and *t*4 / *t*4', 0.5 mm; *t*5 / *t*5' and *t*6, 0.76 mm. Flow rates: Pump 1, 160 mL·min^{-1}; Pump 2, 120 mL·min^{-1}. Reprinted with permission from [118].

300 µL of trypsin (AMERSCO, Road Solon, OH) solutions of 2 and 4 µM in 50 mM tris(hydroxy-methyl)aminomethane buffer at pH 8, or of 4 and 10 µM in 50 mM acetate buffer at pH 5 were pre-loaded into a sample loop *l*2 (Figure 2.1) of a stopped-flow injection device.[91,136] Subsequently, hyperpolarized ligand was dissolved in 4 mL buffer that had been pre-heated until reaching a vapor pressure of 5 bar. This dissolution buffer was of the same composition as that used for preparation of trypsin samples, at pH

5 or pH 8. The dissolved ligand sample was collected in the injection loop *l*1. Two high-pressure syringe pumps (Models 500D and 1000D, Teledyne Isco, Lincoln, NE) filled with distilled water and connected to injection valves *V*1 and *V*2 (DL8UWTI, VICI Valco, Houston, TX) were then used to drive the protein and ligand samples through a mixer and a subsequent splitter into the flow cells of a two-channel flow NMR probe. The outflows from the flow cells converged at another mixer and returned to the switch valve *V*1. After injection, these valves were switched to the original positions to stop flow, and 400 ms later the NMR measurement was triggered.

Dilution factors during sample injection were measured prior to DNP experiments, using 500 mM trifluoroethanol (TFE) and 15 mM trifluoroacetic acid (TFA) as reference compounds, with the same trypsin concentration and dissolution buffer for each experimental condition. TFE solution was loaded into the DNP polarizer, and TFA solution with trypsin was loaded into the sample loop *l*2. After dissolution, NMR spectra were acquired to quantify TFA and TFE concentrations. It was found that TFBC and trypsin were diluted around 200 and 7–8 fold respectively. These dilution factors were used to calculate the final concentrations $[TFBC]_0$ and $[trypsin]_0$ in the flow cell in the DNP experiments.

2.2.3. NMR Experiments

The NMR experiments were measured using a homebuilt two-channel ^{19}F NMR spectroscopy. The design of the NMR probe was previously described.[136] The solenoids of the probe were tuned to 376.4 MHz for the ^{19}F resonance frequency at a magnetic field of 9.4 T. The probe was inserted into a commercial NMR magnet with shim system (Bruker Biospin, Billerica, MA). Dry air regulated by a temperature controller (Air Jet,

SP Scientific, Warminster, PA), was flowed through the probe to maintain a temperature of 299 K during the experiments. Probe temperature was monitored using a thermocouple placed 5 cm below the bottom coil. A two-channel spectrometer incorporating radio frequency pulse generation and acquisition boards (PulseBlasterDDS and RadioProcessor, SpinCore Technologies, Gainesville, FL) and power amplifiers (BT00100 and BT00250 GAMMA, Tomco Technologies, Stepney, Australia) was used for simultaneous spectrum acquisition.

The pulse sequence in Figure 2.2 was designed for simultaneous two-point relaxation dispersion measurements from one hyperpolarized sample, employing two separate CPMG pulse trains. To avoid contamination of the measured signals in one channel by the excitation pulse from the other channel, the 180° pulse and acquisition time in the two channels were aligned. The 180° pulse intervals τ_{cp} in two channels was determined by τ, the half-echo time of the short pulsing channel and n, the number of iterations for the internal loops. For the hyperpolarized NMR experiments, $\tau_{cp} = 2\tau = 300$ μs was used in the short pulsing Channel 2. n was set as 9, making $\tau_{cp} = 2\tau \times (2n+1) = 5700$ μs in the long pulsing Channel 1. The 90° pulse length was calibrated as 11.5 μs. The 180° pulse length was included in the delay time τ_{cp}. The total numbers of spin–echoes that were measured were 1052 and 19988 in Channels 1 and 2, respectively ($m = 1052$, $m\times(2n+1) = 19988$), resulting in an NMR experiment time of 6 seconds. One single data point was acquired within each echo during a delay of 100 μs.

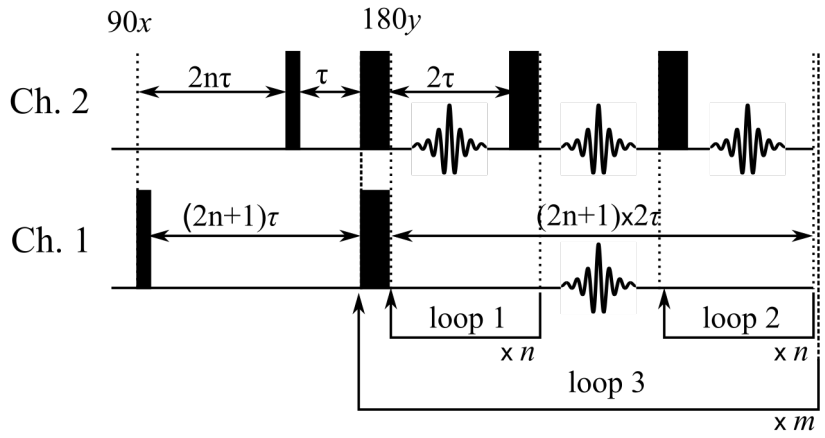

Figure 2.2. Pulse sequence used for simultaneous two-point relaxation dispersion measurements. The pulsing delay in Channel 1 is (2n+1) times longer than Channel 2. Reprinted with permission from [118].

Full relaxation dispersion curves were obtained from non-hyperpolarized samples at higher concentrations (3.5 – 31 μM trypsin containing 10 mM of TFBC), by applying an identical CPMG pulse sequence to both channels. R_2 values were measured at τ_{cp} of 300, 600, 1200, 2400, 4800 and 9600 μs.

Dissociation constants of trypsin and TFBC were determined by ^{19}F NMR titration experiments without hyperpolarization, using concentrations $[TFBC]_0$ = 16, 8, 4, 2, 1 and 0.5 mM and $[trypsin]_0$ = 50 μM at pH 8 or $[trypsin]_0$ = 100 μM at pH 5. In all the titration experiments, TFA in D_2O was used as an external resonance frequency reference. Since the resonance frequency of free TFBC varies at different concentrations, free TFBC of the same concentration was measured as a second reference.

2.2.4. Data Analysis

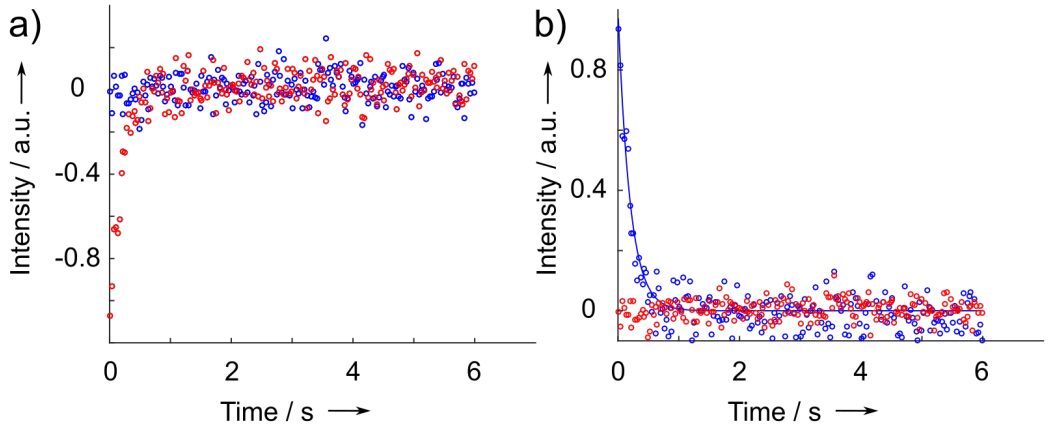

Figure 2.3. Determination of R_2 from central points of spin echoes. a) Raw time domain points with real (blue) and imaginary (red) parts. b) Signals after a phase correction to maximize the real (blue) part and minimize the imaginary part (red). A single exponential fit (blue line) was applied to the real part to obtain the R_2 relaxation rate, $R_2 = 5.3\ s^{-1}$. Reprinted with permission from [118].

For all CPMG experiments, data retrieved from the spectrometer was analyzed with Matlab (MathWorks, Natick, MA). After a phase correction was applied to maximize the real part and minimize the imaginary part, a single exponential function was fitted to the real part to obtain R_2. Since only one data point could be acquired at the center of each spin echo in the experiment with short τ_{cp}, the R_2 relaxation rates were determined from the central points of the spin echo for all experiments (Figure 2.3). Additional data points could be obtained within one spin echo in the experiment with long τ_{cp}. The signal-to-noise ratio of the latter data sets can be improved by approximately 3-fold when all the data points from one echo are Fourier transformed and peak integration is used (Figure 2.4). However, the obtained R_2 values may vary depending on the window function and

number of points used in the integration, and these effects would need to be determined separately.

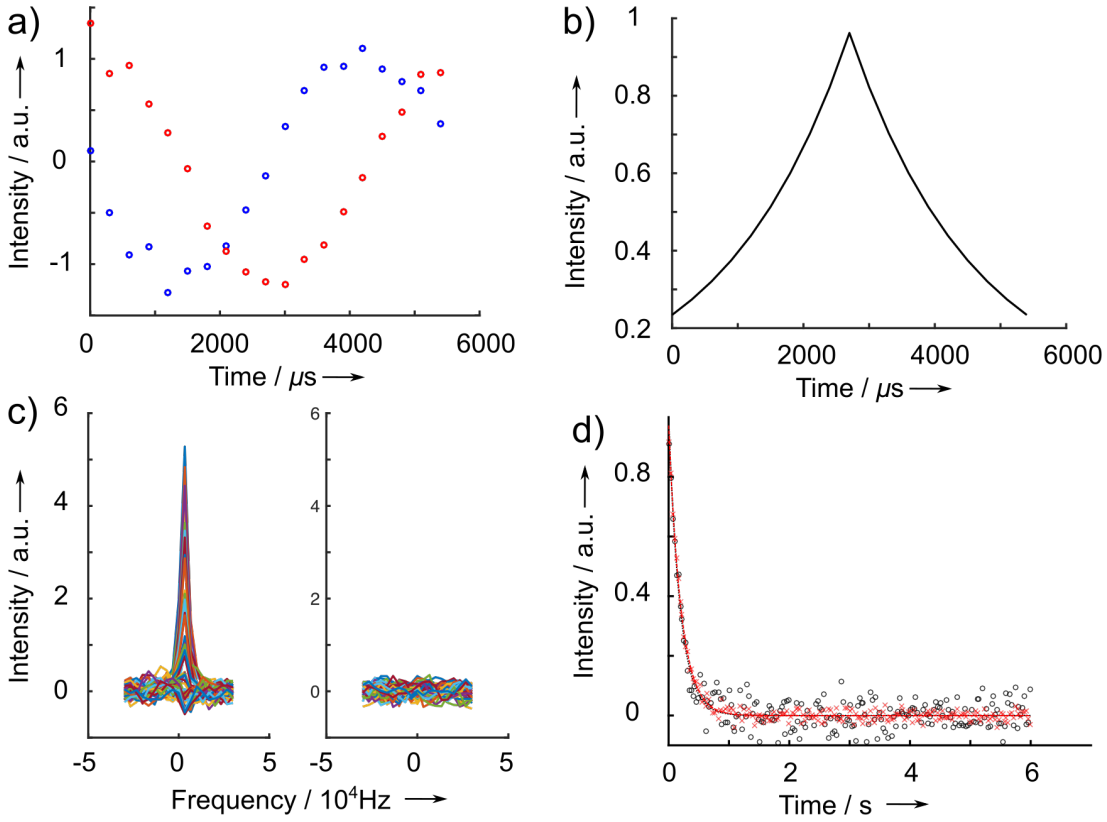

Figure 2.4. Alternative determination of R_2 using Fourier transform of time domain data points. This method is applicable to data sets with long τ_{cp}. a) Raw FID with real (blue) and imaginary (red) parts within one spin echo of Channel 1. b) Exponential window function that is multiplied before Fourier transform. c) Fourier transformed spectra. Since the time-domain data is symmetric, phasing is performed to maximize the real peak (left) and minimize the imaginary peak (right). Every 20th echo is shown. d) Data points from peak maxima processed as in (c) (red 'x') compared with the central points of each echo processed as in Figure 2.3b (black 'o'). The signal-to-noise ratio in the data from peak maxima is increased due to the inclusion of the additional time domain data points. Fitting of single exponential curves resulted in $R_2 = 4.9$ s^{-1} for the data from peak maxima (red dashed curve), compared to $R_2 = 5.3$ s^{-1} for the data from single points (black dotted curve). Intensities on the vertical axis are scaled to equal initial value based on the fitted curves. Reprinted with permission from [118].

To determine the dissociation constants of the trypsin-TFBC complex, changes of the line width and resonance frequency in the titration experiment were fitted to $\Delta LW = X_b \cdot \Delta LW_{max}$ and $\Delta \nu_{obs} = X_b \cdot \Delta \nu_{max}$, with fit parameters K_D to calculate X_b (bound fraction of the ligand), as well as ΔLW_{max} (line width change extrapolated to $X_b = 1$) and $\Delta \nu_{max}$ (resonance frequency change extrapolated to $X_b = 1$).[137] The full relaxation curves at each pH, parametrized by R_{2b}, $\Delta \nu$, and τ_b, were fitted to Equation 2.1 in Section 2.3.2 by constrained minimization in Matlab. X_b and X_f in Equation 2.1 were calculated from K_D and known concentrations. Constraints included two additional equations relating the three fit parameters based on the titration experiments.

2.3. Results and Discussion

2.3.1. R_2 Measurements Using the Hyperpolarized Ligand

The R_2 relaxation rates of the hyperpolarized ligand TFBC in the presence of the target protein trypsin were measured simultaneously in the flow cells of the two-channel NMR probe, at a short and a long CPMG pulse interval. Figure 2.5a shows the intensities obtained at the center of every echo from channels 1 and 2 in the experiment carried out at pH 8. Since a single hyperpolarized aliquot of the ligand was split and injected symmetrically into the corresponding flow cells, a difference in decay rates is expected primarily because of the different pulse intervals. The more rapidly decaying signal from Channel 1 corresponds to the slower refocusing rate (longer τ_{cp}), giving rise to more coherence loss during the chemical exchange between free and bound ligands. The experiment was further conducted at pH 5 using the same ligand and protein concentrations loaded into the instrument as in the case of pH 8 (Figure 2.5b).

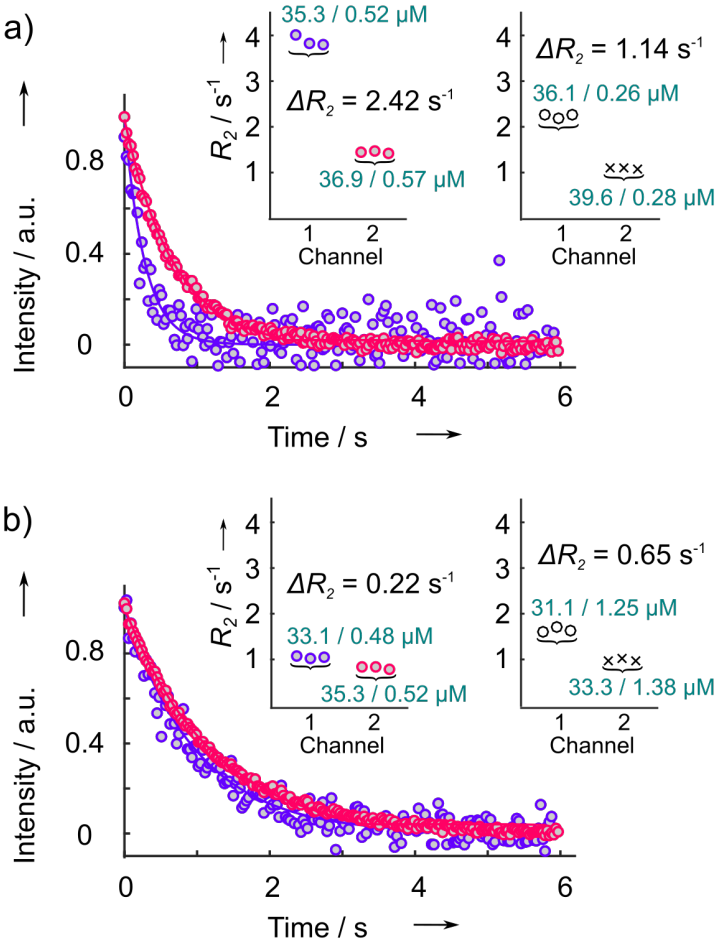

Figure 2.5. Simultaneous measurements of R_2 relaxation at (a) pH 8 and (b) pH 5 using long and short pulse delays. Blue and red colored '○' represent the real parts of the data points after phasing obtained from Channel 1 (τ_{cp} = 5700 µs) and Channel 2 (τ_{cp} = 300 µs) respectively. Shown data points are averages within 0.03 s intervals. R_2 relaxation rates were obtained from a fit to a single exponential; (a) blue curve, $R_2 = 3.82 \pm 0.50$ s^{-1}; red curve, $R_2 = 1.46 \pm 0.03$ s^{-1}; (b) blue curve, $R_2 = 1.04 \pm 0.06$ s^{-1}; red curve, $R_2 = 0.78 \pm 0.01$ s^{-1}. Errors indicate 90% fit confidence intervals. Average values from three measurements are 3.88, 1.46, 1.04, and 0.82 s^{-1}, respectively. The insets display the fitted R_2 values from three repetitions at pH 8 in (a) and pH 5 in (b), using two different protein concentrations. The colored data points represent the results from the shown relaxation data. The uncolored open '○' and '×' represent the results from the measurements using a different trypsin concentration. The concentrations $[TFBC]_0$ / $[trypsin]_0$ are indicated for each set of points. Reprinted with permission from [118].

Comparing these data, a pH dependence of R_2 relaxation is clearly seen. At pH 8, a larger change in R_2 is observed, while at pH 5 the two decay curves are almost overlapped and decaying more slowly. A priori, the smaller R_2 at lower pH can be explained by either a smaller fraction of the bound ligand or a reduced exchange contribution to the relaxation rate (see below). Results from three repetitions of the experiments are shown in the insets in Figure 2.5, as well as in Table 2.1. On average, $\Delta R_2 = R_2(\text{Channel 1}) - R_2(\text{Channel 2})$ obtained from the three nominally identical repetitions is 2.42 ± 0.14 s^{-1} and 0.22 ± 0.05 s^{-1} at pH 8 and 5, respectively (compare colored '○' in the insets in Figure 2.5a and b). A second set of measurements at a different trypsin concentration is shown with uncolored symbols in the insets. The final concentrations of $[\text{TFBC}]_0$ and $[\text{trypsin}]_0$ indicated in the figure were calculated using pre-determined dilution factors for each sample condition (see Section 2.2.2). These dilution factors were approximately 200 for the ligand component and 7–8 for the protein component, and varied by less than 10 % due to experimental errors (see Table 2.1).

Table 2.1. Relaxation rates from different sample conditions. Standard errors from three repetitions are indicated. Final TFBC and trypsin concentrations were calculated from sample dilution factors determined in injections of reference compounds. Reprinted with permission from [118].

pH	Condition	Channel	$[TFBC]_0$ / µM	$[trypsin]_0$ / µM	R_2 / s^{-1}
8	(1)	1	36.1 ± 3.5	0.26 ± 0.01	2.24 ± 0.04
		2	39.6 ± 3.5	0.28 ± 0.01	1.10 ± 0.01
	(2)	1	35.3 ± 2.8	0.52 ± 0.04	3.88 ± 0.12
		2	36.9 ± 2.8	0.57 ± 0.01	1.46 ± 0.03
5	(3)	1	33.1 ± 1.4	0.48 ± 0.03	1.04 ± 0.03
		2	35.3 ± 2.2	0.52 ± 0.03	0.82 ± 0.04
	(4)	1	31.1 ± 2.8	1.25 ± 0.08	1.65 ± 0.05
		2	33.3 ± 2.1	1.38 ± 0.04	1.00 ± 0.03

As seen in Figure 2.5, the signal-to-noise ratio (SNR) is lower in Channel 1 compared to Channel 2 because fewer echoes are acquired during the fixed experimental time. In principle, the SNR in Channel 1 could be improved by approximately three-fold, if multiple data points per echo would be used for this slower echo train (Figure 2.4). However, this would require different methods for analyzing the echo trains from the two channels, which was not preferred here for reasons of consistency.

2.3.2. Chemical Exchange between Free and Bound Ligand at Different pH

In the intermediate exchange regime, the R_2 dependence on the pulsing delay τ_{cp} in the CPMG pulse sequence can be explicitly described by Equation 2.1, when the concentration of the bound ligand is much smaller than the free ligand.[130]

$$R_2 = X_f R_{2f} + X_b/(1/R_{2b} + \tau_b) + X_b X_f \tau_b (2\pi\Delta\nu)^2 [1 - (2\tau_b/\tau_{cp})\tanh(\tau_{cp}/2\tau_b)] \quad (2.1)$$

R_{2f} and R_{2b} are the R_2 relaxation rates of the free and bound ligand, respectively. X_f and X_b = 1 – X_f represent the free and bound fractions of the ligand. τ_b is the life time of the protein-bound ligand complex. $\Delta\nu$ is the resonance frequency difference of the free and bound ligands. At the slow pulsing limit ($\tau_{cp} \rightarrow \infty$), $R_2 \rightarrow X_f R_{2f} + X_b/(1/R_{2b} + \tau_b) + X_b X_f \tau_b (2\pi\Delta\nu)^2$, while at the fast pulsing limit ($\tau_{cp} \rightarrow 0$), $R_2 \rightarrow X_f R_{2f} + X_b/(1/R_{2b} + \tau_b)$. The difference in R_2 from the two limits is equal to $X_b X_f \tau_b (2\pi\Delta\nu)^2$ which includes the exchange term $\tau_b(2\pi\Delta\nu)^2$.

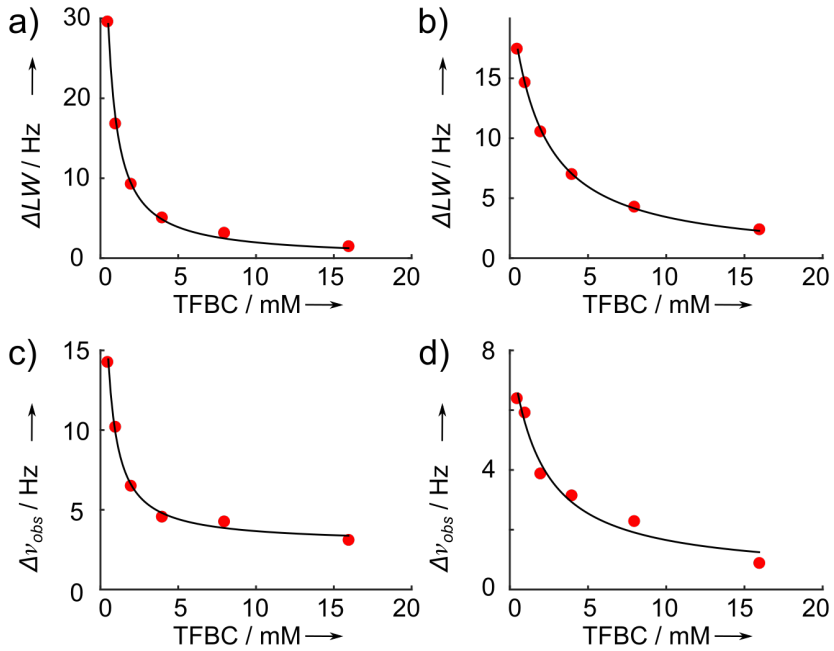

Figure 2.6. Non-hyperpolarized titration experiments to determine K_D of TFBC-trypsin. a) Observed changes in line width (ΔLW) at pH 8. b) Changes in line width at pH 5. c) Resonance frequency change ($\Delta\nu_{obs}$) of the ^{19}F peak of TFBC from the same experiment as in (a), at pH 8. d) Resonance frequency change at pH 5. Fit values with 90 % confidence intervals are: K_D = (168 ± 33) µM, ΔLW_{max} = (401 ± 18) Hz and $\Delta\nu_{max}$ = (160 ± 21) Hz at pH 8; K_D = (1730 ± 92) µM, ΔLW_{max} = (403 ± 14) Hz and $\Delta\nu_{max}$ = (168 ± 14) Hz at pH 5. Reprinted with permission from [118].

The τ_{cp} values of 300 and 5700 μs in the two-point RD measurement using D-DNP were chosen to approximate the two pulsing limits, and therefore $\Delta R_2 \approx \tau_b X_b X_f (2\pi\Delta\nu)^2$. In this case, X_b and X_f can be determined based on K_D, which is often known for a protein of interest. Here, K_D = 0.17 and 1.7 mM at pH 8 and 5, respectively, were determined from non-hyperpolarized titration experiments using a single π/2 pulse (Figure 2.6). Based on these K_D values and the measured ΔR_2, $\tau_b(2\pi\Delta\nu)^2$ were calculated. Despite more than a 10-fold difference between the ΔR_2 values measured at pH 8 and 5, the values of $\tau_b(2\pi\Delta\nu)^2$ are equal within the error limits of all four conditions measured (Table 2.2). Since $\Delta\nu_{max}$ is the same within error limits at pH 8 and 5 (Figure 2.6), the life time of the bound complex τ_b, *i.e.* the chemical exchange dynamics, is found to be the same within measurement uncertainty at the two pH.

Table 2.2. Exchange terms $\tau_b(2\pi\Delta\nu)^2$ determined from simultaneous two-point RD measurements using D-DNP. X_b is calculated with known values of $[TFBC]_0$, $[trypsin]_0$ and K_D. Standard deviations are calculated from three repetitions. Reprinted with permission from [118].

pH	X_b	$\tau_b(2\pi\Delta\nu)^2$ / s^{-1}
8	$1.31 \cdot 10^{-3}$	875 ± 43
	$2.67 \cdot 10^{-3}$	912 ± 53
5	$2.84 \cdot 10^{-4}$	788 ± 154
	$7.47 \cdot 10^{-4}$	881 ± 31

2.3.3. Binding Equilibrium of TFBC and pK_a Determination

Upon changing pH by 3 units, the binding affinity for trypsin and TFBC varies 10-fold (Figure 2.6), while the chemical exchange dynamics remains the same (Table 2.2).

These characteristics can be rationalized by a pre-equilibrium of protonated and deprotonated forms of trypsin, where only the deprotonated form interacts with TFBC (Scheme 2.1).

Scheme 2.1. Binding equilibrium of TFBC and trypsin. Pr^-, PrH, L^+ and PrL represent negatively charged trypsin, protonated trypsin, positively charged TFBC and TFBC-trypsin complex respectively. Pr^- is the active form that binds with L^+ (positively charged TFBC). K_a is the acid dissociation constant of PrH and $K_{D,i} = k_{off} / k_{on}$ is the intrinsic dissociation constant of PrL.

$$PrH + L^+ \overset{K_a}{\leftrightarrow} Pr^- + H^+ + L^+ \overset{K_{D,i}}{\longleftrightarrow} PrL + H^+$$

This scheme is supported by the fact that the binding of benzamidine and trypsin occurs through the formation of a salt bridge between the amidinium cation of benzamidine and the negatively charged carboxyl group of Asp 189 which is the substrate binding site in trypsin.[138,139] A similar binding interaction is expected for the TFBC used here, since it is a para-substituted benzamidine with a trifluoromethyl group and its amidinium cation is intact. Because the pK_a of TFBC is 11.0 (Figure 2.7), more than 99 % of TFBC is positively charged at both pH 8 and 5, *i.e.* $[L^+] \approx [L]_0$. Therefore, protonation of the ligand does not need to be considered. The pK_a of the pre-equilibrium stage can thus be estimated based on the binding equilibrium determined from the two-point RD measurement. From Scheme 2.1, $pK_a = \text{pH} + \log_{10}([PrH]/[Pr^-])$ and the term $[PrH]/[Pr^-]$ can be expressed in a relationship between the intrinsic $K_{D,i}$ and K_D. The difference between these values is that the concentrations of both protonated and deprotonated free trypsin are considered in $K_D = [L^+]([Pr^-]+[PrH])/[PrL]$, whereas $K_{D,i} = [L^+][Pr^-]/[PrL]$ only includes the active deprotonated form of free trypsin. From these equations, $pK_a =$

pH + $\log_{10}$ ($K_D/K_{D,i}$ – 1). When K_D values from the titrations are substituted into the prior equation, pK_a = 6.0 ± 0.3 and $K_{D,i}$ = 0.17 ± 0.02 mM are found. At pH 8, nearly 100% of trypsin is negatively charged, and $K_{D,i}$ is close to K_D. For comparison, the pK_a value for Asp 102, which is at the catalytic site of trypsin near Asp 189, was previously reported as 6.8.[139]

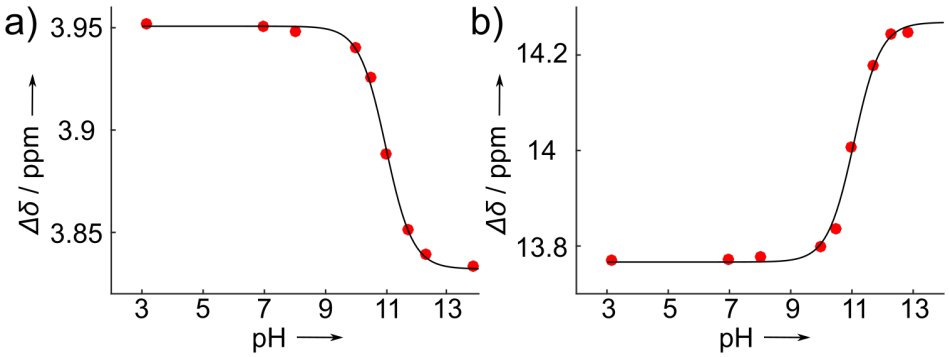

Figure 2.7. Measurement of pK_a of TFBC. a) ^{1}H peak shift. b) ^{19}F peak shift. TFE in D_2O was used as external reference. By fitting the Henderson-Hasselbach equation,[140] pK_a = 10.97 from ^{1}H curve and 11.07 from ^{19}F curve. Reprinted with permission from [118].

2.3.4. Supporting Measurements without Hyperpolarization

To validate the results obtained from the hyperpolarized two-point RD measurements, additional RD experiments were performed with non-hyperpolarized samples. The concentration of TFBC was increased by ~280-fold and the concentration of trypsin was increased by ~60- and 7-fold at pH 8 and 5, respectively. These sample concentrations were chosen to have similar bound complex fractions and SNR as the DNP experiments, while allowing measurement by 8 averaging scans. The experiments were performed at six different τ_{cp} values, applied simultaneously to both channels. The R_2

values measured from four different samples as a function of τ_{cp} are shown in Figure 2.8a and b. Using Equation 2.1, the data points from the same pH were fitted to a single set of parameters R_{2b}, τ_b, and $\Delta\nu$. Constraints from the titration experiments (Figure 2.6) were included in the fitting, since $\pi \cdot \Delta LW_{max} = R_{2b} + \tau_b(2\pi\Delta\nu)^2$ and $\Delta\nu_{max} = \Delta\nu \,/\, [(1+R_{2b}\tau_b)^2 + \tau_b^2(2\pi\Delta\nu)^2]$ when $X_b \sim 0$.[29] From the fitted τ_b value, $k_{on} = 1/(\tau_b K_{D,i}) = 1.9 \cdot 10^7$ $M^{-1} \cdot s^{-1}$, can further be calculated, which is within the range of the diffusion limit for protein-ligand binding.[132]

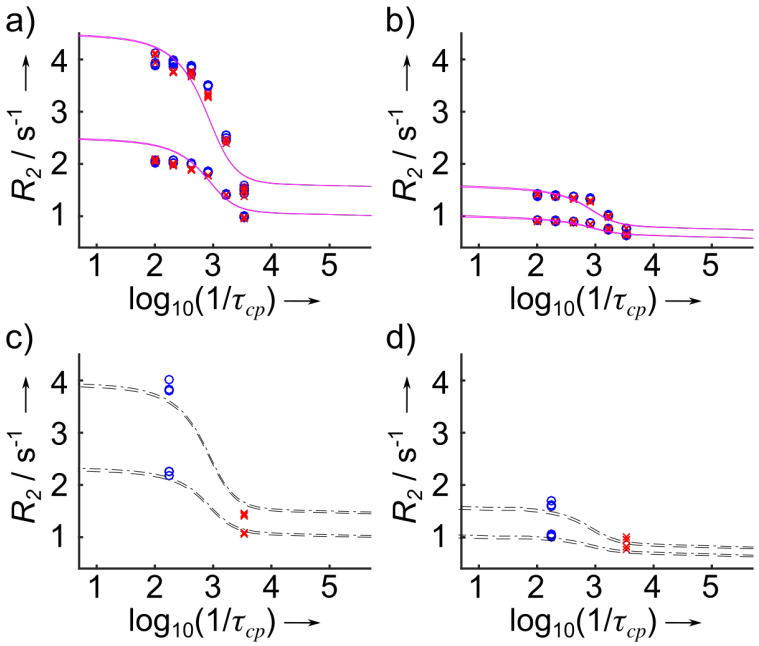

Figure 2.8. Relaxation dispersion measurements at pH 8 (a,c) and 5 (b,d). '○', data points from Channel 1; '×', data points from Channel 2. a) and b), five repetitions of non-hyperpolarized measurements with 8 scans at different τ_{cp} with fitted dispersion curves. c) and d), three repetitions of simultaneous two-point measurement from DNP measurements with calculated dispersion curves (--, Channel 1; -·-, Channel 2). Non-hyperpolarized sample concentrations: $[TFBC]_0$ = 10 mM, $[trypsin]_0$ = 15 / 31 µM at pH 8, and $[trypsin]_0$ = 3.5 / 8.8 µM at pH 5. Parameters obtained from fitting are R_{2b} = 461 s^{-1}, τ_b = 3.2 $\cdot 10^{-4}$ s, and $\Delta\nu$ = 251 Hz at pH 8; R_{2b} = 472 s^{-1}, τ_b = 3.0 $\cdot 10^{-4}$ s, and $\Delta\nu$ = 259 Hz at pH 5. Reprinted with permission from [118].

Based on these fitted parameters, R_2 dispersion curves were calculated for the sample conditions in the DNP experiments, and overlaid with the measured data points in Figure 2.8c and d. These curves are in good agreement with the R_2 values measured by DNP. The fitted exchange terms $\tau_b(2\pi\Delta\nu)^2$ = 798 and 794 s^{-1} at pH 8 and 5, respectively, are also comparable to those obtained from DNP (Table 2.2). Additionally, it can be seen that the τ_{cp} values chosen in the DNP experiments indeed approximate the long and short pulsing limits of the CPMG sequence.

2.3.5. Discussion

Using D-DNP, it was possible to reduce the final protein concentrations in the relaxation dispersion experiments into the sub-micromolar range, and ligand concentration was approximately 35 μM. These concentrations should alleviate solubility constraints in screening applications. Due to dilution during the liquid driven injection, the concentrations of samples are higher when loaded into the polarizer. This requirement can typically be met by preparing aliquots for hyperpolarization in DMSO or DMSO/H_2O based glassing solvents, which increase the solubility of ligands. The dissolution into aqueous buffer after hyperpolarization then sufficiently reduces the concentration to achieve aqueous solubility, even for ligands that may be difficult to dissolve in water at concentrations that would be required for non-hyperpolarized experiments. DNP of the ^{19}F nuclei provided a polarization enhancement of ~1500 fold compared to thermal polarization in a 400 MHz NMR magnet. In order to obtain the same SNR as in the DNP experiment but without hyperpolarization, a sample made in a standard 5 mm NMR tube from the amount loaded into the DNP polarizer (70 nmol) would require 26,000 averages,

and a sample at the final concentration after dilution (35 μM) in the flow cell would require 650,000 averages.

Dual-channel NMR spectroscopy allows a two-point RD measurement using DNP hyperpolarized samples, which was shown here to be sufficient for the determination of an exchange term. The RD measurements of TFBC-trypsin binding illustrate the ability to determine a binding mechanism based on the measured exchange dynamics. Specifically, they support a conformational selection mechanism with the deprotonated trypsin in pre-equilibrium, which is also reflected in that the dissociation constants $K_D > K_{D,i}$ at acidic pH. The DNP RD measurements were performed at two different pH, which changes the populations of protonated and deprotonated forms. In general, determination of a binding mechanism that does not depend on pH can be achieved by instead measuring RD at several different τ_{cp} values to access full dispersion curves under a single condition, from which on-and off rates for the ligand can be calculated.[73] Here, the relaxation decay was measured without spectral resolution since TFBC only shows one fluorine signal, although NMR spectra with low spectral resolution could be obtained in the long pulsing channel from Fourier transform of each echo (Figure 2.4). It would be possible to obtain full spectral resolution with a constant-time CPMG experiment, which is also compatible with the D-DNP experiment. This experiment gives access to the signal intensity after a constant CPMG time, without measuring each echo.[123,141] With the same dual-channel instrumentation used here, data for four or more τ_{cp} values can be measured from two or more hyperpolarized aliquots. Further, it would be possible to increase the number of simultaneous measurements from a single hyperpolarized sample through the development of detection hardware with additional channels.

2.4. Conclusion

A hyperpolarized relaxation dispersion experiment was shown to enable the determination of chemical exchange dynamics. To this end, two-point CPMG RD measurements were performed from a single hyperpolarized aliquot, using dual-channel ^{19}F NMR spectroscopy. For binding of the ligand TFBC to the protein trypsin, the exchange term contributing to transverse relaxation was found to be the same at pH 8 and pH 5. This result is explained by a pre-equilibrium of protein deprotonation, and illustrates the ability to evaluate protein–ligand binding mechanisms by this method. Based on the binding equilibrium, the overall pK_a of the binding pocket was further determined using apparent dissociation constants. While the fluorine nucleus used here is abundant in artificial drugs, the same method is applicable to the detection of other nuclei. The reduction in sample amount or averaging time more generally permits the determination of binding mechanisms by hyperpolarized RD under typical experimental conditions used in drug discovery experiments.

3. MEASUREMENT OF KINETICS AND ACTIVE SITE DISTANCES IN METALLOENZYME USING PARAMAGNETIC NMR WITH ^{13}C HYPERPOLARIZATION[2]

Paramagnetic relaxation enhancement (PRE) conjoint with hyperpolarized NMR reveals structural information on the enzyme-product complex in an ongoing metalloenzyme catalyzed reaction. Substrates of pseudouridine monophosphate glycosidase are hyperpolarized using the dynamic nuclear polarization (DNP) method. Time series of ^{13}C NMR spectra are subsequently measured with the enzyme containing diamagnetic Mg^{2+} or paramagnetic Mn^{2+} ions in the active site. The differences of the signal evolution and line widths in the Mg^{2+} *vs.* Mn^{2+} reactions are explained through PRE in the enzyme-bound product, which is in fast exchange with its free form. Here, a strong distance dependence of the paramagnetically enhanced relaxation rates enables the calculation of distances from product atoms to the metal center in the complexed structure. The same method can be used to add structural information to real-time characterizations of chemical processes involving compounds with naturally present or artificially introduced paramagnetic sites.

[2] Adapted with permission from "Liu, M.; Zhang, G.; Mahanta, N.; Lee, Y.; Hilty, C. Measurement of Kinetics and Active Site Distances in Metalloenzymes Using Paramagnetic NMR with ^{13} C Hyperpolarization. *J. Phys. Chem. Lett.* **2018**, *9* (9), 2218–2221.".[142] Copyright (2019) American Chemical Society.

3.1. Introduction

Structural properties, including of complexed and non-equilibrium configurations, play a pivotal role in biological functions of macromolecules. Conventional nuclear magnetic resonance (NMR) spectroscopy has long been applied to probe molecular structures that are revealed in observables such as chemical shift, scalar coupling, dipolar coupling, and relaxation.[22,76] However, due to an intrinsically low sensitivity of NMR, often the signal detection is limited to proton nuclei and equilibrium conditions that permit signal averaging. Given these factors, hyperpolarization techniques, especially dissolution dynamic nuclear polarization (D-DNP)[14] are increasingly applied to provide NMR signal enhancement of several orders of magnitude. D-DNP has been demonstrated for applications including real-time investigation of enzymatic reactions,[143] screening of protein-ligand interactions, and structural characterizations of a ligand binding pocket.[144] Hyperpolarization by D-DNP offers the possibility to detect ^{13}C spectra at natural abundance. The ability to monitor reactions is enhanced by the large chemical shift dispersion of this nucleus, as well as in some cases by its comparatively low relaxation rates.

For the determination of molecular structures, the nuclear Overhauser effect (NOE) based on dipolar interactions between nuclear spins is traditionally used to identify distances shorter than approximately 6 Å. In the presence of paramagnetic centers, distance determinations that rely on the paramagnetic relaxation effect (PRE) have a significantly extended range of up to ~35 Å.[75,77,145,146] Paramagnetic NMR has the capability of determining macromolecular interactions and structures such as of lowly populated intermediates, which are not easily accessible through other NMR techniques.[75]

While paramagnetic NMR is often applied in combination with labels that are specifically introduced into biomolecular samples, the technique can be used to characterize metalloproteins that naturally contain paramagnetic metal ions.[147,148] The metal ion cofactor is normally located in a binding pocket and is essential for the biological function. Mechanistic or functional information is therefore potentially available from paramagnetic NMR. In some cases, this technique can also be applied to metalloproteins naturally containing diamagnetic ions, upon substitution with a paramagnetic counterpart. Substitutions of the metal ion in the active site of metalloenzymes have widely varying effects.[149] Isoenzymes employing different metals can be expressed alternatively in some organisms, depending on environmental conditions.[150] For example, pseudouridine monophosphate glycosidase (ΨMPG) is a metalloenzyme that is functionally activated with several metal ions, such as Mn^{2+}, Fe^{2+}, Co^{2+}, and Mg^{2+}.[151] In bacteria, including in *Escherichia coli*, the enzyme reversibly catalyzes the cleavage of the C–C glycosidic bond in pseudouridine monophosphate (ΨMP), thereby recycling pseudouridine, the most abundant nucleoside in RNA modifications.[152]

Here, we demonstrate the application of D-DNP to obtain information derived from paramagnetic NMR in enzymatic reactions observed in real time. Using the combined chemical specificity and real-time capability offered by ^{13}C-NMR of hyperpolarized substrates, we differentiate the effect of paramagnetic and diamagnetic metal ion substitutions in ΨMPG. Through a quantitative analysis of both NMR intensities and line widths, we simultaneously determine kinetic and nuclear spin relaxation rate constants. Examining enhanced R_1 and R_2 relaxation values of carbon nuclei in the reaction

product, we obtain long-range distance information of enzyme–product complex with a new approach of paramagnetic NMR using ^{13}C hyperpolarization.

3.2. Experimental Methods

3.2.1. Hyperpolarized NMR Experiments.

The metalloenzyme pseudouridine monophosphate glycosidase (ΨMPG) was expressed and purified as previously described,[151] and then complexed with the metal ion Mg^{2+} or Mn^{2+} with a 1:1 ratio. Absorbance at 280 nm (A_{280}) was measured in a NanoDrop UV-Vis spectrophotometer (ThermoFisher Scientific, Waltham, MA) to determine the stock enzyme concentration. For the concentration determination, an extinction coefficient of 9,970 M^{-1} cm^{-1} was obtained from the ExPASy ProtParam tool using the primary sequence of the protein.[153]

For the substrate hyperpolarization, a 30 μL solution of 21 mM 4,5-$^{13}C_2$-uracil (Cambridge Isotope Laboratories, Tewksbury, MA), 375 mM ribose-5-phosphate (R5P), and 454 mM acetone was prepared in ethylene glycol/H_2O (3:2, v/v) with 15 mM sodium salt of tris[8-carboxyl-2,2,6,6-tetrakis[2-(1-hydroxethyl)]-benzo(1,2-*d*:4,5-*d*′)bis(1,3)di-thiole-4-yl]methyl free radical (OX063; Oxford Instruments, Abingdon, U.K.) and 1 mM diethylenetriamine pentaacetic acid gadolinium complex (Gd-DTPA; Sigma-Aldrich, St. Louis, MO). The sample was hyperpolarized in a HyperSense system (Oxford Instruments, Abingdon, U.K.) by irradiating 60 mW 93.974 GHz microwaves at 1.4 K in a 3.35 T magnetic field for 3 hours, and subsequently dissolved in 4 mL preheated Tris buffer (50 mM Tris(hydroxymethyl)-aminomethane hydrochloride, 50 mM sodium chloride; pH 7.5). The dissolved substrate solution was rapidly injected into a 5 mm NMR tube inside the magnet[3] and mixed with preloaded ΨMPG-Mg^{2+} or -Mn^{2+} solution (1 mM,

1.5 mM, or 2.2 mM). After mixing, the final concentrations of uracil and R5P were 560 μM and 10 mM, respectively. The enzyme was diluted to 56 μM, 83 μM, or 120 μM in the separate experiments. These concentrations were calculated based on known dilution factors, which were determined from test injections.

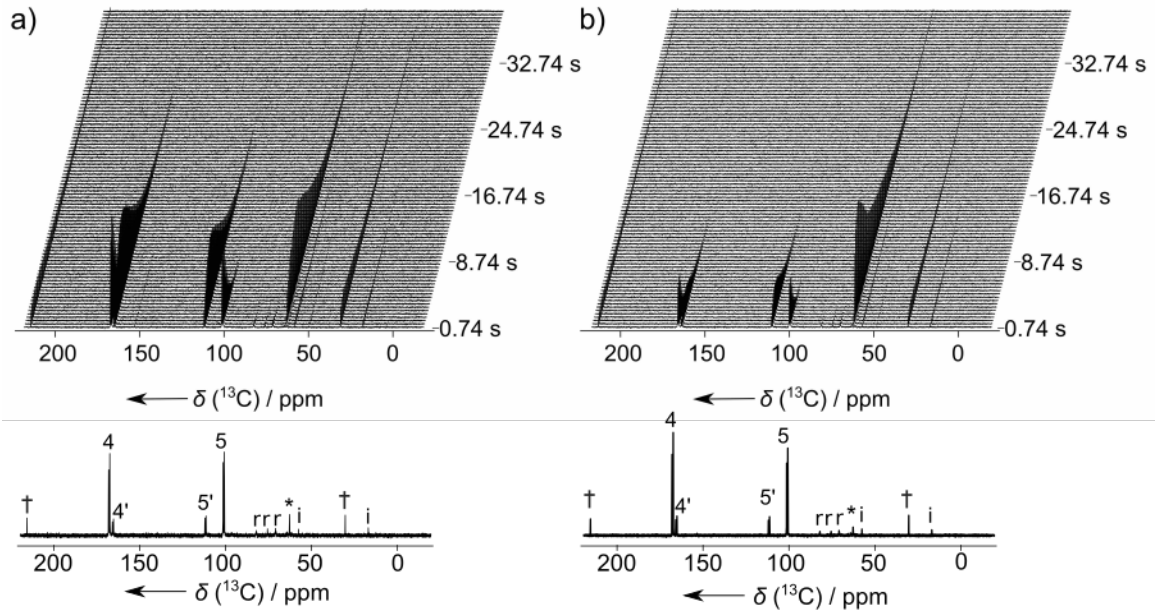

Figure 3.1. Stacked plots of the time series of ^{13}C spectra from hyperpolarized uracil and R5P mixture under the catalysis of a) ΨMPG-Mg^{2+} and b) ΨMPG-Mn^{2+}. The spectrum from the first scan is shown enlarged below each time series. Peaks from ^{13}C labeled positions, 4 and 5 in the reactant uracil as well as 4' and 5' in the product ΨMP are labeled. Peaks from hyperpolarized R5P at natural ^{13}C isotope abundance are labeled with 'r', visible below 100 ppm. '†' represents peaks of the internal reference acetone. '*' indicates the peak of the glassing solvent ethylene glycol used for DNP polarization. Peaks labeled with 'i' are from ethanol, a common impurity in R5P. Reprinted with permission from [142].

For each hyperpolarized NMR experiment, a series of ^{13}C NMR spectra (Figure 3.1) was acquired on a 400 MHz NMR spectrometer equipped with a broad-band observe (BBO) probe (Bruker Biospin, Billerica, MA) at the room temperature 298 K. The pulse

sequence consisted of elements trigger – $(P_1 – G_1)_3$ – $[\alpha_x$ – acquire – $G_z]_{\times 96}$. The selective $\pi/2$ pulse P_1 (EBURP shape, 10 ms and centered at 62.7 ppm) was followed by a pulsed field gradient G_1 (28 G/cm, 29 G/cm, 68 G/cm along x, y, z directions applied simultaneously; 1 ms) to suppress the ethylene glycol peak. α_x was an excitation pulse with the flip angle $\pi/18$ and the pulse strength $\gamma B_1/(2\pi)$ = 27.8 kHz. Proton decoupling was applied during acquisition. A total of 96 transients were acquired at an interval of 400 ms. Each transient was acquired for 340 ms with 16384 data points, after which a randomized pulsed field gradient G_z (1 ms) was applied to remove the residual coherence. Enhancements were calculated by comparing hyperpolarized spectra with non-hyperpolarized reference spectra of 730 mM ^{13}C labeled sodium acetate.

3.2.2. Supporting Measurements

An ITC measurement was carried out to measure the dissociation constant of ΨMPG-Mn^{2+}, using a MicroCal Auto-iTC_{200} instrument (Malvern Instruments, Malvern, UK). 50 mM Tris-HCl, pH 7.5 buffer was used in all the solutions. 50 μM ΨMPG was incubated with 1mM R5P at room temperature for half an hour to equilibrate. The mixture was centrifuged to discard any precipitate, and ~ 300 μL supernatant was placed in the sample cell with water in the reference cell. A stirring syringe containing 80 μL of 500 μM $MnCl_2$ was used to titrate the enzyme sample at a rate of 2 μL / injection, with a stirring speed of 1000 rpm for ~ 20 times. Standard setup conditions were used: 25 ˚C cell temperature, 10 μcal·s^{-1} reference power, 150 s injection interval, 5 s filter period, and high gain. The dissociation constant of ΨMPG-Mn^{2+} was determined as 5 μM (Figure 3.2).

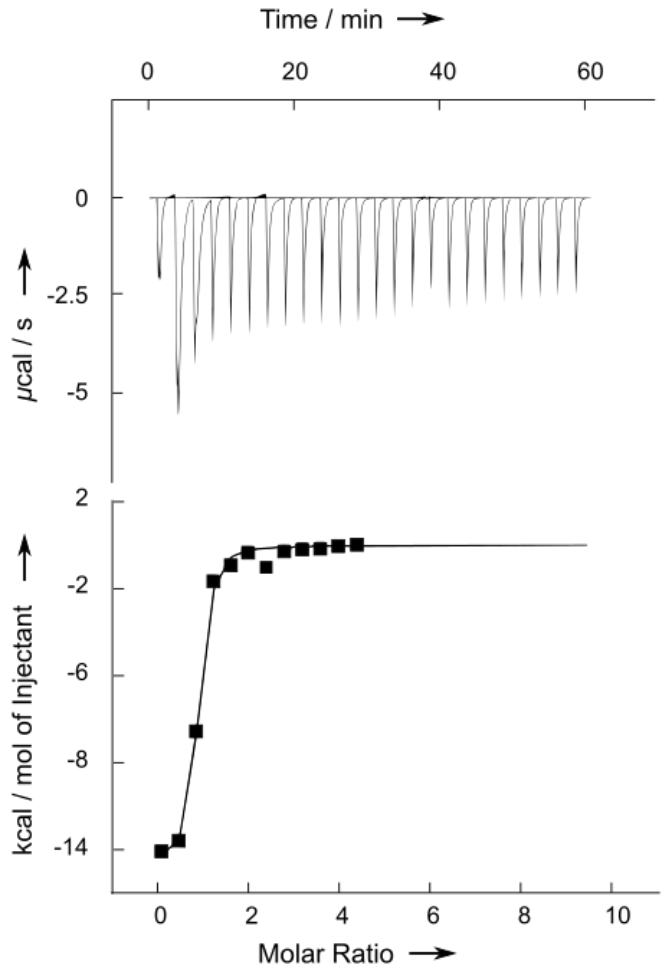

Figure 3.2. Isothermal titration calorimetry data for ΨMPG and Mn^{2+}. The top panel is the raw data, and the bottom shows the binding isotherm plotting the integrated heat peaks against the molar ratio of the enzyme. The heat change was fitted to a single site binding model using the Origin® software to obtain the binding affinity (K_i), enthalpy (ΔH), and entropy (ΔS). K_i = $(2.05 \pm 0.59)\cdot 10^5$ M^{-1}, $\Delta H = -(1.475 \pm 0.390)\cdot 10^4$ cal·mol^{-1}, and $\Delta S = -28.7$ cal·mol^{-1}·°C^{-1}. In the single binding site model, $Q = M_t \Delta H V_0 \left[1 + X_t/M_t + 1/(K_i M_t) - \sqrt{(1 + X_t/M_t + 1/(K_i M_t))^2 - 4X_t/M_t}\right]$. Q is the total heat content, V_0 is the active cell volume, and X_t and M_t are the bulk concentrations of Mn^{2+} and ΨMPG. Reprinted with permission from [142].

To titrate the line broadening with free Mn^{2+}, 1.27 M stock solution of uridine 5'-monophosphate (UMP) di-sodium salt hydrate (TCI America, Portland, OR) or 22 mM stock solution of 4,5-$^{13}C_2$-uracil were prepared in Tris buffer (50 mM Tris(hydro-

xymethyl)aminomethane hydrochloride, 50 mM sodium chloride, pH 7.5). Stock solutions of $MnCl_2$ were prepared in the same Tris buffer and added to the above UMP or uracil solution. The NMR samples for measurement contained 1.26 M UMP, $MnCl_2$ with a series of concentrations (0 μM, 6 μM, 10 μM, 22 μM, 40 μM, 90 μM, 220 μM, 300 μM, 600 μM) and 70 mM dioxane; or 20.2 mM uracil, $MnCl_2$ with a series of concentrations (0 μM, 6 μM, 10 μM, 22 μM, 40 μM, 90 μM, 220 μM) and 80 mM dioxane. Dioxane was added as a reference and D_2O was added for NMR frequency lock. The ^{13}C NMR spectra were acquired at the room temperature using a 400 MHz NMR spectrometer with a BBO probe. The pulse sequence consisted of a single ^{13}C excitation pulse with ^{1}H decoupling during the data acquisition.

Figure 3.3 shows the line width dependence on free Mn^{2+} for different atoms of uracil and UMP, a molecule similar to ΨMP. $\Delta\nu_{1/2}$ is the difference between the observed line width at half height of the resonance in the Mn^{2+} solution and that of the same resonance in the solution without Mn^{2+}. When $[Mn^{2+}] < 25$ μM, all $\Delta\nu_{1/2} < 1$ Hz.

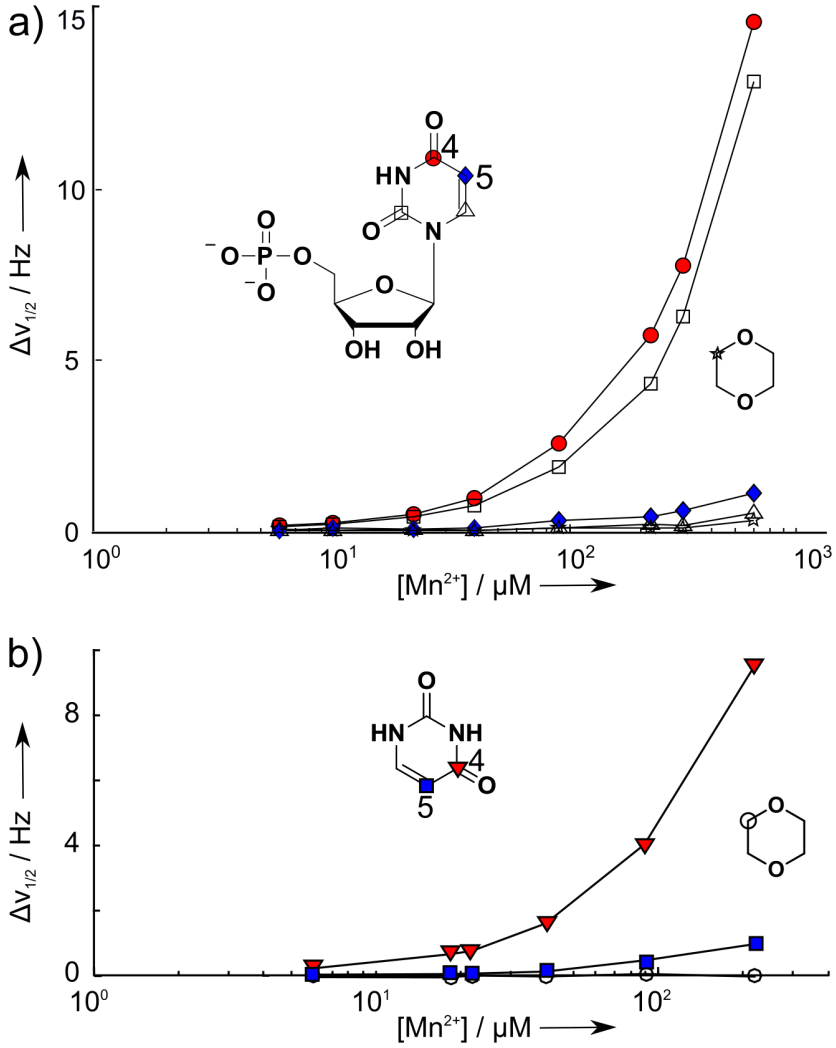

Figure 3.3. The dependence of $\Delta\nu_{1/2}$ on various Mn^{2+} concentration for base carbons of UMP (a) and C_4 and C_5 in uracil (b). Reprinted with permission from [142].

3.2.3. Kinetic Model and Fitting

a. Model for Curve Fitting

Scheme 3.1. Proposed reaction mechanisms for the synthesis of ΨMP under the catalysis of ΨMPG. (a) The bireactant enzyme reaction mechanism. (b) The simplified unireactant enzyme reaction mechanism when R5P is in excess. (c) The simplified unireactant mechanism with the fast exchange between the free and enzyme-bound product. U, E, and P stand for uracil, ΨMPG, and ΨMP respectively. E-R5P is the enzyme-R5P complex, and E-R5P-U is the intermediate complex which is the same as EU. EP is the enzyme-product complex. k_1 and k_{-3} are the second-order rate constants, and k_{-1}, k_2, k_{-2} and k_3 are the first-order rate constants.

$$U + R5P + E \rightleftharpoons U + E - R5P \rightleftharpoons E - R5P - U \rightleftharpoons P + E \quad \text{(a)}$$

$$U + E \underset{k_{-1}}{\overset{k_1}{\rightleftharpoons}} EU \underset{k_{-2}}{\overset{k_2}{\rightleftharpoons}} P + E \quad \text{(b)}$$

$$U + E \underset{k_{-1}}{\overset{k_1}{\rightleftharpoons}} EU \underset{k_{-2}}{\overset{k_2}{\rightleftharpoons}} EP \underset{k_{-3}}{\overset{k_3}{\rightleftharpoons}} P + E \quad \text{(c)}$$

A mechanism for ΨMPG catalysis coupling R5P and uracil was previously proposed as in Scheme 3.1(a).[151] R5P first forms a complex with the enzyme and further reacts with uracil to produce an intermediate which finally dissociates into the product and free enzyme. Since an excess amount of R5P was used, all the enzymes were saturated with R5P. In this case, the simplified unireactant enzyme reaction mechanism in Scheme 3.1(b) can be used, in which uracil reacts with free enzyme first to form the intermediate and then ΨMP is released from the free enzyme. In order to explain the line width broadening of the product signals, Scheme 3.1(c) was finally used as the fitting model including the fast exchange between the free and enzyme-bound product.

b. Fitting of the NMR signals

4,5-$^{13}C_2$-uracil was used in the DNP experiment, therefore only the NMR signals originating from C_4 and C_5 in the reactant uracil, $C_{4'}$ and $C_{5'}$ in the product ΨMP, and C_{4*} and C_{5*} in the intermediates EU and EP were considered. Raw FID data was Fourier transformed after applying an exponential window function with 0.5 Hz line broadening using the TOPSPIN program (Bruker Biospin). The integration, line width measurement, and fitting were performed by MATLAB (The MathWorks, Natick, MA). A linear baseline correction was applied for each peak, defined by points on either side of the peak.

Equations 3.1 – 3.4 were used for NMR signal evolution between two pulses. Signals were multiplied by cos(α) after a pulse was applied. The concentration changes of uracil ([U]), ΨMP ([P]), the intermediates ([EU] and [EP]), and free enzyme ([E]) follow Equations 3.5 – 3.9 respectively.

$$\frac{dS_U}{dt} = -k_1 \times S_U \times [E] + k_{-1} \times S_{EU} - R_{1,U} \times S_U \tag{3.1}$$

$$\frac{dS_{EU}}{dt} = k_1 \times S_U \times [E] + k_{-2} \times S_{EP} - (k_{-1} + k_2) \times S_{EU} - R_{1,EU} \times S_{EU} \tag{3.2}$$

$$\frac{dS_{EP}}{dt} = k_2 \times S_{EU} + k_{-3} \times S_P \times [E] - (k_{-2} + k_3) \times S_{EP} - R_{1,EP} \times S_{EP} \tag{3.3}$$

$$\frac{dS_P}{dt} = k_3 \times S_{EP} - k_{-3} \times S_P \times [E] - R_{1,P} \times S_P \tag{3.4}$$

$$\frac{d[U]}{dt} = -k_1 \times [U] \times [E] + k_{-1} \times [EU] \tag{3.5}$$

$$\frac{d[P]}{dt} = k_3 \times [EP] - k_{-3} \times [P] \times [E] \tag{3.6}$$

$$\frac{d[EU]}{dt} = k_1 \times [U] \times [E] + k_{-2} \times [EP] - (k_{-1} + k_2) \times [EU] \tag{3.7}$$

$$[EP] = [U]_0 - [U] - [EU] - [P] \tag{3.8}$$

$$[E] = [E]_0 - [EU] - [EP] \tag{3.9}$$

Since $v_{1/2} = R_{2,obs} / \pi$, line widths of $C_{4'}$ and $C_{5'}$ in the product contain R_2 relaxation rate values. Line widths were obtained from the Lorentzian fit to the peaks after the baseline correction. Under fast exchange, $R_{2,obs}$ in the ΨMPG-Mg^{2+} and ΨMPG-Mn^{2+} reactions can be expressed as $R_{2,obs}(\mathrm{Mg}) = X_b R^b_{2,Mg} + X_f R^f_2$, and $R_{2,obs}(\mathrm{Mn}) = X_b R^b_{2,Mn} + X_f (R^f_2 + R^f_{2,Mn})$ respectively, where X_b and X_f are the bound and free fractions, R^f_2 is the R_2 rate of the free product, $R^b_{2,Mg}$ or $R^b_{2,Mn}$ is the R_2 rate in the bound state, and $R^f_{2,Mn}$ is the R_2 rate caused by the free Mn^{2+} in the solution.

In the fitting, minimization was performed on fitted residuals of integrals and line widths which share the common parameters X_b and X_f. The R_1 relaxation rate of uracil was assumed the same in both ΨMPG-Mg^{2+} and ΨMPG-Mn^{2+} reactions, as well as in the control experiments without the enzyme, since from experiments the free Mn^{2+} of ~ 20 μM in the solution had little effect on R_1. Therefore, R_1 rates of C_4 and C_5 were first obtained from the control. Considering that the intermediate signals are not separate from the free ones, the observed reactant signal is assumed to be the sum of *U* and *EU*, and the product signal should be the sum of *EP* and *P*. To counteract differences arising from different shimming in each injected sample, the line widths of the product peaks were corrected by subtracting the line width of the acetone peak in the same spectrum, followed by addition of the average line width of the acetone peak from all spectra. Line widths from the spectra measured in the time interval between 4.34 and 11.54 s were used for model fitting. This time interval was chosen to avoid potential sample settling at the beginning of the experiment, and reduced signal-to-noise ratio at the end of the

experiment. $R^f_{2,Mn}$ of *P* was assumed to be the same as of UMP, which was determined from titration with Mn^{2+} as 0.51π and 0.06π s^{-1} for $C_{4'}$ and $C_{5'}$ respectively, at a Mn^{2+} concentration of 22 μM (Figure 3.3).

Three data sets with different enzyme concentrations (120 μM, 83 μM, and 56 μM) were used to fit the unknown kinetic and relaxation rate constants simultaneously. The MATLAB function Parallel MultiStart was used to realize global optimization. The method of least sum of squared errors was used to obtain the best fitting parameters (Table 3.1). 95% confidence intervals were obtained from the Jacobian matrix.

c. Kinetic and Relaxation Fitting Results

The fitting result is self-consistent with the assumption made above, that contributions from bound and free forms are combined in single observable signals. For EP and P, the calculated exchange rate satisfies the fast exchange assumption (see Section 3.3.2). Despite relatively small k_{-1}, the reactant peaks in both reactions are broader than in the control experiments without the enzyme, suggesting that the observed peaks of U and EU are also not separate. This is possible if U and EU have resonance frequencies differing by less than ~ 5 Hz. We also fitted rates under the assumption that only free forms are observed for the reactant peaks. In this case, ΔG derived from the fitting differs in Mg^{2+} and Mn^{2+} reactions (-19 and -32 kJ/mol respectively), which would not be expected, and also deviates from the literature value of -21 kJ/mol. Additionally, the calculated EU fractions are larger than 10%, but small peaks are not observed around the reactant peaks.

Table 3.1. Fitted kinetic rate constants, line widths, and R_1 / R_2 rates in ΨMPG-Mg^{2+} and ΨMPG-Mn^{2+} reactions with 95% confidence intervals. $R_{1,EU4/EP4}$ and $R_{1,EU5/EP5}$ are the R_1 rates of C_{4*} and C_{5*} in the intermediate states. $R_{1,C4} = 0.046 \pm 0.005\ s^{-1}$ and $R_{1,C5} = 0.244 \pm 0.008\ s^{-1}$ were obtained separately from exponential fit to spectra from the control experiments. The line widths of $C_{4'}$ and $C_{5'}$ are close to the reference acetone peak (2.08 Hz). The differences in R_1 / R_2 of intermediate states from Mg^{2+}/Mn^{2+} reactions can be explained by the paramagnetic effect and discussed in Section 3.2.4. Reprinted with permission from [142].

Fit parameters	in ΨMPG-Mg^{2+} reaction	in ΨMPG-Mn^{2+} reaction
k_1 ($M^{-1}s^{-1}$)	$(2.17 \pm 0.00)\cdot10^4$	$(2.22\pm 0.03)\cdot10^4$
k_{-1} (s^{-1})	0.63 ± 0.02	0.64 ± 0.04
k_2 (s^{-1})	2.28 ± 0.03	4.09 ± 0.09
k_{-2} (s^{-1})	0.16 ± 0.02	0.64 ± 0.02
k_3 (s^{-1})	$(2.92 \pm 0.03)\cdot10^4$	$(0.56 \pm 0.01)\cdot10^4$
k_{-3} ($M^{-1}s^{-1}$)	$(9.93 \pm 0.26)\cdot10^7$	$(1.00 \pm 0.07)\cdot10^7$
$R_{1,C4'}$ (s^{-1})	0.15 ± 0.01	
$R_{1,C5'}$ (s^{-1})	0.17 ± 0.00	
$R_{1,EU4/EP4}$ (s^{-1})	0.17 ± 0.03	1.60 ± 0.04
$R_{1,EU5/EP5}$ (s^{-1})	0.13 ± 0.01	1.49 ± 0.04
$\nu_{1/2,C4',free}$ (Hz)	2.11 ± 0.77	
$\nu_{1/2,C5',free}$ (Hz)	2.18 ± 0.77	
$R^b_{2,C4'}$ (s^{-1})	16 ± 24	206 ± 34
$R^b_{2,C5'}$ (s^{-1})	9 ± 24	104 ± 33

A Monte Carlo simulation with 4000 samples was performed to account for the concentration variation of the enzyme and substrate, which was estimated to have a standard deviation of approximately 5% based on dilution tests of the DNP sample injector. In each sample, the enzyme and substrate concentrations in the six experiments were randomly generated from a normal distribution with a standard deviation of 5% of the mean values. Curves were then fitted using initial values from the previous global

optimization. A nonlinear least-squares solver (lsqnonlin, MATLAB) was used. Table 3.2 summarizes the 95% fit parameter confidence ranges from this simulation.

Table 3.2. Fit parameter error ranges, accounting for the enzyme and substrate concentration variation. Reprinted with permission from [142].

Fit parameters	in ΨMPG-Mg^{2+} reaction	in ΨMPG-Mn^{2+} reaction
k_1 ($M^{-1}s^{-1}$)	$(2.17 \pm 0.24)\cdot 10^4$	$(2.23 \pm 0.12)\cdot 10^4$
k_{-1} (s^{-1})	0.47 ± 0.13	0.64 ± 0.12
k_2 (s^{-1})	2.46 ± 0.26	4.13 ± 0.29
k_{-2} (s^{-1})	0.13 ± 0.11	0.65 ± 0.12
k_3 (s^{-1})	$(2.29 \pm 0.35)\cdot 10^4$	$(0.45 \pm 0.08)\cdot 10^4$
k_{-3} ($M^{-1}s^{-1}$)	$(9.25 \pm 1.28)\cdot 10^7$	$(0.85 \pm 0.15)\cdot 10^7$
$R_{1,C4'}$ (s^{-1})	0.12 ± 0.02	
$R_{1,C5'}$ (s^{-1})	0.16 ± 0.02	
$R_{1,EU4/EP4}$ (s^{-1})	0.40 ± 0.12	1.97 ± 0.21
$R_{1,EU5/EP5}$ (s^{-1})	0.28 ± 0.10	1.63 ± 0.15
$\nu_{1/2,C4',free}$ (Hz)	2.12 ± 0.32	
$\nu_{1/2,C5',free}$ (Hz)	2.19 ± 0.18	
$R^b_{2,C4'}$ (s^{-1})	15 ± 8	206 ± 22
$R^b_{2,C5'}$ (s^{-1})	8.5 ± 4.5	104 ± 11

3.2.4. Distance Determination Based on PRE

The increase in R_1 and R_2 rates of carbon nuclei in the bound product with Mn^{2+} is mainly attributed to PRE, which can be used for determining active site distances based on the following calculations. For an isotropic electron system such as Mn^{2+}, PRE is mainly caused by direct dipole-dipole interactions.[75] The electronic relaxation of Mn^{2+} is

on a faster time scale than the chemical exchange and complex rotation. At ~10 T or a higher magnetic field, transverse electronic relaxation can be ignored without introducing significant errors.[145,154] Here, the experiments were performed in a 9.4 T field. Therefore, PRE contributions to R_1 and R_2 in the bound complex can be described by Equations 3.10 and 3.11, using one effective correlation time.[77] For Mn^{2+}, τ_c is between 4 and 10 ns, and the intrinsic angular momentum quantum number $S = 5 / 2$.[77,155] Using the equations, distances between the paramagnetic Mn^{2+} center and the $C_{4'}$ and $C_{5'}$ atoms in enzyme complexed ΨMP were calculated. The 95% error ranges of the distances d were calculated from the standard error, $SE(d)$. $SE(d)$ was determined via the propagation of uncertainty. Since τ_c ranges from 4 to 10 ns, mean(τ_c) = 7 ns and $SE(\tau_c)$ = 3 ns were used. From the Monte Carlo simulation, the distribution of R^b_1 and R^b_2 were found to be close to the normal distribution. Distance values were calculated from the median values of R^b_1 and R^b_2. SE of R^b_1 and R^b_2 were obtained from the 2.5% and 97.5 % percentile of the distributions. Additionally, distances were calculated from the best fit result alone for R^b_1 and R^b_2. In this case, SE of R^b_1 and R^b_2 were obtained from the Jacobian Matrix.

$$R_1^{PRE} = \frac{2}{15}\left(\frac{\mu_0}{4\pi}\right)^2 \frac{\gamma^2 g_e^2 \mu_B^2 S(S+1)}{d^6} \cdot \frac{3\tau_c}{1+\omega_I^2\tau_c^2} \tag{3.10}$$

$$R_2^{PRE} = \frac{1}{15}\left(\frac{\mu_0}{4\pi}\right)^2 \frac{\gamma^2 g_e^2 \mu_B^2 S(S+1)}{d^6} \cdot \left(4\tau_c + \frac{3\tau_c}{1+\omega_I^2\tau_c^2}\right) \tag{3.11}$$

Here, μ_0 is the magnetic constant, γ is the gyromagnetic ratio of the nucleus, g_e is the free electron g value, μ_B is the Bohr magneton, d is the distance between the nucleus and the paramagnetic center, and ω_I is the Larmor frequency of the nucleus. The correlation time

τ_c is defined as $(\tau_r^{-1} + \tau_s^{-1})^{-1}$, where τ_r is the rotational correlation time and τ_s is the effective electron spin relaxation time.

3.3. Results and Discussion

3.3.1. Dissolution DNP Monitored Metalloenzyme Catalysis

In the present experiments, we aimed to measure the PRE by comparing the signal evolution under catalysis by ΨMPG with diamagnetic Mg^{2+} and paramagnetic Mn^{2+} in the active site. ^{13}C hyperpolarized substrates 4,5-$^{13}C_2$-uracil and ribose-5-phosphate (R5P) were rapidly mixed with a solution of the purified ΨMPG-Mg^{2+} or ΨMPG-Mn^{2+} complex. The catalyzed reaction resulted in the formation of ΨMP, in the thermodynamically favored reaction direction, which is the reverse of the *in vivo* pathway (Figure 3.4a). Real-time ^{13}C NMR spectra were recorded using successive small-flip angle excitations. An individual spectrum taken from each time series at 2.34 s is plotted in Figure 3.4b, and the entire time series of spectra are shown in Figure 3.1.

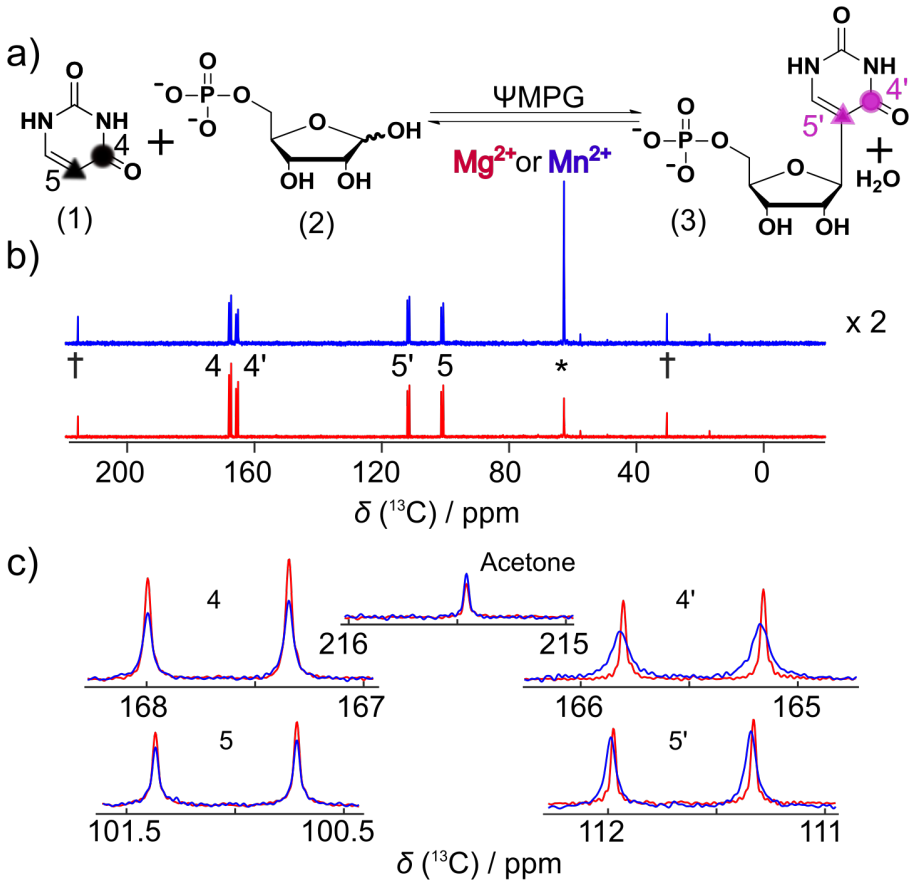

Figure 3.4. a) Reaction of ΨMPG, *in vitro* occurring left to right, coupling uracil (1) and R5P (2) to form ΨMP (3). b) Individual spectra from the time point at 2.34 s, of reactions with Mg^{2+}(red) and Mn^{2+}(blue, scaled ×2). A total of 96 scans were acquired over a total acquisition time of 39 s. The peaks labeled with '†' are from the internal reference acetone. '*' indicates the peak of the glassing solvent ethylene glycol used for DNP polarization, initially suppressed by a selective pulse followed by a pulsed field gradient. c) Enlarged reactant and product peaks. In all spectra, chemical shifts are calibrated using the acetone peak at 215 ppm. The concentrations of uracil (^{13}C labeled for observation), R5P (added in excess), and enzyme were 560 µM, 10 mM, and 83 µM respectively. Reprinted with permission from [142].

Owing to the large chemical shift range of ^{13}C, reactant and product peaks are readily separated. An increase in polarization of ~ 5000 times was calculated by comparing the measured spectra to a thermal equilibrium spectrum of a reference compound. This enhancement also allowed observation of signals from R5P at natural ^{13}C

isotope abundance in the first scans (Figure 3.1), which were however not further analyzed.

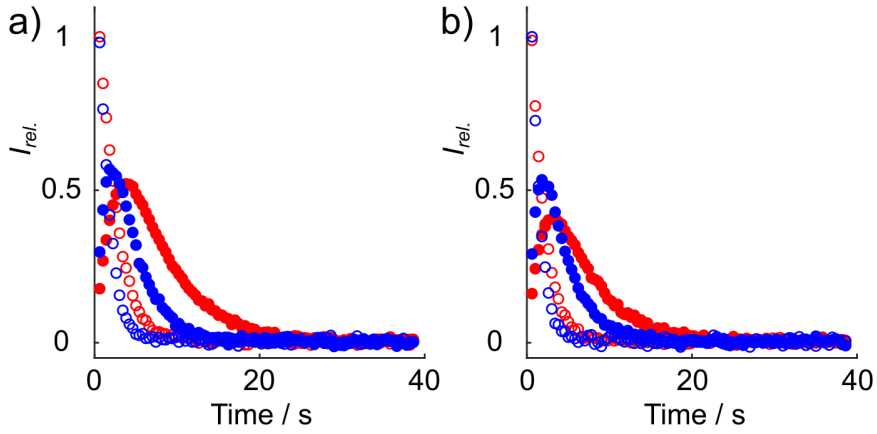

Figure 3.5. Time-dependent integrals in ΨMPG catalyzed reactions with Mg^{2+}(red) and Mn^{2+}(blue). a) Labeled positions in the reactant uracil (4) and in the product ΨMP (4'); b) Labeled positions 5 and 5'. Open and filled circles represent reactant and product peaks respectively. The integrals, $I_{rel.}$, were normalized to the maximum signal. Reprinted with permission from [142].

Spectra show signals of reactant and product at nearly identical chemical shifts in Mg^{2+} and Mn^{2+} reactions (Figure 3.4c). It is apparent, however, that the product peaks have larger line widths in the reaction with Mn^{2+} than with Mg^{2+}. This line broadening cannot be explained by dissociated free Mn^{2+} alone (Section 3.2.2), and may instead be explained by PRE occurring in enzyme complexed product in fast exchange with its free form. The time evolution of integrated signals of the labeled reactant and product peaks is shown in Figure 3.5. Signal intensities change due to the combined effects of spin relaxation, reaction kinetics, and radio frequency pulses.[99] The reactant peaks decay more rapidly, and the product peaks reach their maxima earlier and also decay faster in the reaction with Mn^{2+}. This difference *prima facie* would be caused by increased reaction

and relaxation rates in the presence of paramagnetic Mn^{2+}. Differences in reaction rates with other ions in the active site of ΨMPG have in fact previously been observed, and have been attributed to a dependence on the ionic radius.[151]

3.3.2. Kinetics Determination

A kinetic model is proposed in Scheme 3.1(c) to explain the observed signal evolution quantitatively, and to determine kinetic rate constants and spin relaxation rates that can be used for distance calculation. Signal intensities and product line widths from datasets with three different enzyme concentrations were fitted simultaneously using this model (see Section 3.2.3 for full explanations). This procedure is similar to reference 156, albeit using different input data.

The analysis results in relaxation rates and kinetic rate constants of detailed steps in both forward and reverse directions in the ΨMPG catalyzed reaction. The fitted time evolution of integrals and line widths is plotted in Figure 3.6. The best fit parameters are summarized in Tables 3.1 and 3.2. Fitting errors were estimated from the Jacobian matrix from the fitting procedure, as well as from a Monte Carlo simulation considering an additional ~ 5% uncertainty in the concentrations of the enzyme and substrate arising out of the injection procedure. The parameters $k_1 = (2.23 \pm 0.12) \cdot 10^4\ M^{-1} \cdot s^{-1}$ and $k_2 = (4.13 \pm 0.29)\ s^{-1}$ for the reaction catalyzed by ΨMPG-Mn^{2+} (95% confidence intervals from Monte Carlo simulation) are in remarkably good agreement with the kinetic rate constants determined previously using quench-flow experiments at the room temperature, $k_1 = (2.2 \pm 0.36) \cdot 10^4\ M^{-1} \cdot s^{-1}$ and $k_2 = (3.74 \pm 0.14)\ s^{-1}$.[151] In the ΨMPG-$Mg^{2+}$ reaction, $k_1 = (2.17 \pm 0.24) \cdot 10^4\ M^{-1} \cdot s^{-1}$ and $k_2 = (2.46 \pm 0.26)\ s^{-1}$, are obtained. The dissociation rate constant of the enzyme-product complex k_3 is $(2.29 \pm 0.35) \cdot 10^4\ s^{-1}$ in the ΨMPG-Mg^{2+} reaction

and $(0.45 \pm 0.08) \cdot 10^4$ s^{-1} in the ΨMPG-Mn^{2+} reaction, consistent with the fast exchange assumption that $k_{ex} = k_3 + k_{-3}$ [E] > Δv (the frequency difference between free and bound forms, Δv, is estimated as ~ 40 Hz from the product peak shifts in the Mg^{2+} and Mn^{2+} reactions and the calculated proportions of the bound product). The association rate k_{-3} is $(9.25 \pm 1.28) \cdot 10^7$ and $(0.85 \pm 0.15) \cdot 10^7$ $M^{-1} \cdot s^{-1}$ in the Mg^{2+} and Mn^{2+} reactions respectively, which is within the diffusion-limited range of ~10^7 – 10^9 $M^{-1}s^{-1}$.[132] A Gibbs free energy change of ΔG = -23 kJ/mol for the formation of the product is further calculated from fitted equilibrium concentrations, in both the reactions with Mg^{2+} and Mn^{2+}. This value compares to the literature value of -21 kJ/mol in the absence of enzyme,[152] indicating that the kinetic fitting correctly reproduces the overall equilibrium of the reaction. The small reverse reaction rate constants and the negative ΔG of the product formation are concordant with the fact that the formation of the C-C glycosidic bond is favored.

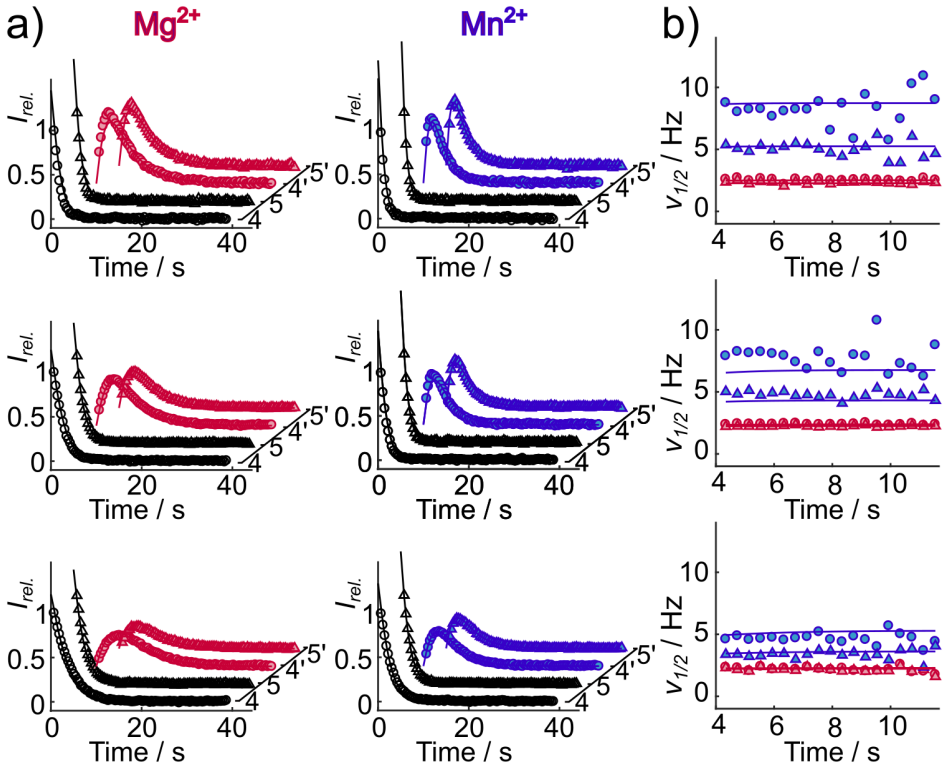

Figure 3.6. Time-dependent NMR signals in reactions with ΨMPG-Mg^{2+} or ΨMPG-Mn^{2+}, including the fitted curves. From top to bottom, the enzyme concentrations are 120, 83, and 56 µM respectively. a) Integrals of reactant and product peaks, $I_{rel.}$, normalized to the maximum signal. The curves are shifted to avoid overlapping. b) Line widths of the product peaks. In (a) and (b), open and filled circles represent positions 4 and 4' respectively; open and filled triangles represent 5 and 5' respectively. Reprinted with permission from [142].

3.3.3. Distance Constraints in the Active Site

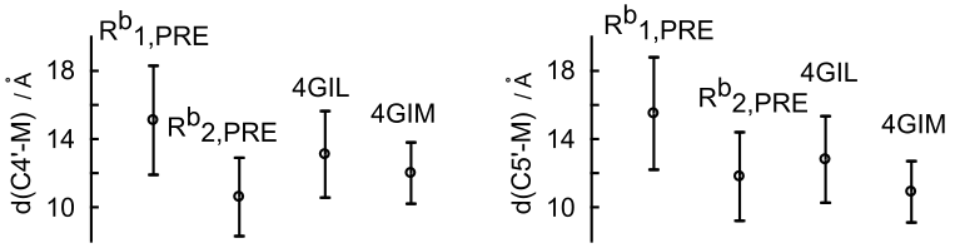

Figure 3.7. Distances between $C_{4'}/C_{5'}$ and the metal ion in the enzyme-product complex. From $R^b_{1,PRE}$, d($C_{4'}$-M) = 15.1 ± 3.2 Å and d($C_{5'}$-M) = 15.5 ± 3.3 Å; from $R^b_{2,PRE}$, d($C_{4'}$-M) = 10.6 ± 2.3 Å and d($C_{5'}$-M) = 11.8 ± 2.6 Å. For distances from two crystal structures, the error bars specify the resolutions. In 4GIL, d($C_{4'}$-M) = 13.1 ± 2.5 Å and d($C_{5'}$-M) = 12.8 ± 2.5 Å; in 4GIM, d($C_{4'}$-M) = 12.0 ± 1.8 Å and d($C_{5'}$-M) = 10.9 ± 1.8 Å. For distances based on $R^b_{1,PRE}$ and $R^b_{2,PRE}$, the values were calculated using the median values of R^b_1 and R^b_2 from the Monte Carlo simulation. The error bars indicate the 95% confidence intervals derived from the distribution of R^b_1 and R^b_2 in the simulation. From the best fit, the obtained distance ranges are: d($C_{4'}$-M) = 15.3 ± 3.2 Å and d($C_{5'}$-M) = 15.5 ± 3.3 Å via $R^b_{1,PRE}$; d($C_{4'}$-M) = 10.6 ± 2.4 Å and d($C_{5'}$-M) = 11.9 ± 2.8 Å via $R^b_{2,PRE}$. Reprinted with permission from [142].

Application of the paramagnetic relaxation theory to the extracted relaxation rates leads to the determination of distances between individual atoms of the enzyme-bound product and the active site metal. The differences of R_1 and R_2 rates from the enzyme-bound product in the reactions with Mn^{2+} *vs.* Mg^{2+} are expected primarily due to the paramagnetic effect, *i.e.* $R^b_{1,PRE} = R^b_{1,Mn} - R^b_{1,Mg}$ and $R^b_{2,PRE} = R^b_{2,Mn} - R^b_{2,Mg}$ (the superscript *b* denotes the enzyme bound form). Based on Equations 3.10 and 3.11 from the dipolar interaction mechanism of PRE,[77,154,155] distances between the metal center and $C_{4'}$ and $C_{5'}$ atoms in the active site are derived (Section 3.2.4). Figure 3.7 shows that the results are within error limits of distances measured in two crystal structures of related complexes (PDB ID: 4GIL and 4GIM),[151] although it should be noted that the crystal structures do not represent exactly the same complex: The product ring is open in 4GIL

and the enzyme is mutated in 4GIM (Figure 3.8). The distances calculated are subject to several sources of error. Firstly, R^b_1 is assumed to be the same in EU and EP in the model, since the enzyme bound forms are not directly observable. Thus $R^b_{1,PRE}$ derived distances for EP are average values between EU and EP along the reaction coordinate. Secondly, as in any measurement of the PRE, additional metal binding on the complex would cause further relaxation, which however would only be possible for weak affinity or a longer distance from the product atoms based on the magnitude of observed relaxation rates. The distances in principle are also averaged over an ensemble of dynamic states.

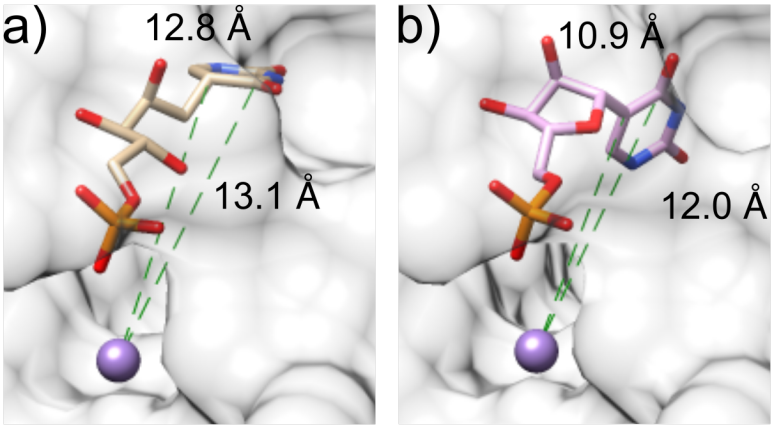

Figure 3.8. Crystal structures of ΨMPG – ΨMP complex. a) Wild type ΨMPG with covalent ΨMP adduct (PDB ID 4GIL). The ribose ring is open in a linear form and connected to lysine 166. Since ΨMPG exhibits a high stereospecificity to synthesize only the β-anomer,[152] the complex with linear sugar is unlikely to arise during the fast exchange, rather representing an intermediate structure in the steps of the catalysis.[151] b) ΨMP is observed with a closed ribose ring but the lysine forming the covalent adduct is mutated (K166A) (PDB ID 4GIM). (a) and (b) are plotted with the same orientation. Distances between $C_{4'}$ / $C_{5'}$ and Mn^{2+} are indicated. Reprinted with permission from [142].

3.3.4. Discussion

The combination of PRE and DNP advances the available methodology for the characterization of molecular structure and dynamics in two respects. Owing to the 10^3 – 10^4 fold signal enhancement by DNP, paramagnetic NMR measurements can be achieved at low concentration. The real-time ability of DNP also provides PRE experiments with time resolution, which may be exploited in the study of dynamic processes. As reported here, the measurements of PRE in ΨMPG for the first time characterize the actual complex arising in the process of the reaction, and not under equilibrium. Meanwhile, paramagnetic relaxation based methods add a capability for structural characterization to D-DNP experiments. This capability offers additional information beyond the measurement of kinetics from real-time DNP-NMR. The combined method is applicable to reactions involving compounds with naturally present or artificially introduced paramagnetic sites, including many enzyme catalyzed reactions, polymerizations such as with radical intermediates, and others.

3.4. Conclusion

In summary, the high sensitivity from hyperpolarization by D-DNP enables real-time paramagnetic NMR measurements. Hyperpolarized ^{13}C spectra were measured in a metalloenzyme catalyzed reaction with diamagnetic and paramagnetic metal substitution. Through a quantitative analysis of time-dependent NMR intensities and line widths, kinetic and nuclear spin relaxation rate constants were determined. Examining the paramagnetically enhanced R_1 and R_2 relaxation values of carbon nuclei in the enzyme complexed product, long-range distance information in the active site was obtained. This

approach therefore provides conformational information during an ongoing reaction, without the use of stabilized intermediates.

4. METABOLIC MEASUREMENTS OF NON-PERMEATING COMPOUNDS IN LIVE CELLS USING HYPERPOLARIZED NMR[3]

Hyperpolarization by dissolution dynamic nuclear polarization (D-DNP) has emerged as a technique for enhancing NMR signals by several orders of magnitude, thereby facilitating the characterization of metabolic pathways both *in vivo* and *in vitro*. Following the introduction of an externally hyperpolarized compound, real-time NMR enables the measurement of metabolic flux in the corresponding pathway. Spin relaxation however limits the maximum experimental time and prevents the use of this method with compounds exhibiting slow membrane transport rates. Here, we demonstrate that electroporation can serve as a method for membrane permeabilization for use with D-DNP in cell cultures. An electroporation apparatus hyphenated with stopped flow sample injection permits the introduction of the hyperpolarized metabolite within 3 s after the electrical pulse. In yeast cells that do not readily take up pyruvate, the addition of the electroporation pulse to the D-DNP experiment increases the signals of the downstream metabolic products CO_2 and HCO_3^-, which otherwise are near the detection limit, by 8.2 and 8.6-fold. Modeling of the time dependence of these signals then permits the determination of the respective kinetic rate constants. The observed conversion rate from pyruvate to CO_2 normalized for cell density was found to increase by a factor of 12 due to the alleviation of the membrane transport limitation. Using electroporation therefore

[3] Adapted with permission from "Liu, M.; Hilty, C. Metabolic Measurements of Nonpermeating Compounds in Live Cells Using Hyperpolarized NMR. *Anal. Chem.* **2018**, *90* (2), 1217–1222.".[157] Copyright (2019) American Chemical Society.

extends the applicability of D-DNP to *in vitro* studies to a wider range of metabolites, and at the same time reduces the influence of membrane transport on the observed conversion rates.

4.1. Introduction

Nuclear magnetic resonance (NMR), a spectroscopic technique capable of recognizing chemical identities even in complex mixtures, has long been applied to the determination of metabolic products and kinetics.[45,158,159] More recently, hyperpolarization of nuclear spins has been introduced as a method of enhancing signals and extending the reach of NMR to the characterization of metabolic pathways at an overall metabolite concentration that is reduced by several orders of magnitude compared to conventional non-hyperpolarized experiments.[87,102,160] Dissolution dynamic nuclear polarization (D-DNP) is a hyperpolarization technique that utilizes the larger electron Zeeman splitting, "transferring" the higher electron spin polarization to nuclear spins. This polarization process occurs at a low temperature in a magnetic field, after which hyperpolarized aliquots are dissolved and can be transferred to the NMR detector at room temperature.[14,88,143] In combination with magnetic resonance imaging (MRI), metabolic turnover of substrates such as pyruvate can readily be monitored *in vivo*.[161,162] D-DNP has also emerged as a tool capable of characterizing metabolic flux *in vitro*, either in perfused organs or in cell cultures.[163,164] These *in vitro* experiments have been used for basic metabolic characterization of cell lines, as well as for the development of methods for later use in *in vivo* MRI.[164]

The D-DNP experiment differs from conventional non-hyperpolarized NMR in that the observed signals stem from the polarization generated prior to the start of data

acquisition. The initially high signals, therefore, need to be acquired within the time frame of nuclear spin relaxation, which typically is on the order of seconds to tens of seconds.[87] Signal averaging is not possible, but data can be measured at multiple time points when using small-flip angle excitation. These conditions result in a short overall time scale of the experiment. For determining kinetics in systems containing multiple pathways, the ability to use a short time window may be beneficial in reducing the complexity of the problem. At the same time, the observation is limited to rapid processes.[165]

Since hyperpolarization by D-DNP occurs externally, the first potentially rate-limiting step in an experiment aiming at the elucidation of metabolism is the uptake of the metabolite into cells. Membrane transport is highly dependent on active transporters that differ among cell types.[166] A method for introducing small molecules into cells is electroporation. Hyperpolarized $^{133}Cs^{+}$ has been used to probe cellular membrane impairment of pre-loaded electroporated yeast cells.[167] Here, we introduce a method, where electroporation is hyphenated with stopped-flow sample injection and NMR detection. Electroporation allows for the introduction of arbitrary metabolites in cell cultures, compatible with D-DNP hyperpolarization. We demonstrate the measurement of the kinetics of pyruvate metabolism in yeast, a metabolite that is not readily transported into these cells. Finally, we discuss the application of this method for the determination of metabolic flux under *in vitro* conditions.

4.2. Experimental Section

4.2.1. Cell Preparation

Wild yeast strain W303 cells were grown in 50 mL culturing medium in a 125 mL Erlenmeyer flask. The culturing medium was prepared by dissolving 10 g yeast extract,

20 g peptone, and 20 g glucose in 1 L water. Cells were cultured in an incubating shaker at 300 rpm and 30 ºC, until the optical density at 600 nm (OD^{600}) ≈ 1.8 was reached. The cells were then collected by centrifugation at 447 g for 1 min, and dispersed in 45 mL culturing medium without glucose. This rinsing procedure was repeated twice to remove glucose. After each step, cells were collected by centrifugation. The final cell concentration was adjusted by adding culturing medium without glucose to reach a linearly extrapolated value for OD^{600} of ≈ 400 (the OD was measured at 500-fold dilution).

4.2.2. Hyperpolarization

The hyperpolarized samples consisted of 0.89 M [1-^{13}C]-pyruvate (Cambridge Isotope Laboratories, Andover, MA), 15 mM tris[8-carboxy-2,2,6,6-tetrakis(2-hydroxyethyl)benzo[1,2-d:4,5-d']bis[1,3]-dithiol-4-yl]methyl free radical sodium salt (OX063; Oxford Instruments, Abingdon, U.K.), and 0.5 mM gadolinium diethylenetriaminepentaacetic acid in a solvent consisting of 3:2 v/v ethylene glycol / D_2O. Sample aliquots of 5 μL volume were hyperpolarized on ^{13}C by irradiation of microwaves with 60 mW power and 93.974 GHz frequency, at a temperature of 1.4 K in a HyperSense DNP polarizer (Oxford Instruments). The polarization time was 3 hours.

4.2.3. Sample Injection and Electroporation

400 μL of the concentrated yeast cell culture in medium without glucose was pre-loaded into an electroporation cuvette with 2 mm gap (Phenix Research Products, Candler, North Carolina). The cuvette was located in an electrically insulated housing ex-situ to the NMR instrument (Figure 4.1). The cuvette was connected with electrical leads to the electroporator (Model 2510, Eppendorf, Germany). Tubing (0.8 mm inner diameter) was installed in the bottom of the cuvette to connect it to the sample injection system. For

dissolution of the hyperpolarized sample, 4 mL pure water was heated until the vapor pressure reached 10^6 Pa. Under these conditions, the solvent reached a final temperature of approximately 160 ºC before entering the cryogenic region of the DNP polarizer. Immediately before dissolution occurred, an electroporation pulse of 1600 V was applied to the cell suspension. The hyperpolarized pyruvate sample was then dissolved, and the solution was automatically collected into a sample loop (Loop1 in Figure 4.1). The electroporated cells were drawn through the pre-installed tubing into a second sample loop (Loop2), using vacuum produced by a syringe. Subsequently, two injection valves connected to the respective loops were switched, and the cell suspension and pyruvate solution were simultaneously driven into the flow cell inside the magnet. The driving force was provided by water from two high pressure pumps. This sample injection followed previously described procedures.[91] During injection, cells and hyperpolarized pyruvate solution mixed within a Y-connector mixer. This mixing occurred 2 to 3 s after the electroporation pulse. After a total injection time of 760 ms, the sample mixture arrived in the NMR flow cell. The injection valves were switched to their original positions to stop flow, and the pumps were stopped. Control experiments were performed using the same procedures, but without applying the electroporation pulse. In all experiments, the final concentration of pyruvate was 10 mM, and the cell density was diluted by 50 % compared to the density loaded into the cuvette. These final concentrations and dilutions were determined before the D-DNP experiment, using dimethyl sulfoxide as a reference compound.

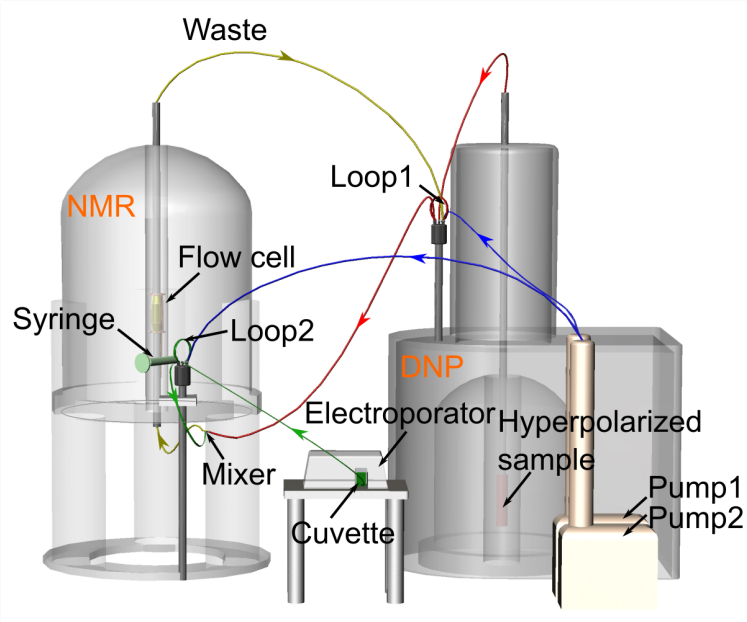

Figure 4.1. Diagram of ex-situ electroporator interfaced with DNP-NMR. Red and green lines indicate the injection pathways of the hyperpolarized pyruvate and cell solutions, respectively. The flow path of the mixture is indicated with yellow lines. Blue lines indicate water used to drive the samples from the two pumps. Reprinted with permission from [157].

Viability after electroporation was determined in separate experiments by counting colony-forming units. Cells with and without electroporation were collected and diluted to $OD^{600} \approx 3.5 \cdot 10^{-5}$. A volume of 100 µL was inoculated to agar plates. Colony-forming units were counted after incubation at 30 ºC for 48 hours.

4.2.4. NMR Spectroscopy

The flow cell was positioned inside a triple resonance TXI probe installed in a 400 MHz NMR spectrometer (Bruker Biospin, Billerica, MA). After injection and following a stabilization time of 500 ms, a series of small flip angle pulses was applied to observe ^{13}C NMR spectra of the metabolic reactions in real time. The pulse sequence consisted of [G_z– P_α – acquire], and was repeated 32 times at an interval of 5 s between subsequent

pulses. The pulse P_α was adjusted for a flip angle $\alpha = 30^o$ and had a pulse strength of $(\gamma B_1)/2\pi = 17.86$ kHz, where B_1 is the amplitude of the excitation radio frequency field. For each scan, 11028 complex points were collected. A pulsed field gradient G_z (45.5 G/cm, 1 ms) was applied to remove remaining coherence before each new scan.

4.2.5. Data Analysis

Raw FID data were Fourier transformed after applying an exponential window function with 2 Hz line broadening and phase corrected using the TOPSPIN program (Bruker Biospin). Peak integration and fitting of signal intensities were performed with MATLAB (The MathWorks, Natick, MA). Before integration, a linear baseline correction was applied for each peak, defined by baseline points on either side of the peak.

4.3. Results and Discussion

4.3.1. Metabolism Profile

After the mixture of hyperpolarized [1-^{13}C]-pyruvate and electroporated yeast cells arrives in the NMR probe, the buildup of the metabolic products is readily observable (Figure 4.2a). The individual signals are best identified by considering an individual spectrum of this time series. The spectrum measured 15.5 s after injection is displayed in Figure 4.2b. The pyruvate C1 signal can be seen at 170.4 ppm, as well as the predominant products CO_2 (124.8 ppm) and HCO_3^- (160.4 ppm) at intensities that are 96 and 225 times lower than the pyruvate signal. These relative signal intensities depend on the overall metabolic activity of the cells, and also on the cell density. Signals from unlabeled C2 and C3 of pyruvate, are also visible. Integrals of these signals are approximately 100-fold lower, and additionally the signals are split due to the ^{1}H-^{13}C coupling. Nevertheless, the

initially high enhancement in signal to noise ratio and concomitantly the dynamic range of the hyperpolarized experiment suffice for observing these signals.

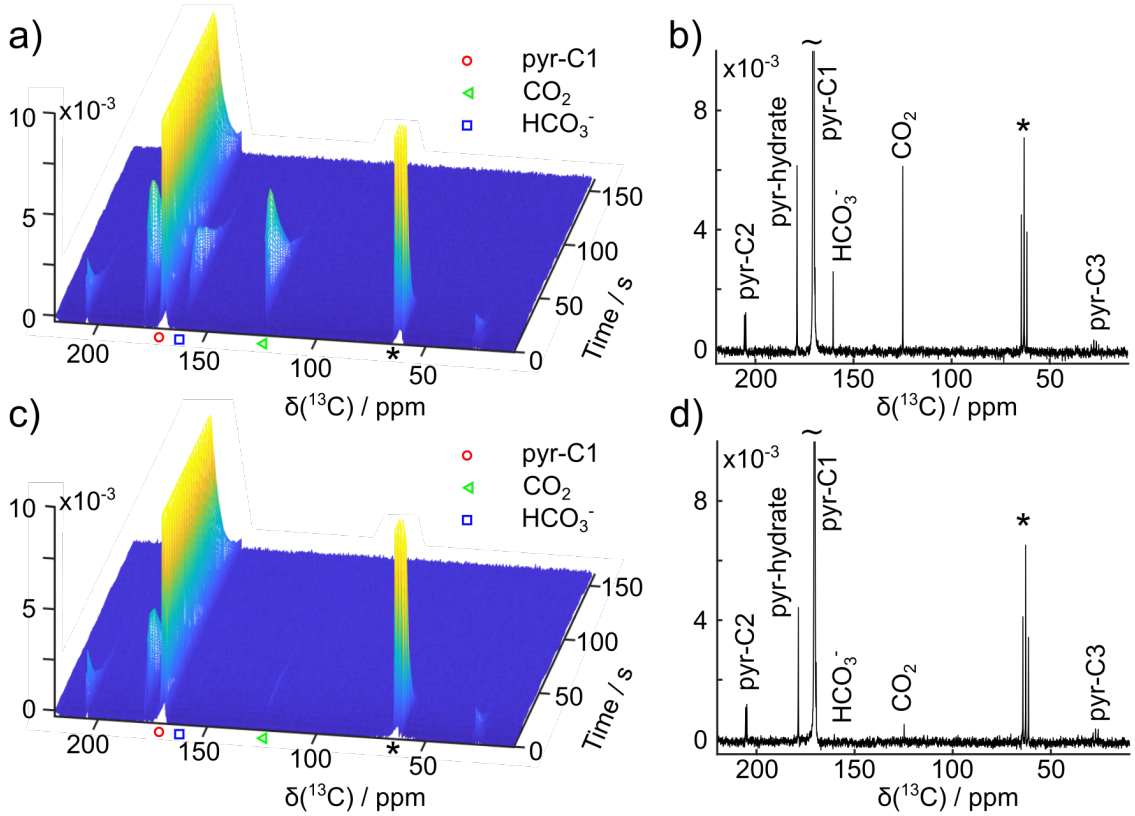

Figure 4.2. a) Time series of ^{13}C NMR spectra obtained after introducing hyperpolarized [1-^{13}C]-pyruvate into electroporated yeast cells. b) 1D spectrum from the series in (a), taken at 15.5 s after injection into the flow cell. c) Time series as in (a), with omission of the electroporation pulse. d) Spectrum from (c), taken 15.5 s after injection. In all spectra, resonance peaks from C1, C2, and C3 of pyruvate are labeled as pyr-C1, pyr-C2, and pyr-C3. Pyruvate hydrate is referred to as pyr-hydrate. * indicates the solvent peak from the hyperpolarized ethylene glycol. The intensity values are shown relative to the intensity of hyperpolarized pyruvate in the first scan. Signals of pyr-C1 and * that are larger than the axis scale are cut at the top of the scale in all panels. Reprinted with permission from [157].

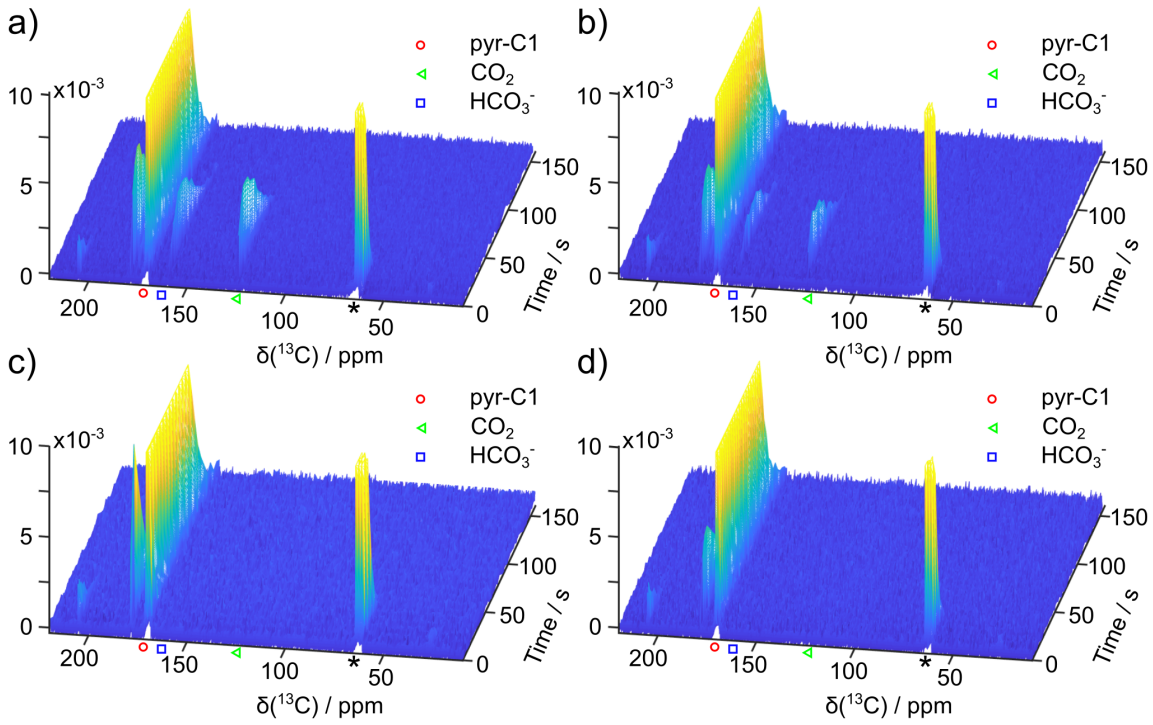

Figure 4.3. Time series of NMR spectra obtained in pyruvate metabolism in yeast cells. The data were acquired in the same way as those shown in Figure 4.2. (a) and (b) represent data from electroporated yeast cells mixed with hyperpolarized [1-^{13}C]-pyruvate. (c) and (d) represent data from non-electroporated yeast cells mixed with hyperpolarized [1-^{13}C]-pyruvate. Reprinted with permission from [157].

In contrast, signal intensities of CO_2 and HCO_3^- are lower by factors of 8.2 and 8.6, respectively, without electroporation (Figures 4.2c and d). This difference is despite hyperpolarization levels of pyruvate differing by less than 4 % in the two experiments with and without electroporation that are shown. The repeatability of the experiment is further validated by two additional sets of data, each comprising an experiment with and without electroporation (see Figure 4.3). The difference between the data in Figure 4.2a and c therefore can be attributed to the electroporation pulse. Such a difference is anticipated, since the cells were cultured with glucose before the NMR experiment. Under

these growth conditions, the lactate / pyruvate permease that would be capable of transporting these compounds is not expressed or is degraded, leaving pyruvate to pass the plasma membrane only through simple diffusion.[168] These yeast cells do not readily take up pyruvate through the cell membrane, but nevertheless contain pyruvate decarboxylase in the cytosol.[169] Therefore, in the experiments described here, CO_2 can only be produced in substantial quantity if the diffusion barrier of the membrane is removed by the electroporation pulse. Under the catalytic action of the enzyme carbonic anhydrase, HCO_3^- is further produced from CO_2. On the other hand, pyruvate hydrate, which is formed non-metabolically in aqueous solution, appears in both experiments.

The near absence of membrane transport for pyruvate into the yeast cells used here stands in contrast to other metabolites, such as glucose and fructose. Unlike pyruvate, these metabolites can be taken up into yeast cells actively.[170] Meier *et al.* readily observed metabolic products after mixing with hyperpolarized glucose and fructose, and were able to visualize the respective pathways.[171] Experiments with hyperpolarized glucose performed using the protocols described here are shown in Figure 4.4. In these experiments, the amount of yeast cells is about 10 times smaller than in reference 171, and otherwise experiments are comparable. The difference in the maximum product signal intensity when using hyperpolarized glucose with or without electroporation is only approximately 30 %. This result is expected, when the membrane transport is not the rate limiting step.

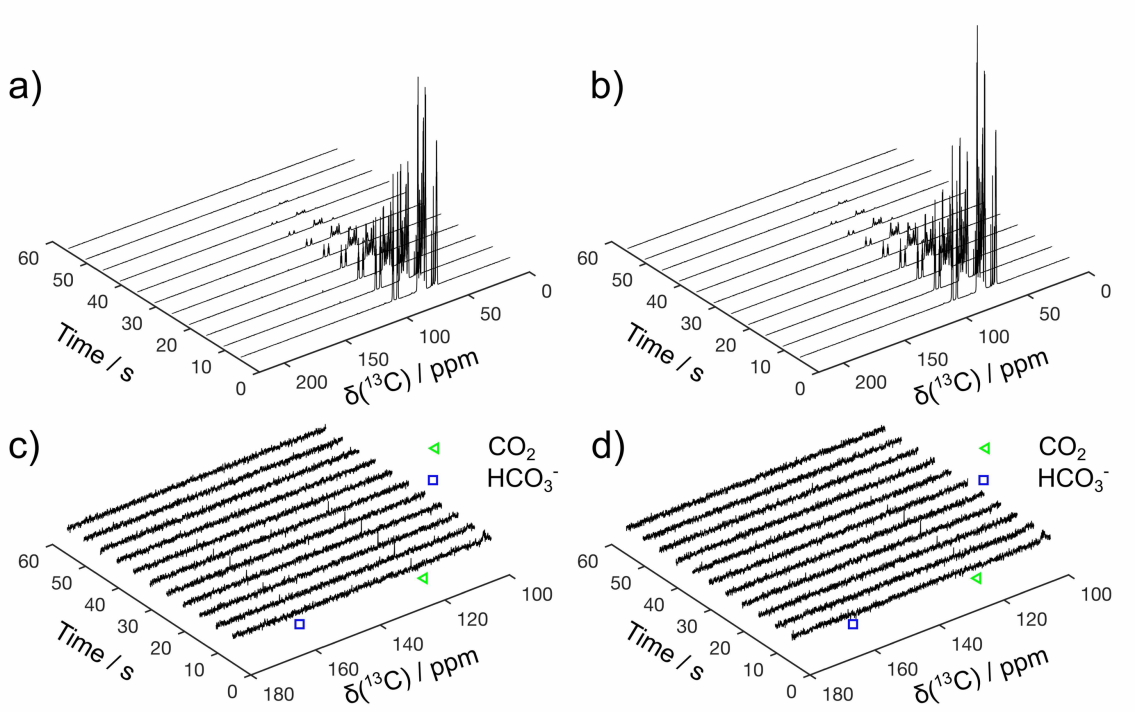

Figure 4.4. Time series of NMR spectra obtained after hyperpolarized [$^{2}H_{12}$,$^{13}C_{6}$]-glucose was mixed with electroporated (a) and non-electroporated (b) yeast cells. The experimental conditions were the same as pyruvate, with 5 µL 0.89 M glucose hyperpolarized instead. (c) and (d) are 10 times enlarged of (a) and (b) respectively, showing the product region. Reprinted with permission from [157].

In general, it is necessary to consider the internal compartmentalization of the cells in any experiment, where metabolites are introduced externally. Pyruvate is converted to CO_2 by the enzyme pyruvate decarboxylase, which is primarily located in the cytosol.[169,172] It can also enter the tricarboxylic acid cycle to form CO_2 by the action of pyruvate dehydrogenase in the mitochondria. When the pyruvate concentration is high, the cytosolic pathway was reported as dominant.[172] Therefore, in the present experiments, the kinetics of introduction into mitochondria was not further considered.

4.3.2. Quantification through Modeling

In order to quantify the differences observed with and without electroporation, the reaction model in Scheme 4.1 was used to fit the observed signals. In this model, the rate constant for transport of pyruvate to the intracellular environment is included in the apparent first order rate constant $k(\text{pyr}\rightarrow\text{CO}_2)$.[102,173] This first order assumption holds, when the substrate concentration [substrate] << K_M of the enzyme. When only a small fraction of substrate is consumed, this rate constant can also approximate a zeroth order reaction, where the enzyme operates at $V_{max} = k \cdot [\text{substrate}]_0$.

Scheme 4.1. Model to describe the change of NMR signal intensities. $k(\text{pyr}\rightarrow\text{CO}_2)$ is the conversion rate constant from pyruvate to CO_2 and $k(\text{CO}_2\rightarrow\text{HCO}_3^-)$ is the constant for conversion from CO_2 to HCO_3^-. $R_1(\text{pyr})$, $R_1(\text{CO}_2)$, and $R_1(\text{HCO}_3^-)$ are the T_1 relaxation rates for pyruvate, CO_2, and HCO_3^- respectively.

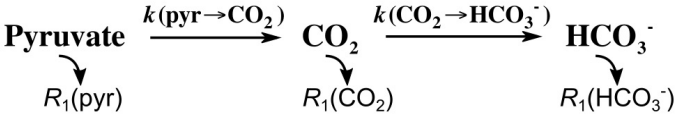

Between two successive pulses, NMR signals evolve following kinetic rate expressions and spin relaxation. For pyruvate, the signal depletion is dependent on relaxation and reaction consumption, $dS(\text{pyr})/dt = -[R_1(\text{pyr}) + k(\text{pyr}\rightarrow\text{CO}_2)]S(\text{pyr})$. The signal of CO_2 increases because of production from pyruvate and decreases due to conversion to HCO_3^- and relaxation, $dS(\text{CO}_2)/dt = k(\text{pyr}\rightarrow\text{CO}_2)S(\text{pyr}) - [R_1(\text{CO}_2) + k(\text{CO}_2\rightarrow\text{HCO}_3^-)]S(\text{CO}_2)$. HCO_3^- is produced from CO_2, and the signal decays via relaxation, $dS(\text{HCO}_3^-)/dt = k(\text{CO}_2\rightarrow\text{HCO}_3^-)S(\text{CO}_2) - R_1(\text{HCO}_3^-)S(\text{HCO}_3^-)$. The excitation

pulses cause an additional signal depletion of a factor of cos(α) for each pulse with flip angle α.

For fitting of this model to the observed signals, only the labeled C1 position in pyruvate was considered, since the observed product peaks originate from this carbon atom. R_1(pyr) and $k(CO_2 \rightarrow HCO_3^-)$ are assumed to be the same with and without electroporation, since the fraction of pyruvate consumed is small and no plasma membrane transport is expected for the conversion step $CO_2 \rightarrow HCO_3^-$. Therefore, an experiment with and an experiment without electroporation were combined into one set of data and fitted with six signal curves simultaneously. The two experiments in the set share the common unknown parameters R_1(pyr) and $k(CO_2 \rightarrow HCO_3^-)$, but are described by different $k(\text{pyr} \rightarrow CO_2)$. The fitted T_1 relaxation and kinetic rate constants were obtained by minimizing the sum of residual squares between calculated and measured data points. As in previous studies,[101,105,174] the signal of pyruvate hydrate is not included in the fitting. Pyruvate hydrate results from the reversible hydration of pyruvate in a non-enzymatic process and is not metabolized.[162] Its signal is less than 2 % of pyruvate in the present experiments. The results from three sets of data are shown in Figure 4.5, and the rate constants are given in the figure caption. Since the loaded cell concentrations differ slightly in each experiment, the rate constant values from each set of data were normalized to the final cell concentrations as determined by OD of the loaded cell suspension and the dilution factor during sample injection, and averaged. The result for $k(\text{pyr} \rightarrow CO_2)$ is $(4.71 \pm 0.86) \cdot 10^{-6}$ $s^{-1} \cdot OD^{-1}$ with electroporation and $(4.11 \pm 1.67) \cdot 10^{-7}$ $s^{-1} \cdot OD^{-1}$ without electroporation. The fitted value for $k(CO_2 \rightarrow HCO_3^-)$ is $(3.20 \pm 0.19) \cdot 10^{-4}$ $s^{-1} \cdot OD^{-1}$. The errors indicated are the standard deviations from three sets of data. The cell density of

W303 strain is about $2 \cdot 10^7$ cell / mL when $OD^{600} = 1$.[175] Therefore, the approximate observed values for the kinetic rate constants expressed per cell are $k(\text{pyr}\rightarrow\text{CO}_2) = 2.35 \cdot 10^{-13}$ $\text{s}^{-1}\cdot\text{cell}^{-1}$ with electroporation and $2.05 \cdot 10^{-14}$ $\text{s}^{-1}\cdot\text{cell}^{-1}$ without electroporation, and $k(\text{CO}_2\rightarrow\text{HCO}_3^-) = 1.60 \cdot 10^{-11}$ $\text{s}^{-1}\cdot\text{cell}^{-1}$.

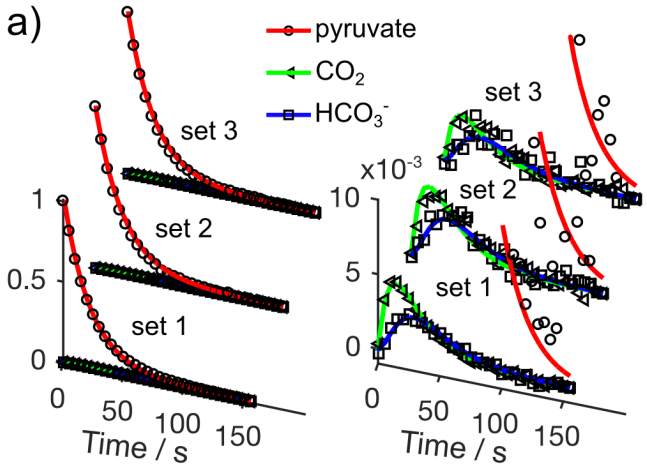

Figure 4.5. Fit of NMR signal intensities in the pyruvate metabolism, using kinetic equations derived from Scheme 4.1. a) Electroporated yeast cells mixed with hyperpolarized [1-^{13}C]-pyruvate. b) Non-electroporated yeast cells mixed with hyperpolarized [1-^{13}C]-pyruvate. The vertical axis is enlarged in the second panel in (a) and (b) to show the time evolution of product signals. From three sets of data, each comprising an experiment with and without electroporation, the optimized parameters are $k(\text{pyr}\rightarrow\text{CO}_2) = (4.96 \pm 0.14) \cdot 10^{-6}$, $(5.42 \pm 0.47) \cdot 10^{-6}$, and $(3.75 \pm 0.43) \cdot 10^{-6}$ $\text{s}^{-1}\cdot\text{OD}^{-1}$ with electroporation. $k(\text{pyr}\rightarrow\text{CO}_2) = (6.03 \pm 1.02) \cdot 10^{-7}$, $(3.08 \pm 3.40) \cdot 10^{-7}$, and $(3.21 \pm 3.46) \cdot 10^{-7}$ $\text{s}^{-1}\cdot\text{OD}^{-1}$ without electroporation. $k(\text{CO}_2\rightarrow\text{HCO}_3^-) = (3.01 \pm 0.13) \cdot 10^{-4}$, $(3.20 \pm 0.42) \cdot 10^{-4}$, and $(3.39 \pm 0.65) \cdot 10^{-4}$ $\text{s}^{-1}\cdot\text{OD}^{-1}$ was obtained. Ranges indicate 95 % fit confidence intervals calculated using the Jacobian matrix from the fitting. The large intervals of $k(\text{pyr}\rightarrow\text{CO}_2)$ without electroporation are due to the absence of the product signals under this experimental condition. Literature values $T_1(\text{CO}_2) = 50$ s and $T_1(\text{HCO}_3^-) = 24$ s were used as constants in the fit.[176–178] The fitted $T_1(\text{pyr}) = 64.3 \pm 4.3$ s, which is consistent with literature values of 42 – 68 s *in vitro*.[105,176] Reprinted with permission from [157].

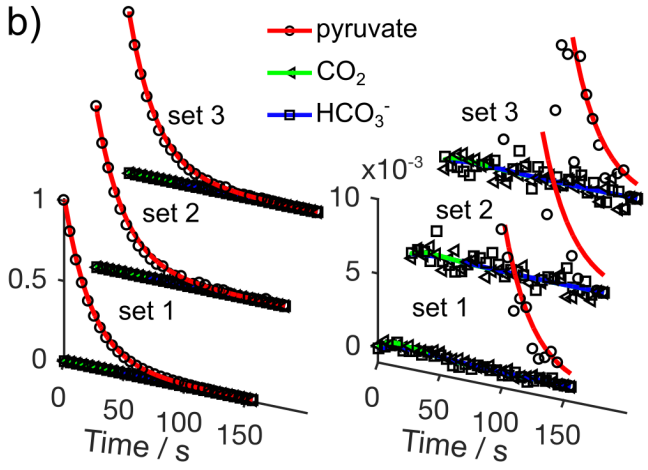

Figure 4.5. Continued.

These numbers indicate that k(pyr→CO_2) increases about twelve times through the use of electroporation to render the plasma membrane permeable. Based on these results, electroporation is shown to be an effective method to introduce hyperpolarized metabolites into cells in the absence of natural membrane transporters. The hyphenated electroporation system does not impose an additional delay time to the automatic liquid driven injection system, by collecting the ex-situ electroporated cells into the second sample loop. This method is therefore compatible with any compounds that can be hyperpolarized by D-DNP. Compared to manual mixing, the automated injection results in a shorter delay, and a higher polarization level can be preserved.

4.3.3. Discussion

The repeatability of the D-DNP experiment does not appear to be impacted by the electroporation pulse, as judged from the standard deviations. Compared to other protocols for introducing small molecules into cells, such as heat shock, the use of carriers, and overexpression of transport proteins, electroporation has several advantages.[179–182]

Electroporation can introduce various molecules into any cell type with high transfer efficiency. Most importantly, preparation requirements are minimal, since other reagents or sample components (*e.g.* viral vectors or lipid vesicles) or chemical / biological processing of cells is not needed.

To ensure that cells are in best possible condition at the time of the NMR measurement after electroporation, the hyperpolarized pyruvate was mixed with the electroporated yeast cells as little as 2 – 3 s after the high voltage pulse was applied. This time duration was chosen in accordance with a variability in the charging time of < 1 s of the power supply that was employed. It would be possible to further reduce this time delay with the use of a purpose designed power supply that allows for pre-charging. It would also be possible to perform electroporation after mixing with a flow cell electroporation device.[183] However, the recovery of openings on cell membranes requires at least several seconds.[184] This recovery time was confirmed under the conditions employed here by fluorescence microscopy measurements (see Figure 4.6). It was found that electroporated yeast cells can be stained with the fluorescent dye even after 12 s. As a control, the dye does not enter cells without electroporation even after mixing for several minutes. Therefore, the currently achieved time delay between the electroporation pulse and mixing appears sufficient for these experiments.

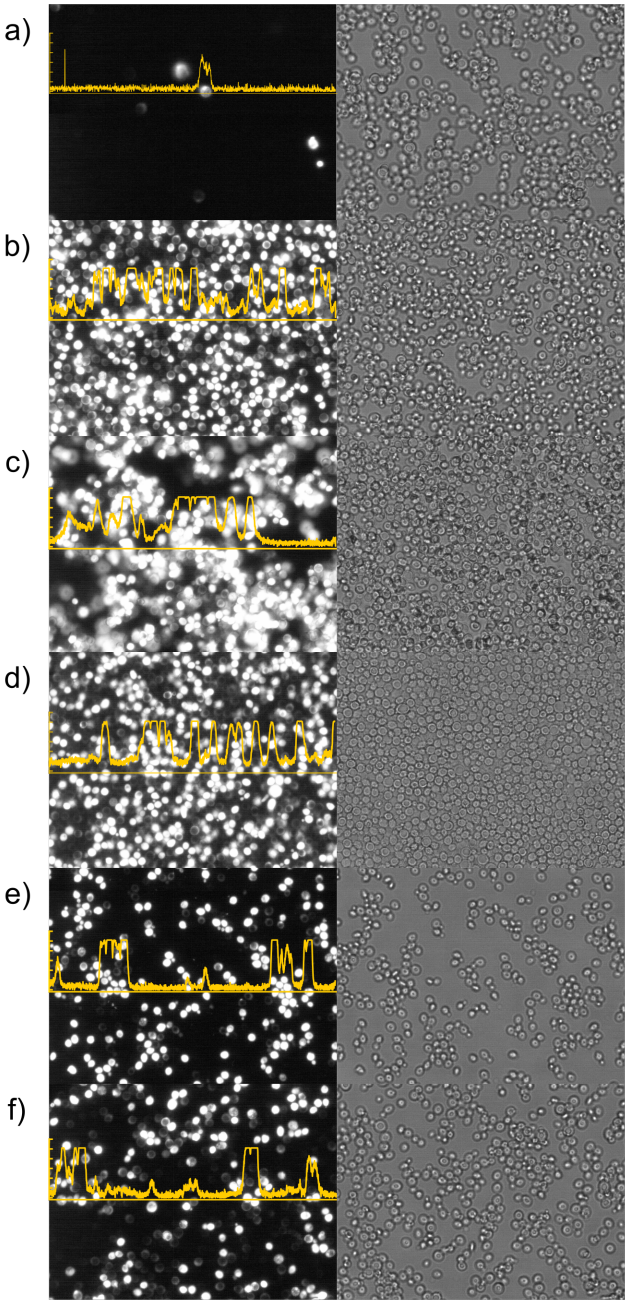

Figure 4.6. Fluorescence (left) and white light (right) images of yeast cells. a) Cells mixed with 0.1 mg / mL propidium iodide solution without electroporation. b) Cells mixed with propidium iodide solution and subsequently subjected to an electroporation pulse. Propidium iodide cannot pass through the intact plasma membrane.[185] The remaining panels show electroporated cells mixed with propidium iodide solution approximately (c) 3 s, (d) 6 s, (e) 9 s, and (f) 12 s after electroporation. In all cases, the electroporation pulse was applied with a time constant of 5 ms at a field strength of 800 V/mm. Reprinted with permission from [157].

A concern in the use of electroporation generally is whether cells remain viable after completion of the procedure. For yeast cells and using an electric field of 800 V/mm, viability was measured as 47 % by counting colony-forming units, which is close to a literature value of 50 %.[186] The D-DNP experiment is unique in that it probes a short time window of a few tens of seconds after electroporation. Even if cells ultimately do not remain viable, enzymes are still expected to be active. The physiological state of cells may ultimately change after electroporation, as the electric field can cause redox state changes and membrane pores can result in loss of some essential ions and small molecules.[187,188] For in cell measurements of enzyme activity, as demonstrated here on the example of enzymes in the pyruvate metabolism pathways, the electroporation based method however can be expected to yield accurate results on substrate turnover.

4.4. Conclusion

In summary, we compared signals of metabolic products after introduction of pyruvate hyperpolarized by D-DNP into yeast cells by simple mixing, or by electroporation. Electroporation alleviates the barrier for transport of metabolic precursors imposed by the cell membrane. Unlike glucose or fructose, pyruvate cannot be quickly absorbed into the yeast cells used in these experiments. As a result, simple mixing of cell suspensions with hyperpolarized pyruvate solution only resulted in product signals close to the lower limit of detection. With electroporation, approximately 8-fold stronger signals of the products were observed. The apparent conversion rate from pyruvate to CO_2 increased by a factor of about 12. These results demonstrate that incorporating electroporation into *in vitro* D-DNP experiments reduces the influence of membrane transport on observed rate constants. At the same time, it provides a versatile method to

facilitate the characterization of metabolic pathways using hyperpolarized molecules that may play vital roles in cells, but do not readily cross the cell membrane.

5. REAL-TIME NMR REACTION MONITORING USING SPATIAL ENCODING

Real-time NMR spectroscopy monitors reaction progress by following the time evolution of the resonance peaks. Between the measurement intervals of the reaction time course, a certain amount of time has to be reserved for data acquisition, averaging scans, and magnetization regeneration. Here, the limit of the reaction time resolution is extended through the combination of continuous-flow NMR and an ultrafast imaging pulse sequence. Using a purpose built mixer device for continuous flow NMR, signals are acquired downstream of the mixing of two reagents, reflecting the extent of the reaction. The reaction time is mapped to a spatial dimension in the direction of flow. The signals from the entire detection region are measured simultaneously in a single acquisition. The resulting reaction time resolution is the ratio of the spatial resolution and the linear flow velocity. In a demonstration of this method using an enzymatic reaction, the achieved time resolution is more than two times better than the acquisition time of a single scan. Using this method, the time resolution in reaction monitoring depends on sensitivity. Further time resolution improvements may in the future be achieved by sensitivity enhancement methods.

5.1. Introduction

Nuclear magnetic resonance spectroscopy (NMR) as an analytical technique combines the ability to determine chemical structure of large or small molecules, with the possibility for accurate quantitation through highly reproducible measurement of signal intensity. These qualities enable the use of NMR for measuring reaction kinetics and determining mechanisms. Early in the development of NMR applications in chemistry,

stopped-flow techniques for the monitoring of reactions have been demonstrated.[29] Since then, stopped-flow NMR has been applied in various fields, ranging from the determination of the mechanisms of polymer reactions[31] to protein folding.[189] Recently, its applicability has also been extended using the hyperpolarization of nuclear spins, which among other benefits allows the detection of low-sensitivity nuclei.[144,190] Regardless of the applications, stopped-flow techniques rely on acquiring data from samples in batches, which increases complexity and potentially limits throughput. These experiments also are subject to a dead-time for mixing and stabilization of a sample, which may be more substantial than with optical detection because of larger sample volumes and stringent requirements on sample homogeneity for NMR detection.

As an alternative to stopped-flow NMR, reactions may be characterized with continuously flowing reagents. The mixing method plays an important role in the reaction rates determined by NMR.[191] Continuous-flow or on-line NMR can overcome the sample inhomogeneity issue arising in stopped-flow NMR and give a more accurate kinetic result. On-line reaction monitoring is often performed using portable, low-field NMR systems.[192] Continuous flow mixers for use in standard, high-field NMR spectrometers are more directly applicable to studies determining reaction kinetics and mechanisms.[193] High-resolution spectra obtained with these devices enable distinguishing signals from reactants and products even in complex mixtures.[35] Continuous flow monitoring of reactions by NMR has also been demonstrated in a microfluidic context, where the required amount of sample is reduced, in one application enabling the monitoring of signal changes due to protein folding.[194]

When reactions are monitored *in situ* using static samples, the time resolution is primarily limited by the acquisition time. This limit can be overcome with continuous flow and magnetic resonance imaging (MRI). MRI has been used to measure the spatial distribution of reaction processes, such as in reactors and heterogeneous systems.[37] For example, MRI was used to image the process of a heterogeneous catalytic reaction, from the bottom to the top of a fixed-bed flowing reactor. Using this approach, the conversion rates and selectivity were compared at different radial and axial positions.[38] In continuous flow, the reaction at each spatial location is in a steady state corresponding to a reaction time that equals the flow time after mixing. Therefore, the reaction time coordinate can be mapped to the spatial coordinate downstream from the mixer. Signals from different reaction times can be read out with imaging methods. By decoupling reaction time from the real time of the experiment, an in principle unlimited number of acquisitions can be performed, which may be used for increasing time resolution, or obtaining correlation information such as with multidimensional spectroscopy. On the other hand, continuous flow in combination with an extended duration of readout results in a substantial consumption of reactant.

In this work, we introduce a method that makes use of ultrafast NMR imaging in continuos-flow NMR. The spectro-temporal encoding permits to read an entire data set in a single acquisition.[195] With a simple device for mixing a stream of pre-polarized reactant with a second reagent, we demonstrate the acquisition of kinetic data with high time resolution from an enzyme catalyzed reaction.

5.2. Materials and Methods

5.2.1. Mixer Device

A mixer device was designed for continuous flow NMR spectroscopy, with the provision to pre-polarize the nuclear spins of one of the reactants in the magnetic field. Hence, the device was made to fit into a narrow-bore NMR magnet with commercial shim system installed. The device contains two inlet channels for the two reactants (Figure 5.1a). The reactant to be observed passes through the middle inlet leading to the pre-polarization chamber (2.7 mL volume). The chamber provides an increased residence time of nominally 3 s at a flow rate of 50 mL·min^{-1} for spins to polarize in the magnetic field. The other reactant is injected through the second inlet and mixes with the first reactant downstream of the chamber. Immediately below, the mixture flows through a leading tube (1/32 inch outer and 0.02 inch inner diameter, IDEX Health & Science, Oak Harbor, WA) to the bottom of a standard 5 mm NMR tube inserted into the NMR probe. While the mixture flows upwards, the reaction is monitored. The spent reaction solution finally flows out from the return channel of the device and is collected in a waste container. The device was made from a cylinder of Delrin plastic with an outer diameter of 25 mm and a length of 75 mm (Online Metals, Seattle, WA). Channels of 1.6 mm width and depth were machined by computer numerical control (CNC) into a flat surface milled into the cylinder (A). Channels were sealed with a single gasket sheet made from nitrile rubber (McMaster-Carr, Elmhurst, IL). The cover (B) was attached with brass screws (4-40 unified thread standard). For leak tight inlet and outlet connections, vias extend below this surface to meet access holes drilled in the top and bottom surface of the cylinder.

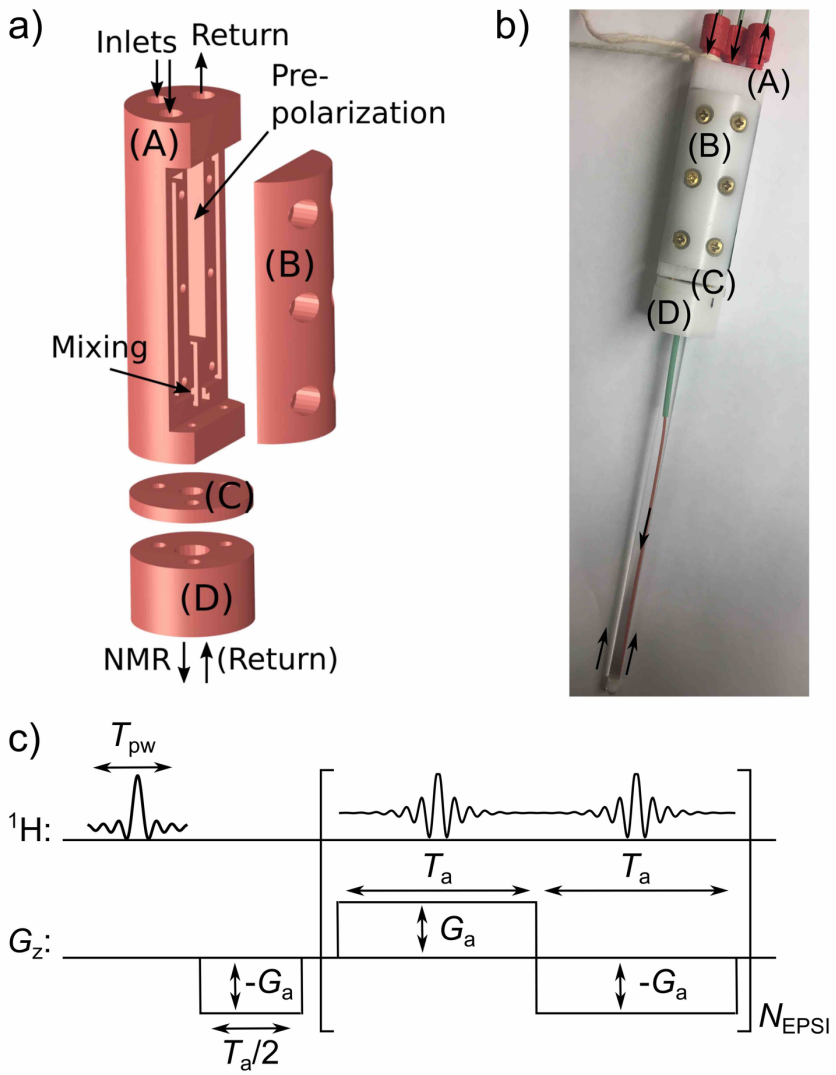

Figure 5.1. a) The design diagram of the mixer device for continuous-flow NMR spectroscopy and imaging, showing the channel substrate (A), cover plate (B), as well as NMR tube adapter consisting of sealing plate (C) and tube retainer (D). b) The fabricated device with a standard 5 mm NMR tube and fluid connectors attached. c) Pulse sequence used in spectro-temporal encoding of the reactant and product signals during the continuous flow reaction.

The NMR tube was attached below the mixer, using a nitrile O-ring between pieces (A) and (C), and a retaining ring permanently glued to the NMR tube between pieces (C) and (D). In the fabricated device (Figure 5.1b), the edge of the gasket inserted below the

cover can be seen. Mixing was improved with a cotton string held inside a section of the leading tube (green tubing, 1/16 inch outer and 1/32 inch inner diameter), acting as a porous plug. No fluid leaks were observed at all flow rates tested, up to 150 $mL \cdot min^{-1}$.

5.2.2. Pulse Sequences

The pulse sequence used to collect the two-dimensional time-resolved kinetic NMR spectra was an echo planar spectroscopic imaging (EPSI) sequence,[195] shown in Figure 5.1c. A polychromatic excitation pulse Pc9_4_90 was first used to selectively excite ^1H magnetization. The excitation bandwidth was selected as 400 Hz based on the EPSI signal profile (Figure 5.2), which corresponds to a duration T_{pw} of 18.78 ms. Magnetization then evolved under a so-called pre-phasing gradient with strength G_a for a time $T_a/2$. Subsequently, a pair of alternating bi-polar readout gradients, each having a duration T_a and strength $\pm G_a$ were used to collect a gradient-echo train. The bi-polar gradients were alternated for a total of N_{EPSI} times, in which $2N_{EPSI}$ gradient echoes are acquired in a one-dimensional fashion.

Experiments using a slice-selective pulse sequence were performed for comparison with the EPSI results. The pulse sequence consisted of *sup* – p1(G_z) – aq. A G4 Gauss-Cascade pulse p1 with a bandwidth of 15 kHz was used for selective excitation. Using a gradient G_z = 17.62 G/cm, a 2 mm slice was measured at a time. A total of 8 slices within the sensitive region of the NMR coil were measured successively, using frequency offsets covering a total of 105 kHz with a step of 15 kHz. A water suppression sequence (*sup*) consisting of a EBURP 2.1 shaped π/2 pulse followed by randomized pulsed field gradients G_x, G_y and G_z, was applied before the excitation pulse. During a data acquisition (aq) time of 1 s, a total of 6400 complex points were measured in one slice.

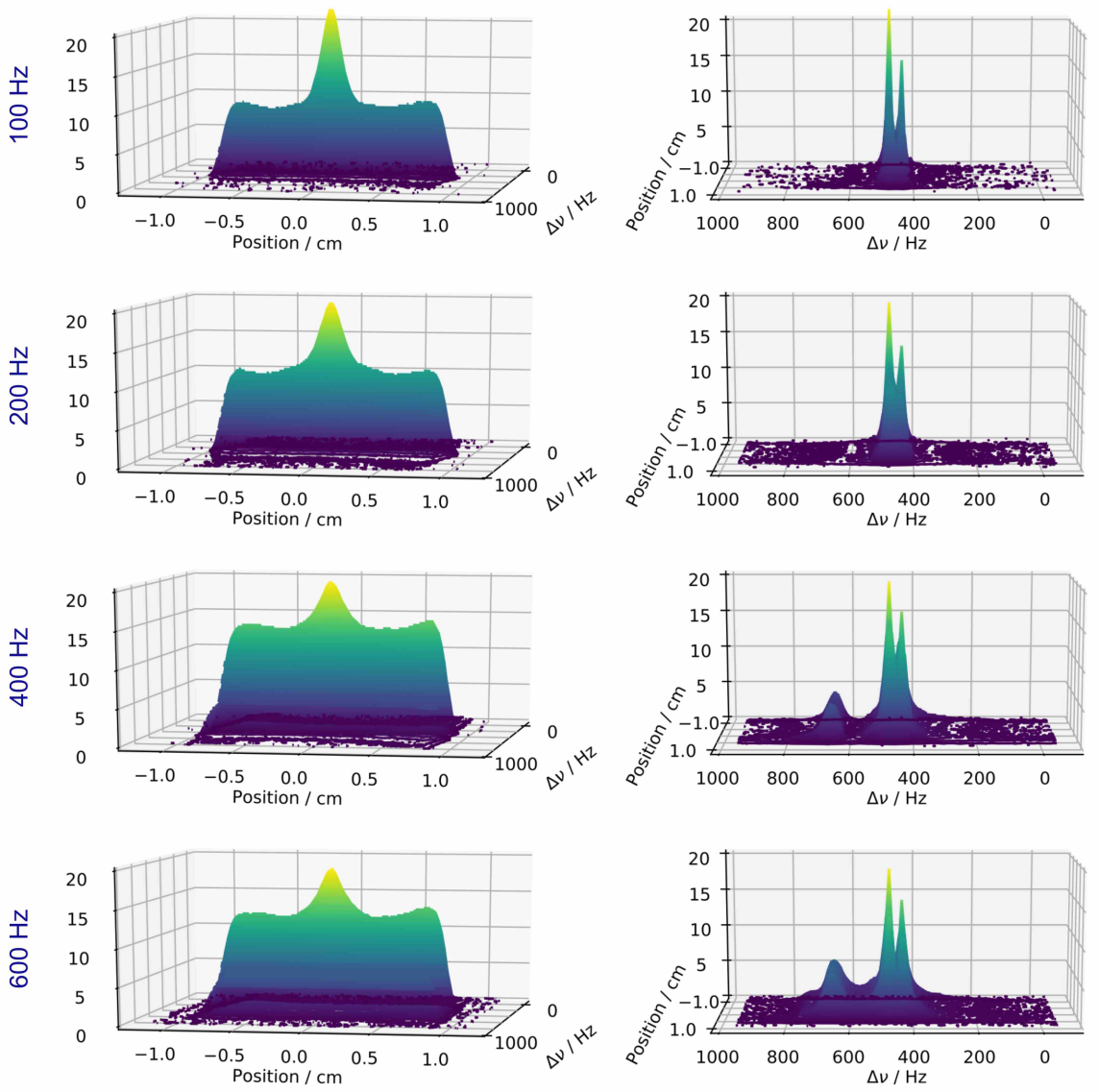

Figure 5.2. The EPSI signal profile with different excitation bandwidths. Two 3D angles of view are shown in the left and right columns respectively. A static sample was used, consisting of the substrate N-α-benzoyl arginine ethyl ester (BAEE) and the product ethanol. This dataset was acquired with the following acquisition parameters: TD = 40,000, N_{EPSI} = 100, T_a = 0.5 ms, G_a = 20.5 G/cm. Here, TD is the total number of real and imaginary data points. An excitation bandwidth of 400 Hz gives a relatively flat profile along the z axis and the strongest average signal. The same findings are observed with a different set of acquisition parameters: TD = 80,000, N_{EPSI} = 100, T_a = 1 ms, G_a = 20.5 G/cm.

5.2.3. Experimental Procedure

The substrate solution was prepared by dissolving N-α-benzoyl arginine ethyl ester (BAEE, TCI Chemicals, Tokyo, Japan) in 50 mM, pH 7.6 phosphate buffer. The enzyme trypsin (AMERSCO, Road Solon, OH) was dissolved in the same buffer at a concentration of 15 or 50 μM. 10% D_2O was added into the substrate solution for frequency locking of the NMR spectrometer. The substrate and enzyme solutions were injected into the mixer device with a 1:1 volume ratio by a syringe pump (Fusion 200 Touch, Chemyx, Stafford, TX). The NMR spectra were measured using a triple resonance TXI probe installed in a 400 MHz NMR spectrometer (Bruker Biospin, Billerica, MA).

5.2.4. Data Analysis

The two-dimensional EPSI data set was constructed by rearranging the one-dimensional gradient-echo vector into a 2D matrix by placing each gradient echo (composed of n points, with n = 100 or 200 in the experiments) into a distinct column. Therefore, the number of columns in the 2D data matrix is equal to the number of acquired gradient echoes, and the number of rows is equal to the number of points composing a single gradient echo. Next, the gradient echo in every odd column was corrected with a linear phase correction because these echoes were acquired with a positive gradient. Alternatively, this phase correction step was applied to process the echoes occupying the even columns. Finally, Fourier transform of each dimension was used to calculate the 1D spatial profile along the columns and the chemical shift along the rows, giving the so-called 2D EPSI NMR spectrum. The gradient-related wavenumber encoding position has opposite signs in the odd and even echoes, so the EPSI spectrum from the even echoes was reversed along the z axis and combined with the spectrum from the odd echoes. The

processed EPSI spectra are in magnitude mode. For spins undergoing both chemical change and unidirectional linear flow with a uniform velocity, the spatial dimension in the 2D EPSI NMR spectrum is mapped onto a time dimension representing the reaction time coordinate.

A static sample consisting of the reactant BAEE and the product ethanol was used to test the pulse sequence. In the 1D experiment, the integral ratio of ethanol over BAEE, α, is larger than 1 (Figure 5.3a). However, the BAEE peak is stronger in the EPSI spectrum (Figure 5.3b). Therefore, an correction profile was used to make the integral ratio of the two peaks the same as the 1D measurement. The peaks in the middle region are taller but narrower, so their integrals are smaller than those in the edge region (Figure 5.3c,d). The correction factor for BAEE was obtained as the averaged I_R / I_R; the correction factor for ethanol equals to the averaged I_R / $I_P \cdot \alpha$. The reactant and product integrals obtained using the same set of parameters were multiplied with this correction profile. The integral profile drops outside ± 0.7 cm, so only the signals within the sensitive region of ~ 1.4 cm were used in kinetic analysis. Since the total concentration of the reactant and the product is expected to be the same at every position, the reactant and product integrals were normalized before kinetic fitting: $S_R^n = S_R/(S_R + S_P)$, and $S_P^n = S_P/(S_R + S_P)$. The subscripts R and P denote the reactant and product, respectively.

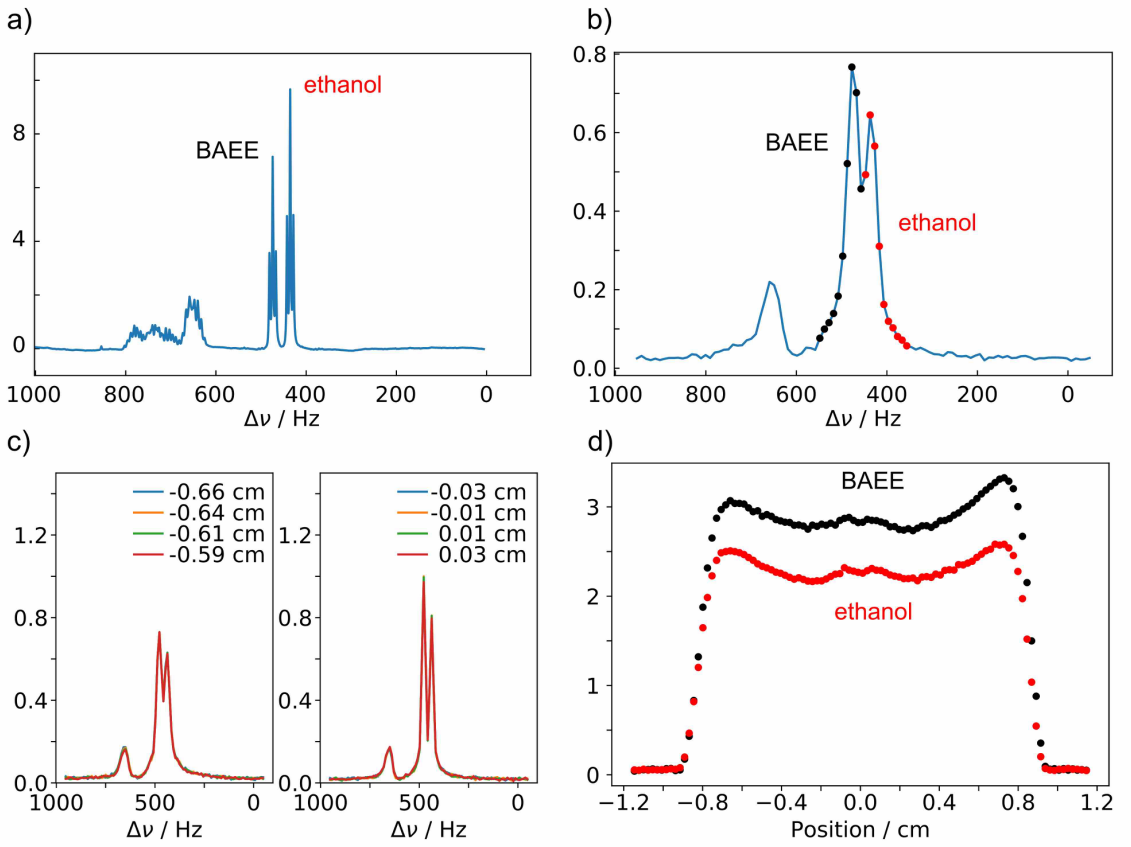

Figure 5.3. Integration of the reactant and product peaks. a) 1D spectrum of BAEE and ethanol. b) Integration ranges of the EPSI spectrum. The black markers denote the ranges for BAEE and the red markers for ethanol. c) Spectra from the edge (left) and middle (right) regions. d) The integrals of BAEE (I_R) and ethanol (I_P) are plotted against position.

5.3. Results and Discussion

5.3.1. Reaction Imaging Using EPSI

The enzymatically catalyzed hydrolysis of N-α-benzoyl arginine ethyl ester (BAEE) was chosen as a test reaction (Figure 5.4). A continuous flow of the substrate BAEE was provided through the pre-polarization channel of the mixer device, and the enzyme trypsin flowed through the second channel. NMR spectra were acquired with the EPSI and slice-selective pulse sequences from the mixture within the NMR tube attached to the mixer.

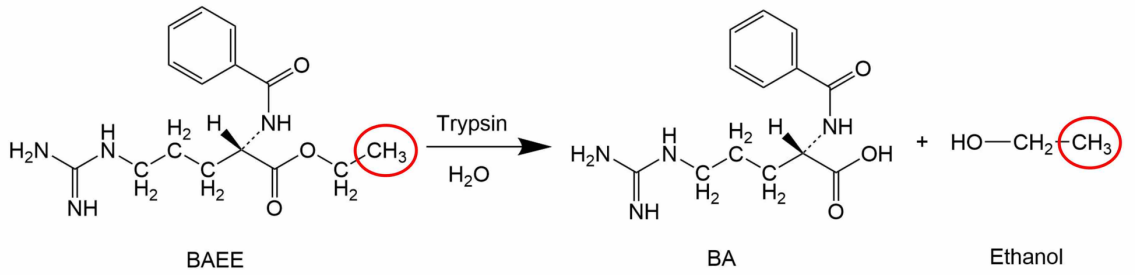

Figure 5.4. (a) Chemical structures of the substrate N-α-benzoyl arginine ethyl ester (BAEE), and reaction products benzoyl arginine (BA) and ethanol. The CH_3 groups observed in the experiments are circled in red.

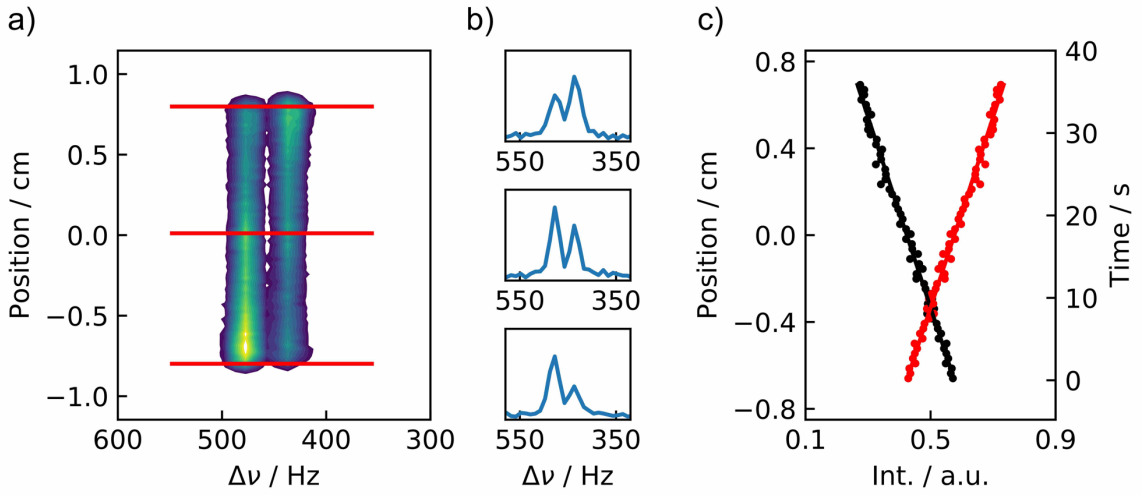

Figure 5.5. Reaction between 7.5 µM trypsin and 10 mM BAEE monitored using the ultrafast encoded EPSI pulse sequence. a) Contour plot showing the spatial imaging dimension on the vertical axis, and the ^{1}H NMR frequency dimension on the horizontal axis. b) 1D spectra corresponding to three positions along the spatial imaging dimension, indicated with red lines in (a). c) The spatial dimension is plotted against the integrated signal intensity (Int.) with fitting lines from the kinetic analysis (reactant: black; product: red). The right axis is mapped to the reaction time coordinate. The frequency selective excitation pulse was centered on 456 Hz. Frequency offsets ($\Delta\nu$) are indicated with respect to 400.13 MHz. 64 scans were averaged with a delay of 5 s.

Figure 5.5a shows the two-dimensional EPSI data set, monitoring the flow reaction between 10 mM BAEE and 7.5 µM trypsin. For this data set, $N_{EPSI} = 100$, $T_a = 0.5$ ms, $G_a = 20.5$ G/cm, and a total of 20,000 complex data points (TD = 40,000) were acquired. The

flow rate is 0.3 mL·min^{-1}. In the spectra taken from horizontal slices through the data set, a peak from the reactant BAEE is visible at 476 Hz, and a peak from the reaction product ethanol at 437 Hz. The contours in the two-dimensional graph show that the reactant peak decays while the product peak increases, as the reaction progresses from the bottom to the top of the detection region. Three cross-sections from the spatial dimension are plotted in Figure 5.5b, further showing the evolution of the reaction. In this data set, the field of view FOV = n / ($\gamma G_a T_a$) = 2.3 cm is imaged. Here, n is the number of data points in one gradient echo and also the size of the spatial dimension, which equals to TD / (4 N_{EPSI}). The spatial resolution is Δz = 1 / ($\gamma G_a T_a$) = 230 µm. With an inner diameter of the NMR tube of 4 mm, the linear velocity of the flow is v = 390 µm/s. These parameters result in a time resolution of $\Delta t = \Delta z / v$ = 580 ms after mapping the spatial dimension to the reaction time.

5.3.2. Kinetic Analysis

Integration of the peaks reveals the time dependence of the reaction seen in Figure 5.5c, showing the depletion of the reactant and the buildup of the product. Kinetic analysis was performed to extract the catalysis rate from the continuous flow measurements. Under conditions where the substrate concentration is much larger than the Michaelis-Menten constant, the rate of product formation is proportional to the total enzyme concentration, $\mathrm{d}[P] / \mathrm{d}t = k_{cat} \cdot [E]_0$. The parameter k_{cat} is the turnover number characterizing the catalyzed reaction. Therefore, the normalized integrals of the reactant and product follow $S_R^n = 1 / [R]_0 \cdot ([R]_0 - k_{cat} \cdot [E]_0 \cdot (t + t_0))$ and $S_P^n = 1 / [R]_0 \cdot k_{cat} \cdot [E]_0 \cdot (t + t_0)$, respectively. Here, $[R]_0$ and $[E]_0$ are the initial concentrations of BAEE and trypsin, and t_0 is the time difference after the start of the reaction and prior to the first fitted data point. The time t_0 accounts for the dead volume consisting of the mixing region in the mixer

device, the narrow tubing leading to the bottom of the NMR tube, and the volume of the NMR tube below the sensitive region of the coil. By minimizing the sum of the squared errors for reactant and product signal, k_{cat} and t_0 were fitted to the experimental data. The fitted lines are plotted together with the measured data points in Figure 5.5c. For the dataset shown, k_{cat} = 12.1 s^{-1}. From three repetitions, k_{cat} = 11.8 ± 0.5 s^{-1} and t_0 = 48 ± 3 s. The time t_0 corresponds to a dead volume of 240 µL.

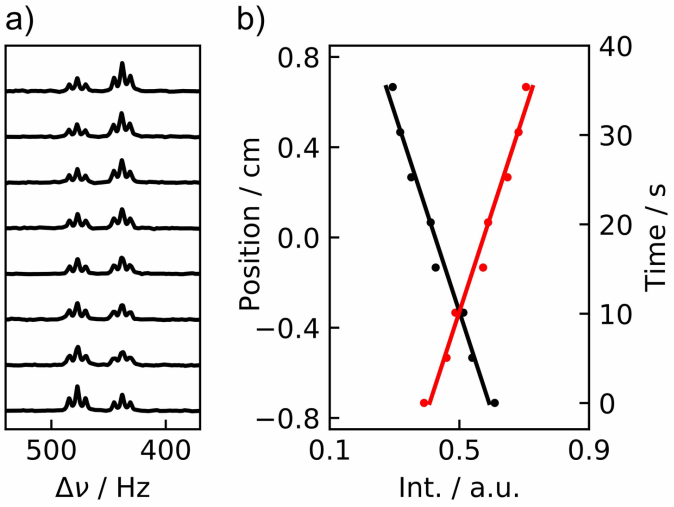

Figure 5.6. Spectra acquired with the slice-selective pulse sequence. The experimental conditions are the same as in Figure 5.5: 7.5 µM trypsin, 10 mM BAEE, and flow rate of 0.3 mL·min^{-1}. a) Spectra of the methyl group region. Each spectrum results from a 2 mm long slice along the vertical direction. The top spectrum corresponds to the longest reaction time near the top of the detection region. b) The spatial dimension (left axis) and the mapped reaction time coordinate (right axis) are plotted against the integrated signal intensity (Int.) with fitting lines from the kinetic analysis (reactant: black; product: red). For the shown dataset, k_{cat} = 12.0 s^{-1} and t_0 = 45 s.

The slice-selective experiment was measured to compare with the EPSI results. The same reaction concentrations and flow rate were used. The slice-selective spectra are shown in Figure 5.6. From three repetitions, k_{cat} = 11.7 ± 0.3 s^{-1} and t_0 = 47 ± 2 s were

obtained, showing a good agreement with the value from EPSI. These values also compare to a reference value of k_{cat} = 12 s^{-1} for this enzyme under similar conditions.[144,196]

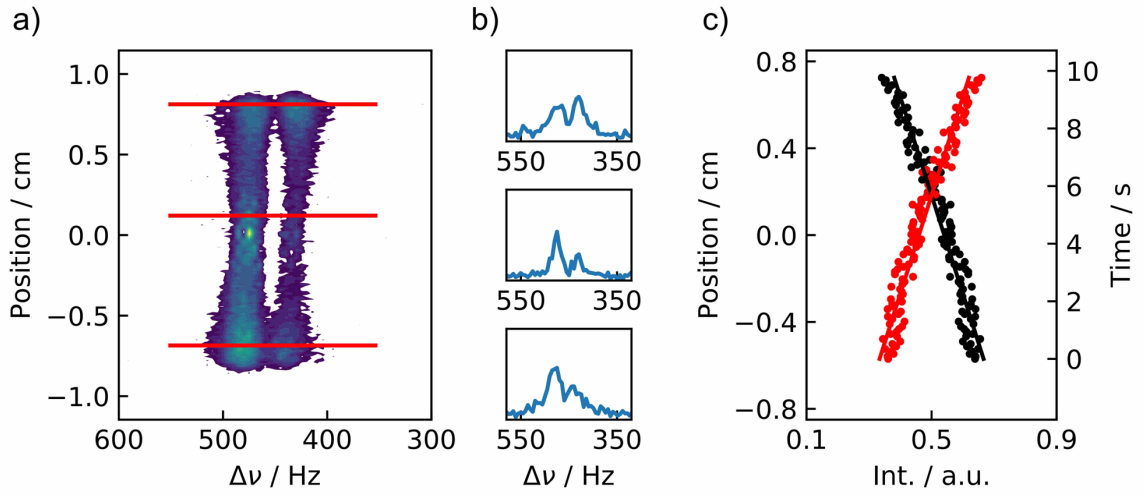

Figure 5.7. As in Figure 5.5, the EPSI spectra were measured during a flow reaction between 25 µM trypsin and 10 mM BAEE. For this data set, N_{EPSI} = 100, T_a = 1 ms, G_a = 20.5 G/cm, and TD = 80,000 (200 complex points per echo). The flow rate was 1 mL·min^{-1}. In this dataset, 240 averaging scans were used with a delay of 5 s. The fitting results are k_{cat} = 11.7 s^{-1} and t_0 = 11 s.

The EPSI pulse sequence allows for a time resolution that is increased compared to the dataset shown in Figure 5.5. Using T_a = 1 ms and TD = 80,000, the spatial resolution is twice finer, Δz = 115 µm. By further increasing the flow rate to 1 mL·min^{-1}, the time resolution Δt is reduced to 86 ms (Figure 5.7). Similarly to the above data, three repetitions under these conditions resulted in k_{cat} = 11.9 ± 0.3 s^{-1} and t_0 = 12 ± 1 s. The corresponding dead volume is 200 µL. The slice-selective spectra measured under the same conditions produced closely matched values, k_{cat} = 11.8 ± 0.2 s^{-1} and t_0 = 13 ± 1 s (three repetitions,

one data set is shown in Figure 5.8). Therefore, the error ranges of fitted k_{cat} from different sets of parameters and flow rates overlay.

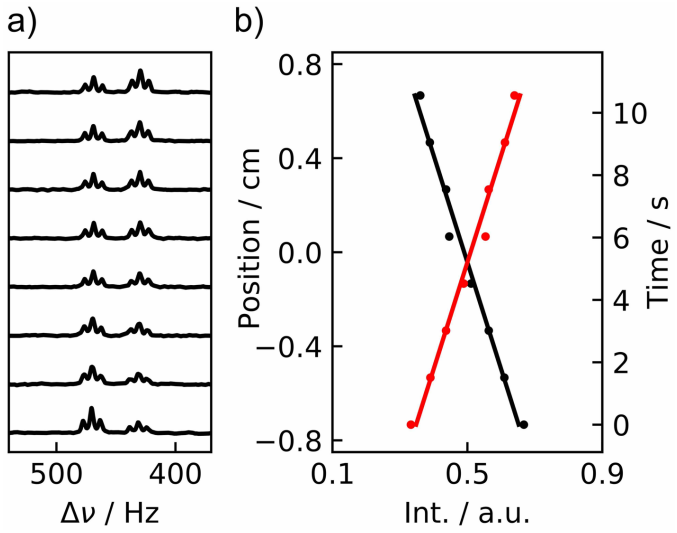

Figure 5.8. The slice-selective spectra were acquired under the same experimental conditions as in Figure 5.7: 25 μM trypsin, 10 mM BAEE, and flow rate of 1 mL·min^{-1}. In this dataset, the fitting results are k_{cat} = 11.7 s^{-1} and t_0 = 12 s.

The spectral resolution of the EPSI experiment in Figure 5.7 is $1/(2N_{EPSI}T_a)$ = 5 Hz, which would correspond to an acquisition time of 200 ms in a 1D measurement. Therefore, the nominal time resolution achieved by the EPSI sequence of 86 ms is finer than the resolution that could be achievable in a traditional stopped-flow experiment. Additionally, in the EPSI experiment, 200 different reaction time points were acquired at the same time with a total acquisition time of 0.2 s per scan.

5.3.3. Discussion

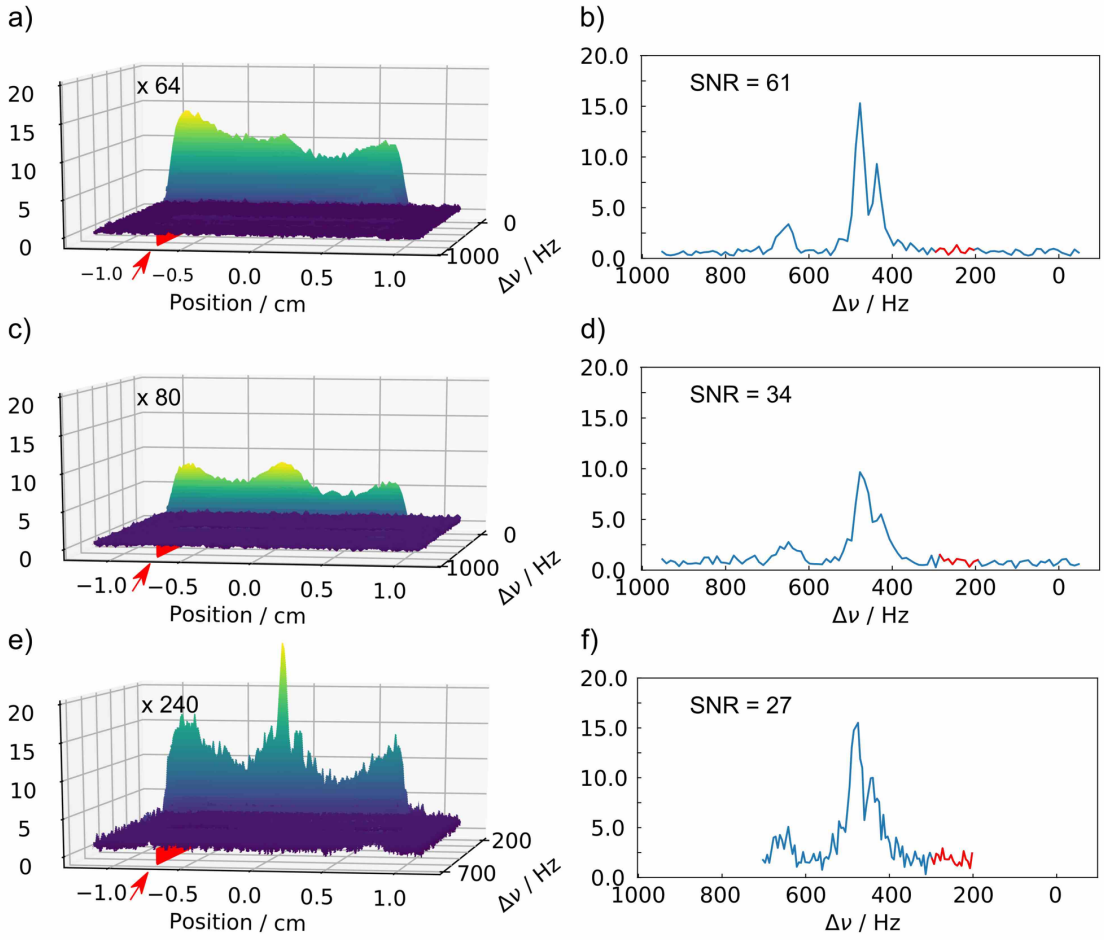

Figure 5.9. Signal to noise ratio (SNR) under different acquisition parameters and flow rates. 3D views of the measured EPSI spectra from three datasets are shown in the left column (a,c,e). The number of averaging scans is indicated. 1D spectra (b,d,f) with the SNR are plotted in the right column, taken from the position at -0.685 cm (the red slice, labeled by the red arrow in the 3D view). In the calculation of SNR, the maximum intensity was taken as the signal and the noise is the standard deviation of the 200 – 300 Hz range (plotted in red). A first set of acquisition parameters for a) and c) is: $N_{EPSI} = 100$, $T_a = 0.5$ ms, $G_a = 20.5$ G/cm, and TD = 40,000. A second set of parameters was applied for e): $N_{EPSI} = 100$, $T_a = 1$ ms, $G_a = 20.5$ G/cm, and TD = 80,000. The spatial distribution of reactant and product concentrations was intentionally kept similar when varying the flow rates, so that SNR at the same position can be compared. In the comparison, the relationship that SNR is proportional with the square root of the number of averaging scans is considered. The initial concentration of BAEE in all three datasets is 10 mM. For a), the flow rate was 0.3 mL·min^{-1} and the trypsin concentration $[E]_0 = 7.5$ µM; for c) and e), the flow rate was 1 mL·min^{-1} and $[E]_0 = 25$ µM.

The comparison of the data in Figure 5.5 and 5.7 illustrates that the signal to noise ratio (SNR) reduces with a finer spatial resolution (Δz) and a faster flow rate (v). The spatial distribution of reactant and product concentrations was intentionally kept similar under both conditions, by increasing the enzyme concentration and flow rate with a factor of 10/3. Regardless, at the higher flow rate, the SNR per scan at the position of -0.685 cm was 4.4 times smaller (shown in Figure 5.9a,e). This SNR reduction is consistent with the individual contributions from the spatial resolution and flow rates. SNR per scan reduces by 2 times when the flow rate increases by the factor of 10/3 without changing the spatial resolution (Figure 5.9 a,c). This signal loss possibly originates from imperfect gradient refocusing due to the spin position change. An additional reduction in SNR per scan of about 2.5 times was observed when the spatial resolution is decreased by a factor of two (Figure 5.10a,c). The reason is apparent that the total number of spins in one slice becomes less. Since $\Delta t = \Delta z / v$, it would be possible to further increase the time resolution by changing the spatial resolution and flow rate. The achievable sensitivity would ultimately limit the reaction time resolution. In the experiments shown, the dead volume was determined to be approximately 200 μL from the fitting. Part of this volume is from the mixing chamber and the leading tube, which contains a volume of several tens of microliters. The distance from the first data point within the sensitive region of NMR detection to the bottom of the NMR tube was ~ 1.2 cm, which corresponds to another volume of 150 μL. This volume may in the future be reduced by a different flow cell design. Turbulence was observed at the bottom when a red dye solution flowed out of the leading tube. This turbulence improves mixing of the reactants. If the initial reaction progress is to be monitored, minimization of this dead volume may also require a more

complicated mixer design. Using the present experimental setup, the measured reaction kinetics was found to be reproducible. The EPSI imaging pulse sequence samples different reaction time points simultaneously, and the continuous-flow design effectively prevents batch differences.

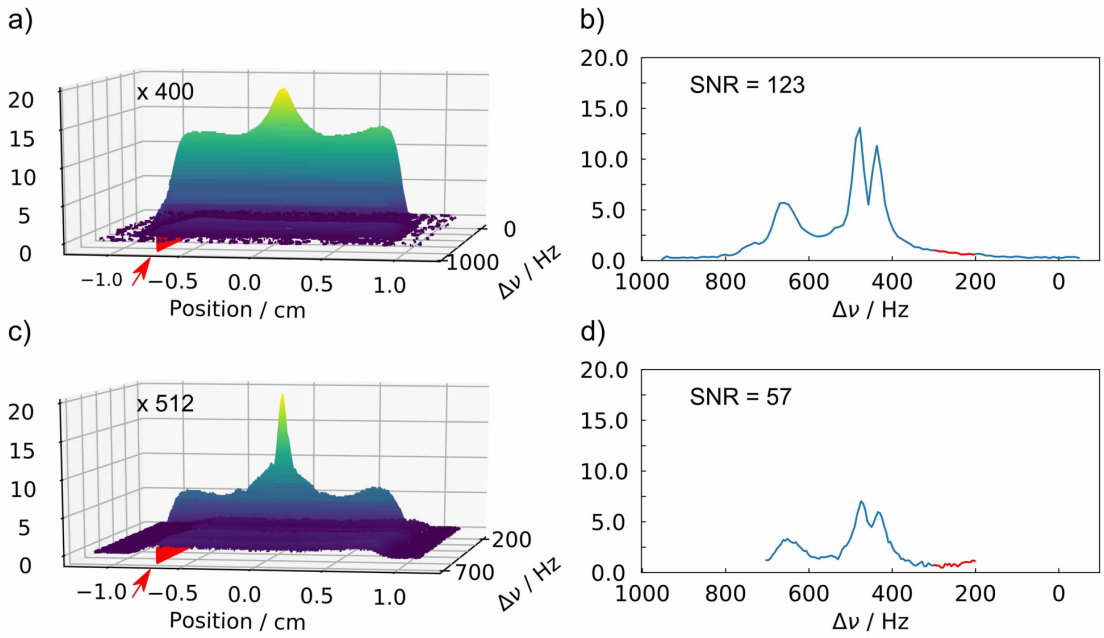

Figure 5.10. SNR comparison with different spatial resolutions. A static sample consisting of BAEE and ethanol was tested. As in Figure 5.9, the first and second sets of acquisition parameters were applied for a) and c) respectively. The spatial resolutions are 230 μm in a) and 115 μm in c).

5.4. Conclusion

In summary, the experiments demonstrated a method to increase the time resolution for reaction monitoring by NMR. An enzymatic reaction was followed by continuous-flow NMR with a purpose fabricated mixer device. An echo-planar spectroscopic imaging pulse sequence was used to map the spatial dimension to the

reaction time coordinate and provide chemical shift resolution. Different reaction time points along the flow direction were therefore measured simultaneously. The achievable time resolution was demonstrated to be a function of the detection sensitivity, thereby opening a possibility for monitoring reactions on an unprecedented time scale in combination with sensitivity enhancement techniques such as nuclear spin hyperpolarization.

6. SUMMARY

Nuclear magnetic resonance (NMR) signals can be enhanced by dissolution dynamic nuclear polarization (DNP) by up to 10,000 times or more compared to the thermally polarized experiment, which permits single-scan acquisitions with low sample concentrations. When the hyperpolarized magnetization is split by successive small flip angle pulses, the repetition interval is shortened to the order of 0.1 s, since polarization regeneration or averaging is not needed. This allows real-time NMR to follow non-equilibrium processes that occur within seconds or minutes. In this dissertation, DNP-NMR methods were developed to rapidly characterize biochemical transformations. These transformations include ligand-protein binding governed by the chemical exchange process that happens on the millisecond time scale, and fast biochemical reactions that occurs within a few minutes.

The high polarization from dissolution DNP is generated in a second magnet and is non-renewable, which presents challenges for experiments requiring multiple data points. These challenges can be overcome using multi-channel detection, as demonstrated in the protein-ligand interaction experiment of this dissertation. A dual-channel spectroscopy was implemented to measure R_2 rates at two pulsing limits simultaneously. An exchange term that contains kinetic parameters in the chemical exchange dynamics was therefore determined from a single hyperpolarization. In this experiment, a protein concentration of as low as 1 μM was used. The reduced sample amount benefits from the high sensitivity provided by DNP, which is desirable in applications such as screening in drug discovery. The usage of hyperpolarized relaxation dispersion experiments can be

extended to characterize different exchange processes including conformational change and oligomerization, as well as to determine the corresponding mechanism. The multi-channel spectroscopy can also measure multiple data points for other experiments with a single hyperpolarization.

In real-time DNP-NMR, relaxation complicates the data analysis, but also contains valuable structural information. In this dissertation, kinetic and relaxation rates were obtained from a metalloenzyme catalyzed reaction with paramagnetic metal ion substitution. Based on the paramagnetic relaxation effect, distances from the ^{13}C labeled product positions to the metal center in the enzyme-product complex were derived. The experiment shows that paramagnetic relaxation of hyperpolarized spins can be used to measure distances and other information, on intermediates or minor populations, even in non-equilibrium systems. Paramagnetic relaxation can also be used to probe intramolecular or intermolecular interactions in DNP-NMR experiments. Diamagnetic target molecules can further be tagged with paramagnetic metal complexes.

Relaxation limits the time window of DNP-NMR experiments. The signals from downstream metabolites cannot be observed if the hyperpolarized substrates enter into cells slowly. In this dissertation, this problem was solved by hyphenating an electroporator with the automatic injector system. Membrane openings created by the electroporation pulse led to the rapid introduction of the hyperpolarized precursor into cells, making the downstream product signals observable within the detection time window. Kinetic modeling further revealed that the apparent conversion rate increased about 12-fold in the presence of electroporation. The hyphenation of the electroporator enables metabolism monitoring for hyperpolarized precursors with low cell membrane permeability. Since

electroporation can introduce arbitrary substrates to the living cells, other in-cell transformations such as protein-ligand interactions can be probed by DNP-NMR.

In real-time NMR, the time resolution is limited to be longer than the acquisition time. In the final part of this dissertation, it was demonstrated that the combination of continuos-flow reaction and an ultra-fast imaging pulse can achieve unprecedented time resolution. Inhomogeneous mixing and batch-to-batch differences can also be avoided with this method. Provided that a sufficiently high SNR is achieved, the time resolution can be further increased. This experiment can be used to discover short-lived intermediates and measure the time profiles.

To conclude, NMR methods were developed in this dissertation to characterize rapid biochemical transformations with the aid of dissolution DNP. The measurement of relaxation dispersion and paramagnetic relaxation by DNP-NMR was demonstrated for the first time. Purpose-built instrumentation, such as the multi-channel spectrometer and the hyphenation of an electroporator, was used to realize different applications. In all experiments, modeling enabled the determination of kinetic rate constants as well as other parameters. These developments can enhance the applicability of dissolution DNP to a broader range of reactions and interactions. Using these methods, more information on reaction kinetics, mechanisms, and intermediates can be obtained rapidly.

REFERENCES

(1) Binsch, G.; Kessler, H. The Kinetic and Mechanistic Evaluation of NMR Spectra. New Analytical Methods (18). *Angew. Chem. Int. Ed. Engl.* **1980**, *19* (6), 411–428.

(2) Torchia, D. A. NMR Studies of Dynamic Biomolecular Conformational Ensembles. *Prog. Nucl. Magn. Reson. Spectrosc.* **2015**, *84–85*, 14–32.

(3) Bifulco, G.; Dambruoso, P.; Gomez-Paloma, L.; Riccio, R. Determination of Relative Configuration in Organic Compounds by NMR Spectroscopy and Computational Methods. *Chem. Rev.* **2007**, *107* (9), 3744–3779.

(4) Li, X.; Hopmann, K. H.; Hudecová, J.; Isaksson, J.; Novotná, J.; Stensen, W.; Andrushchenko, V.; Urbanová, M.; Svendsen, J.-S.; Bouř, P.; et al. Determination of Absolute Configuration and Conformation of a Cyclic Dipeptide by NMR and Chiral Spectroscopic Methods. *J. Phys. Chem. A* **2013**, *117* (8), 1721–1736.

(5) Bharti, S. K.; Roy, R. Quantitative ^{1}H NMR Spectroscopy. *TrAC Trends Anal. Chem.* **2012**, *35*, 5–26.

(6) Kleckner, I. R.; Foster, M. P. An Introduction to NMR-Based Approaches for Measuring Protein Dynamics. *Biochim. Biophys. Acta* **2011**, *1814* (8), 942–968.

(7) Sapienza, P. J.; Lee, A. L. Using NMR to Study Fast Dynamics in Proteins: Methods and Applications. *Curr. Opin. Pharmacol.* **2010**, *10* (6), 723–730.

(8) Palmer, A. G.; Massi, F. Characterization of the Dynamics of Biomacromolecules Using Rotating-Frame Spin Relaxation NMR Spectroscopy. *Chem. Rev.* **2006**, *106* (5), 1700–1719.

(9) Walinda, E.; Morimoto, D.; Sugase, K. Overview of Relaxation Dispersion NMR Spectroscopy to Study Protein Dynamics and Protein-Ligand Interactions: Relaxation Dispersion NMR Spectroscopy. *Curr. Protoc. Protein Sci.* **2018**, *92* (1), e57.

(10) Rennella, E.; Cutuil, T.; Schanda, P.; Ayala, I.; Forge, V.; Brutscher, B. Real-Time NMR Characterization of Structure and Dynamics in a Transiently Populated Protein Folding Intermediate. *J. Am. Chem. Soc.* **2012**, *134* (19), 8066–8069.

(11) Nikolaou, P.; Goodson, B. M.; Chekmenev, E. Y. NMR Hyperpolarization Techniques for Biomedicine. *Chem. Weinh. Bergstr. Ger.* **2015**, *21* (8), 3156–3166.

(12) Kovtunov, K. V.; Pokochueva, E. V.; Salnikov, O. G.; Cousin, S. F.; Kurzbach, D.; Vuichoud, B.; Jannin, S.; Chekmenev, E. Y.; Goodson, B. M.; Barskiy, D. A.; et al. Hyperpolarized NMR Spectroscopy: *D*-DNP, PHIP, and SABRE Techniques. *Chem. - Asian J.* **2018**, *13* (15), 1857–1871.

(13) Abragam, A.; Goldman, M. Principles of Dynamic Nuclear Polarisation. *Rep. Prog. Phys.* **1978**, *41* (3), 395–467.

(14) Ardenkjaer-Larsen, J. H.; Fridlund, B.; Gram, A.; Hansson, G.; Hansson, L.; Lerche, M. H.; Servin, R.; Thaning, M.; Golman, K. Increase in Signal-to-Noise Ratio of > 10,000 Times in Liquid-State NMR. *Proc. Natl. Acad. Sci.* **2003**, *100* (18), 10158–10163.

(15) Natterer, J.; Bargon, J. Parahydrogen Induced Polarization. *Prog. Nucl. Magn. Reson. Spectrosc.* **1997**, *31* (4), 293–315.

(16) Duckett, S. B.; Mewis, R. E. Application of *Para* Hydrogen Induced Polarization Techniques in NMR Spectroscopy and Imaging. *Acc. Chem. Res.* **2012**, *45* (8), 1247–1257.

(17) Adams, R. W.; Aguilar, J. A.; Atkinson, K. D.; Cowley, M. J.; Elliott, P. I. P.; Duckett, S. B.; Green, G. G. R.; Khazal, I. G.; López-Serrano, J.; Williamson, D. C. Reversible Interactions with Para-Hydrogen Enhance NMR Sensitivity by Polarization Transfer. *Science* **2009**, *323* (5922), 1708–1711.

(18) Mewis, R. E. Developments and Advances Concerning the Hyperpolarisation Technique SABRE: Developments and Advances Concerning the Hyperpolarisation Technique SABRE. *Magn. Reson. Chem.* **2015**, *53* (10), 789–800.

(19) Mok, K. H.; Nagashima, T.; Day, I. J.; Jones, J. A.; Jones, C. J. V.; Dobson, C. M.; Hore, P. J. Rapid Sample-Mixing Technique for Transient NMR and Photo-CIDNP Spectroscopy: Applications to Real-Time Protein Folding. *J. Am. Chem. Soc.* **2003**, *125* (41), 12484–12492.

(20) Goez, M. Photo-CIDNP Spectroscopy. In *Annual Reports on NMR Spectroscopy*; Elsevier, 2009; Vol. 66, pp 77–147.

(21) Mompeán, M.; Sánchez-Donoso, R. M.; de la Hoz, A.; Saggiomo, V.; Velders, A. H.; Gomez, M. V. Pushing Nuclear Magnetic Resonance Sensitivity Limits with Microfluidics and Photo-Chemically Induced Dynamic Nuclear Polarization. *Nat. Commun.* **2018**, *9* (1).

(22) Cavanagh, J.; Fairbrother, Wayne. J.; Palmer III, A. G.; Rance, M.; Skelton, N. J. *Protein NMR Spectroscopy: Principles and Practice*, 2nd ed.; Academic Press: Amsterdam, 2007.

(23) Kowalewski, J.; Mäler, L. *Nuclear Spin Relaxation in Liquids: Theory, Experiments, and Applications*, Second edition.; CRC Press, Taylor & Francis Group: Boca Raton, 2018.

(24) Schanda, P.; Brutscher, B. Very Fast Two-Dimensional NMR Spectroscopy for Real-Time Investigation of Dynamic Events in Proteins on the Time Scale of Seconds. *J. Am. Chem. Soc.* **2005**, *127* (22), 8014–8015.

(25) Gal, M.; Mishkovsky, M.; Frydman, L. Real-Time Monitoring of Chemical Transformations by Ultrafast 2D NMR Spectroscopy. *J. Am. Chem. Soc.* **2006**, *128* (3), 951–956.

(26) Hyberts, S. G.; Arthanari, H.; Wagner, G. Applications of Non-Uniform Sampling and Processing. *Top. Curr. Chem.* **2012**, *316*, 125–148.

(27) Wu, Y.; D'Agostino, C.; Holland, D. J.; Gladden, L. F. *In Situ* Study of Reaction Kinetics Using Compressed Sensing NMR. *Chem Commun* **2014**, *50* (91), 14137–14140.

(28) Walsh, D. J.; Lau, S. H.; Hyatt, M. G.; Guironnet, D. Kinetic Study of Living Ring-Opening Metathesis Polymerization with Third-Generation Grubbs Catalysts. *J. Am. Chem. Soc.* **2017**, *139* (39), 13644–13647.

(29) Kühne, R. O.; Schaffhauser, T.; Wokaun, A.; Ernst, R. R. Study of Transient Chemical Reactions by NMR. Fast Stopped-Flow Fourier Transform Experiments. *J. Magn. Reson. 1969* **1979**, *35* (1), 39–67.

(30) Hoeltzli, S. D.; Frieden, C. Stopped-Flow NMR Spectroscopy: Real-Time Unfolding Studies of 6-19F-Tryptophan-Labeled Escherichia Coli Dihydrofolate Reductase. *Proc. Natl. Acad. Sci.* **1995**, *92* (20), 9318–9322.

(31) Christianson, M. D.; Tan, E. H. P.; Landis, C. R. Stopped-Flow NMR: Determining the Kinetics of [*Rac*-(C_2H_4(1-Indenyl)$_2$)ZrMe][MeB(C_6F_5)$_3$]-Catalyzed Polymerization of 1-Hexene by Direct Observation. *J. Am. Chem. Soc.* **2010**, *132* (33), 11461–11463.

(32) Hoeltzli, S. D.; Ropson, I. J.; Frieden, C. Application of Equilibrium and Stopped-Flow ^{19}F NMR Spectroscopy to Protein Folding: Studies of E. Coli Dihydrofolate Reductase. In *Techniques in Protein Chemistry*; Elsevier, 1994; Vol. 5, pp 455–465.

(33) Picard, B.; Gouilleux, B.; Lebleu, T.; Maddaluno, J.; Chataigner, I.; Penhoat, M.; Felpin, F.-X.; Giraudeau, P.; Legros, J. Oxidative Neutralization of Mustard-Gas Simulants in an On-Board Flow Device with In-Line NMR Monitoring. *Angew. Chem. Int. Ed.* **2017**, *56* (26), 7568–7572.

(34) Maiwald, M.; Fischer, H. H.; Kim, Y.-K.; Albert, K.; Hasse, H. Quantitative High-Resolution on-Line NMR Spectroscopy in Reaction and Process Monitoring. *J. Magn. Reson.* **2004**, *166* (2), 135–146.

(35) Foley, D. A.; Bez, E.; Codina, A.; Colson, K. L.; Fey, M.; Krull, R.; Piroli, D.; Zell, M. T.; Marquez, B. L. NMR Flow Tube for Online NMR Reaction Monitoring. *Anal. Chem.* **2014**, *86* (24), 12008–12013.

(36) Feindel, K. W. Spatially Resolved Chemical Reaction Monitoring Using Magnetic Resonance Imaging. *Magn. Reson. Chem.* **2016**, *54* (6), 429–436.

(37) Britton, M. M. MRI of Chemical Reactions and Processes. *Prog. Nucl. Magn. Reson. Spectrosc.* **2017**, *101*, 51–70.

(38) Akpa, B. S.; Mantle, M. D.; Sederman, A. J.; Gladden, L. F. *In Situ* ^{13}C DEPT-MRI as a Tool to Spatially Resolve Chemical Conversion and Selectivity of a Heterogeneous Catalytic Reaction Occurring in a Fixed-Bed Reactor. *Chem. Commun.* **2005**, No. 21, 2741.

(39) Bray, J. M.; Davenport, A. J.; Ryder, K. S.; Britton, M. M. Quantitative, In Situ Visualization of Metal-Ion Dissolution and Transport Using ^{1}H Magnetic Resonance Imaging. *Angew. Chem. Int. Ed.* **2016**, *55* (32), 9394–9397.

(40) Kumar, A.; Balbach, J. Real-Time Protein NMR Spectroscopy and Investigation of Assisted Protein Folding. *Biochim. Biophys. Acta BBA - Gen. Subj.* **2015**, *1850* (10), 1965–1972.

(41) Rennella, E.; Brutscher, B. Fast Real-Time NMR Methods for Characterizing Short-Lived Molecular States. *ChemPhysChem* **2013**, *14* (13), 3059–3070.

(42) Blackmond, D. G. Kinetic Profiling of Catalytic Organic Reactions as a Mechanistic Tool. *J. Am. Chem. Soc.* **2015**, *137* (34), 10852–10866.

(43) Furukawa, A.; Nagata, T.; Matsugami, A.; Habu, Y.; Sugiyama, R.; Hayashi, F.; Kobayashi, N.; Yokoyama, S.; Takaku, H.; Katahira, M. Structure, Interaction and Real-Time Monitoring of the Enzymatic Reaction of Wild-Type APOBEC3G. *EMBO J.* **2009**, *28* (4), 440–451.

(44) Zhao, N.; Qiu, L.; Wang, X.; Li, J.; Jiang, Y.; Wan, X. Trifluoroacetic Acid Catalyzed Dibenzodiazocine Synthesis: Optimization and Mechanism Study. *Tetrahedron* **2012**, *68* (47), 9665–9671.

(45) Gallinger, A.; Biet, T.; Pellerin, L.; Peters, T. Insights into Neuronal Cell Metabolism Using NMR Spectroscopy: Uridyl Diphosphate N-Acetyl-Glucosamine as a Unique Metabolic Marker. *Angew. Chem. Int. Ed.* **2011**, *50* (49), 11672–11674.

(46) Dolinski, N. D.; Page, Z. A.; Eisenreich, F.; Niu, J.; Hecht, S.; Read de Alaniz, J.; Hawker, C. J. A Versatile Approach for In Situ Monitoring of Photoswitches and Photopolymerizations. *ChemPhotoChem* **2017**, *1* (4), 125–131.

(47) Jutz, F.; Buchard, A.; Kember, M. R.; Fredriksen, S. B.; Williams, C. K. Mechanistic Investigation and Reaction Kinetics of the Low-Pressure Copolymerization of Cyclohexene Oxide and Carbon Dioxide Catalyzed by a Dizinc Complex. *J. Am. Chem. Soc.* **2011**, *133* (43), 17395–17405.

(48) Nadim, E.; Bouhendi, H.; Ziaee, F.; Nouri, A. Kinetic Study of the Aqueous Free-Radical Polymerization of 2-Acrylamido-2-Methyl-1-Propanesulfonic Acid via an Online Proton Nuclear Magnetic Resonance Technique. *J. Appl. Polym. Sci.* **2012**, *126* (1), 156–161.

(49) Du, X.; Li, Y.; Xia, Y.-L.; Ai, S.-M.; Liang, J.; Sang, P.; Ji, X.-L.; Liu, S.-Q. Insights into Protein–Ligand Interactions: Mechanisms, Models, and Methods. *Int. J. Mol. Sci.* **2016**, *17* (2), 144.

(50) Clore, G. M. Exploring Sparsely Populated States of Macromolecules by Diamagnetic and Paramagnetic NMR Relaxation. *Protein Sci.* **2011**, *20* (2), 229–246.

(51) Meyer, B.; Peters, T. NMR Spectroscopy Techniques for Screening and Identifying Ligand Binding to Protein Receptors. *Angew. Chem. Int. Ed.* **2003**, *42* (8), 864–890.

(52) Angulo, J.; Nieto, P. M. STD-NMR: Application to Transient Interactions between Biomolecules—a Quantitative Approach. *Eur. Biophys. J.* **2011**, *40* (12), 1357–1369.

(53) Rama Krishna, N.; Jayalakshmi, V. Complete Relaxation and Conformational Exchange Matrix Analysis of STD-NMR Spectra of Ligand–Receptor Complexes. *Prog. Nucl. Magn. Reson. Spectrosc.* **2006**, *49* (1), 1–25.

(54) Szczepina, M. G.; Bleile, D. W.; Pinto, B. M. Investigation of the Binding of a Carbohydrate-Mimetic Peptide to Its Complementary Anticarbohydrate Antibody by STD-NMR Spectroscopy and Molecular-Dynamics Simulations. *Chem. - Eur. J.* **2011**, *17* (41), 11446–11455.

(55) Pérez-Victoria, I.; Kemper, S.; Patel, M. K.; Edwards, J. M.; Errey, J. C.; Primavesi, L. F.; Paul, M. J.; Claridge, T. D. W.; Davis, B. G. Saturation Transfer Difference NMR Reveals Functionally Essential Kinetic Differences for a Sugar-Binding Repressor Protein. *Chem. Commun.* **2009**, No. 39, 5862.

(56) Villar, H. O.; Yan, J.; Hansen, M. R. Using NMR for Ligand Discovery and Optimization. *Curr. Opin. Chem. Biol.* **2004**, *8* (4), 387–391.

(57) Dalvit, C.; Fasolini, M.; Flocco, M.; Knapp, S.; Pevarello, P.; Veronesi, M. NMR-Based Screening with Competition Water−Ligand Observed via Gradient Spectroscopy Experiments: Detection of High-Affinity Ligands. *J. Med. Chem.* **2002**, *45* (12), 2610–2614.

(58) Sánchez-Pedregal, V. M.; Reese, M.; Meiler, J.; Blommers, M. J. J.; Griesinger, C.; Carlomagno, T. The INPHARMA Method: Protein-Mediated Interligand NOEs for Pharmacophore Mapping. *Angew. Chem. Int. Ed.* **2005**, *44* (27), 4172–4175.

(59) Orts, J.; Tuma, J.; Reese, M.; Grimm, S. K.; Monecke, P.; Bartoschek, S.; Schiffer, A.; Wendt, K. U.; Griesinger, C.; Carlomagno, T. Crystallography-Independent Determination of Ligand Binding Modes. *Angew. Chem. Int. Ed.* **2008**, *47* (40), 7736–7740.

(60) Orts, J.; Griesinger, C.; Carlomagno, T. The INPHARMA Technique for Pharmacophore Mapping: A Theoretical Guide to the Method. *J. Magn. Reson.* **2009**, *200* (1), 64–73.

(61) Bartoschek, S.; Klabunde, T.; Defossa, E.; Dietrich, V.; Stengelin, S.; Griesinger, C.; Carlomagno, T.; Focken, I.; Wendt, K. U. Drug Design for G-Protein-Coupled Receptors by a Ligand-Based NMR Method. *Angew. Chem. Int. Ed.* **2010**, *49* (8), 1426–1429.

(62) Krimm, I. INPHARMA-Based Identification of Ligand Binding Site in Fragment-Based Drug Design. *MedChemComm* **2012**, *3* (5), 605.

(63) Bhat, R.; Berger, S. The 5S Subunit of Transcarboxylase Interacts with Free Biotin as Studied by Transferred-NOESY and Saturation Transfer Difference NMR. *Protein Pept. Lett.* **2008**, *15* (6), 624–629.

(64) Orts, J.; Bartoschek, S.; Griesinger, C.; Monecke, P.; Carlomagno, T. An NMR-Based Scoring Function Improves the Accuracy of Binding Pose Predictions by Docking by Two Orders of Magnitude. *J. Biomol. NMR* **2012**, *52* (1), 23–30.

(65) Fruth, M.; Plaza, A.; Hinsberger, S.; Sahner, J. H.; Haupenthal, J.; Bischoff, M.; Jansen, R.; Müller, R.; Hartmann, R. W. Binding Mode Characterization of Novel RNA Polymerase Inhibitors Using a Combined Biochemical and NMR Approach. *ACS Chem. Biol.* **2014**, *9* (11), 2656–2663.

(66) Korzhnev, D. M.; Kay, L. E. Probing Invisible, Low-Populated States of Protein Molecules by Relaxation Dispersion NMR Spectroscopy: An Application to Protein Folding. *Acc. Chem. Res.* **2008**, *41* (3), 442–451.

(67) Walinda, E.; Morimoto, D.; Sugase, K. Resolving Biomolecular Motion and Interactions by R_2 and $R_{1\rho}$ Relaxation Dispersion NMR. *Methods* **2018**, *148*, 28–38.

(68) Palmer, A. G.; Kroenke, C. D.; Patrick Loria, J. Nuclear Magnetic Resonance Methods for Quantifying Microsecond-to-Millisecond Motions in Biological Macromolecules. In *Methods in Enzymology*; Elsevier, 2001; Vol. 339, pp 204–238.

(69) Korzhnev, D. M.; Salvatella, X.; Vendruscolo, M.; Di Nardo, A. A.; Davidson, A. R.; Dobson, C. M.; Kay, L. E. Low-Populated Folding Intermediates of Fyn SH3 Characterized by Relaxation Dispersion NMR. *Nature* **2004**, *430* (6999), 586–590.

(70) Choy, W.-Y.; Zhou, Z.; Bai, Y.; Kay, L. E. An ^{15}N NMR Spin Relaxation Dispersion Study of the Folding of a Pair of Engineered Mutants of Apocytochrome b_{562}. *J. Am. Chem. Soc.* **2005**, *127* (14), 5066–5072.

(71) Vallurupalli, P.; Hansen, D. F.; Kay, L. E. Structures of Invisible, Excited Protein States by Relaxation Dispersion NMR Spectroscopy. *Proc. Natl. Acad. Sci.* **2008**, *105* (33), 11766–11771.

(72) Zintsmaster, J. S.; Wilson, B. D.; Peng, J. W. Dynamics of Ligand Binding from ^{13}C NMR Relaxation Dispersion at Natural Abundance. *J. Am. Chem. Soc.* **2008**, *130* (43), 14060–14061.

(73) Moschen, T.; Wunderlich, C. H.; Spitzer, R.; Levic, J.; Micura, R.; Tollinger, M.; Kreutz, C. Ligand-Detected Relaxation Dispersion NMR Spectroscopy: Dynamics of $PreQ_1$-RNA Binding. *Angew. Chem. Int. Ed.* **2015**, *54*, 560–563.

(74) Furukawa, A.; Konuma, T.; Yanaka, S.; Sugase, K. Quantitative Analysis of Protein–Ligand Interactions by NMR. *Prog. Nucl. Magn. Reson. Spectrosc.* **2016**, *96*, 47–57.

(75) Clore, G. M.; Iwahara, J. Theory, Practice, and Applications of Paramagnetic Relaxation Enhancement for the Characterization of Transient Low-Population States of Biological Macromolecules and Their Complexes. *Chem. Rev.* **2009**, *109* (9), 4108–4139.

(76) *Solution NMR of Paramagnetic Molecules: Applications to Metallobiomolecules and Models*; Bertini, I., Luchinat, C., Parigi, G., Eds.; Current methods in inorganic chemistry; Elsevier Science Ltd: Amsterdam ; New York, 2001.

(77) Iwahara, J.; Tang, C.; Marius Clore, G. Practical Aspects of ^{1}H Transverse Paramagnetic Relaxation Enhancement Measurements on Macromolecules. *J. Magn. Reson.* **2007**, *184* (2), 185–195.

(78) Hass, M. A.; Ubbink, M. Structure Determination of Protein–Protein Complexes with Long-Range Anisotropic Paramagnetic NMR Restraints. *Curr. Opin. Struct. Biol.* **2014**, *24*, 45–53.

(79) Clore, G. M. Interplay between Conformational Selection and Induced Fit in Multidomain Protein–Ligand Binding Probed by Paramagnetic Relaxation Enhancement. *Biophys. Chem.* **2014**, *186*, 3–12.

(80) Leung, I. K. H.; Flashman, E.; Yeoh, K. K.; Schofield, C. J.; Claridge, T. D. W. Using NMR Solvent Water Relaxation to Investigate Metalloenzyme−Ligand Binding Interactions. *J. Med. Chem.* **2010**, *53* (2), 867–875.

(81) Hoult, D. I.; Richards, R. E. The Signal-to-Noise Ratio of the Nuclear Magnetic Resonance Experiment. *J. Magn. Reson.* **1976**, *24* (1), 71–85.

(82) Kovacs, H.; Moskau, D.; Spraul, M. Cryogenically Cooled Probes—a Leap in NMR Technology. *Prog. Nucl. Magn. Reson. Spectrosc.* **2005**, *46* (2–3), 131–155.

(83) Moser, E.; Laistler, E.; Schmitt, F.; Kontaxis, G. Ultra-High Field NMR and MRI—The Role of Magnet Technology to Increase Sensitivity and Specificity. *Front. Phys.* **2017**, *5*.

(84) Bird, M. D.; Dixon, I. R.; Toth, J. Large, High-Field Magnet Projects at the NHMFL. *IEEE Trans. Appl. Supercond.* **2015**, *25* (3), 1–6.

(85) Plainchont, B.; Berruyer, P.; Dumez, J.-N.; Jannin, S.; Giraudeau, P. Dynamic Nuclear Polarization Opens New Perspectives for NMR Spectroscopy in Analytical Chemistry. *Anal. Chem.* **2018**, *90* (6), 3639–3650.

(86) Hu, K.-N.; Debelouchina, G. T.; Smith, A. A.; Griffin, R. G. Quantum Mechanical Theory of Dynamic Nuclear Polarization in Solid Dielectrics. *J. Chem. Phys.* **2011**, *134* (12), 125105.

(87) Keshari, K. R.; Wilson, D. M. Chemistry and Biochemistry of ^{13}C Hyperpolarized Magnetic Resonance Using Dynamic Nuclear Polarization. *Chem Soc Rev* **2014**, *43* (5), 1627–1659.

(88) Lee, Y. Dissolution Dynamic Nuclear Polarization–Enhanced Magnetic Resonance Spectroscopy and Imaging: Chemical and Biochemical Reactions in Nonequilibrium Conditions. *Appl. Spectrosc. Rev.* **2016**, *51* (3), 210–226.

(89) Zhang, G.; Hilty, C. Applications of Dissolution Dynamic Nuclear Polarization in Chemistry and Biochemistry. *Magn. Reson. Chem.* **2018**, *56* (7), 566–582.

(90) Bowen, S.; Hilty, C. Rapid Sample Injection for Hyperpolarized NMR Spectroscopy. *Phys. Chem. Chem. Phys.* **2010**, *12* (22), 5766.

(91) Chen, H.-Y.; Hilty, C. Implementation and Characterization of Flow Injection in Dissolution Dynamic Nuclear Polarization NMR Spectroscopy. *ChemPhysChem* **2015**, *16* (12), 2646–2652.

(92) Miéville, P.; Ahuja, P.; Sarkar, R.; Jannin, S.; Vasos, P. R.; Gerber-Lemaire, S.; Mishkovsky, M.; Comment, A.; Gruetter, R.; Ouari, O.; et al. Scavenging Free Radicals To Preserve Enhancement and Extend Relaxation Times in NMR Using Dynamic Nuclear Polarization. *Angew. Chem. Int. Ed.* **2010**, *49* (35), 6182–6185.

(93) Gajan, D.; Bornet, A.; Vuichoud, B.; Milani, J.; Melzi, R.; van Kalkeren, H. A.; Veyre, L.; Thieuleux, C.; Conley, M. P.; Gruning, W. R.; et al. Hybrid Polarizing Solids for Pure Hyperpolarized Liquids through Dissolution Dynamic Nuclear Polarization. *Proc. Natl. Acad. Sci.* **2014**, *111* (41), 14693–14697.

(94) Harris, T.; Bretschneider, C.; Frydman, L. Dissolution DNP NMR with Solvent Mixtures: Substrate Concentration and Radical Extraction. *J. Magn. Reson.* **2011**, *211* (1), 96–100.

(95) Eichhorn, T. R.; Takado, Y.; Salameh, N.; Capozzi, A.; Cheng, T.; Hyacinthe, J.-N.; Mishkovsky, M.; Roussel, C.; Comment, A. Hyperpolarization without Persistent

Radicals for in Vivo Real-Time Metabolic Imaging. *Proc. Natl. Acad. Sci.* **2013**, *110* (45), 18064–18069.

(96) Milani, J.; Vuichoud, B.; Bornet, A.; Miéville, P.; Mottier, R.; Jannin, S.; Bodenhausen, G. A Magnetic Tunnel to Shelter Hyperpolarized Fluids. *Rev. Sci. Instrum.* **2015**, *86* (2), 024101.

(97) Allouche-Arnon, H.; Hovav, Y.; Friesen-Waldner, L.; Sosna, J.; Moshe Gomori, J.; Vega, S.; Katz-Brull, R. Quantification of Rate Constants for Successive Enzymatic Reactions with DNP Hyperpolarized MR. *NMR Biomed.* **2014**, *27* (6), 656–662.

(98) Sadet, A.; Weber, E. M. M.; Jhajharia, A.; Kurzbach, D.; Bodenhausen, G.; Miclet, E.; Abergel, D. Rates of Chemical Reactions Embedded in a Metabolic Network by Dissolution Dynamic Nuclear Polarisation NMR. *Chem. - Eur. J.* **2018**, *24* (21), 5456–5461.

(99) Zeng, H.; Lee, Y.; Hilty, C. Quantitative Rate Determination by Dynamic Nuclear Polarization Enhanced NMR of a Diels−Alder Reaction. *Anal. Chem.* **2010**, *82* (21), 8897–8902.

(100) Chen, C.-H.; Shih, W.-C.; Hilty, C. *In Situ* Determination of Tacticity, Deactivation, and Kinetics in [*Rac*-(C_2H_4(1-Indenyl)$_2$)ZrMe][$B(C_6F_5)_4$] and [Cp_2ZrMe][$B(C_6F_5)_4$]-Catalyzed Polymerization of 1-Hexene Using ^{13}C Hyperpolarized NMR. *J. Am. Chem. Soc.* **2015**, *137* (21), 6965–6971.

(101) Harris, T.; Eliyahu, G.; Frydman, L.; Degani, H. Kinetics of Hyperpolarized $^{13}C_1$-Pyruvate Transport and Metabolism in Living Human Breast Cancer Cells. *Proc. Natl. Acad. Sci.* **2009**, *106* (43), 18131–18136.

(102) Dzien, P.; Fages, A.; Jona, G.; Brindle, K. M.; Schwaiger, M.; Frydman, L. Following Metabolism in Living Microorganisms by Hyperpolarized ^{1}H NMR. *J. Am. Chem. Soc.* **2016**, *138* (37), 12278–12286.

(103) Chen, H.-Y.; Ragavan, M.; Hilty, C. Protein Folding Studied by Dissolution Dynamic Nuclear Polarization. *Angew. Chem. Int. Ed.* **2013**, *52* (35), 9192–9195.

(104) Zierhut, M. L.; Yen, Y.-F.; Chen, A. P.; Bok, R.; Albers, M. J.; Zhang, V.; Tropp, J.; Park, I.; Vigneron, D. B.; Kurhanewicz, J.; et al. Kinetic Modeling of Hyperpolarized $^{13}C_1$-Pyruvate Metabolism in Normal Rats and TRAMP Mice. *J. Magn. Reson.* **2010**, *202* (1), 85–92.

(105) Harrison, C.; Yang, C.; Jindal, A.; DeBerardinis, R. J.; Hooshyar, M. A.; Merritt, M.; Dean Sherry, A.; Malloy, C. R. Comparison of Kinetic Models for Analysis of Pyruvate-to-Lactate Exchange by Hyperpolarized ^{13}C NMR. *NMR Biomed.* **2012**, *25* (11), 1286–1294.

(106) Gómez Damián, P. A.; Sperl, J. I.; Janich, M. A.; Khegai, O.; Wiesinger, F.; Glaser, S. J.; Haase, A.; Schwaiger, M.; Schulte, R. F.; Menzel, M. I. Multisite Kinetic Modeling of ^{13}C Metabolic MR Using [1-^{13}C]Pyruvate. *Radiol. Res. Pract.* **2014**, *2014*, 1–10.

(107) Hill, D. K.; Orton, M. R.; Mariotti, E.; Boult, J. K. R.; Panek, R.; Jafar, M.; Parkes, H. G.; Jamin, Y.; Miniotis, M. F.; Al-Saffar, N. M. S.; et al. Model Free Approach to Kinetic Analysis of Real-Time Hyperpolarized ^{13}C Magnetic Resonance Spectroscopy Data. *PLoS ONE* **2013**, *8* (9), e71996.

(108) Bastiaansen, J. A. M.; Cheng, T.; Mishkovsky, M.; Duarte, J. M. N.; Comment, A.; Gruetter, R. In Vivo Enzymatic Activity of AcetylCoA Synthetase in Skeletal

Muscle Revealed by ^{13}C Turnover from Hyperpolarized [1-^{13}C]Acetate to [1-^{13}C]Acetylcarnitine. *Biochim. Biophys. Acta BBA - Gen. Subj.* **2013**, *1830* (8), 4171–4178.

(109) Bowen, S.; Hilty, C. Temporal Chemical Shift Correlations in Reactions Studied by Hyperpolarized Nuclear Magnetic Resonance. *Anal. Chem.* **2009**, *81* (11), 4543–4547.

(110) Kim, Y.; Chen, C.-H.; Hilty, C. Direct Observation of Ru-Alkylidene Forming into Ethylene in Ring-Closing Metathesis from Hyperpolarized ^{1}H NMR. *Chem. Commun.* **2018**, *54* (34), 4333–4336.

(111) Lee, Y.; Heo, G. S.; Zeng, H.; Wooley, K. L.; Hilty, C. Detection of Living Anionic Species in Polymerization Reactions Using Hyperpolarized NMR. *J. Am. Chem. Soc.* **2013**, *135* (12), 4636–4639.

(112) Wang, Y.; Ragavan, M.; Hilty, C. Site Specific Polarization Transfer from a Hyperpolarized Ligand of Dihydrofolate Reductase. *J. Biomol. NMR* **2016**, *65* (1), 41–48.

(113) Wang, Y.; Hilty, C. Determination of Ligand Binding Epitope Structures Using Polarization Transfer from Hyperpolarized Ligands. *J. Med. Chem.* **2019**.

(114) Min, H.; Sekar, G.; Hilty, C. Polarization Transfer from Ligands Hyperpolarized by Dissolution Dynamic Nuclear Polarization for Screening in Drug Discovery. *ChemMedChem* **2015**, *10* (9), 1559–1563.

(115) Chappuis, Q.; Milani, J.; Vuichoud, B.; Bornet, A.; Gossert, A. D.; Bodenhausen, G.; Jannin, S. Hyperpolarized Water to Study Protein–Ligand Interactions. *J. Phys. Chem. Lett.* **2015**, *6* (9), 1674–1678.

(116) Kim, J.; Liu, M.; Hilty, C. Modeling of Polarization Transfer Kinetics in Protein Hydration Using Hyperpolarized Water. *J. Phys. Chem. B* **2017**, *121* (27), 6492–6498.

(117) Lee, Y.; Zeng, H.; Mazur, A.; Wegstroth, M.; Carlomagno, T.; Reese, M.; Lee, D.; Becker, S.; Griesinger, C.; Hilty, C. Hyperpolarized Binding Pocket Nuclear Overhauser Effect for Determination of Competitive Ligand Binding. *Angew. Chem. Int. Ed.* **2012**, *51* (21), 5179–5182.

(118) Liu, M.; Kim, Y.; Hilty, C. Characterization of Chemical Exchange Using Relaxation Dispersion of Hyperpolarized Nuclear Spins. *Anal. Chem.* **2017**, *89* (17), 9154–9158.

(119) Henzler-Wildman, K.; Kern, D. Dynamic Personalities of Proteins. *Nature* **2007**, *450* (7172), 964–972.

(120) Orozco, M. A Theoretical View of Protein Dynamics. *Chem Soc Rev* **2014**, *43* (14), 5051–5066.

(121) Guo, J.; Zhou, H.-X. Protein Allostery and Conformational Dynamics. *Chem. Rev.* **2016**, *116* (11), 6503–6515.

(122) Baldwin, A. J.; Kay, L. E. NMR Spectroscopy Brings Invisible Protein States into Focus. *Nat. Chem. Biol.* **2009**, *5* (11), 808–814.

(123) Loria, J. P.; Rance, M.; Palmer, A. G. A Relaxation-Compensated Carr−Purcell−Meiboom−Gill Sequence for Characterizing Chemical Exchange by NMR Spectroscopy. *J. Am. Chem. Soc.* **1999**, *121* (10), 2331–2332.

(124) Tollinger, M.; Skrynnikov, N. R.; Mulder, F. A. A.; Forman-Kay, J. D.; Kay, L. E. Slow Dynamics in Folded and Unfolded States of an SH3 Domain. *J. Am. Chem. Soc.* **2001**, *123* (46), 11341–11352.

(125) Hansen, D. F.; Vallurupalli, P.; Kay, L. E. Using Relaxation Dispersion NMR Spectroscopy to Determine Structures of Excited, Invisible Protein States. *J. Biomol. NMR* **2008**, *41* (3), 113–120.

(126) Eisenmesser, E. Z.; Millet, O.; Labeikovsky, W.; Korzhnev, D. M.; Wolf-Watz, M.; Bosco, D. A.; Skalicky, J. J.; Kay, L. E.; Kern, D. Intrinsic Dynamics of an Enzyme Underlies Catalysis. *Nature* **2005**, *438* (7064), 117–121.

(127) Korzhnev, D. M.; Neudecker, P.; Zarrine-Afsar, A.; Davidson, A. R.; Kay, L. E. Abp1p and Fyn SH3 Domains Fold through Similar Low-Populated Intermediate States. *Biochemistry* **2006**, *45* (34), 10175–10183.

(128) Neudecker, P.; Zarrine-Afsar, A.; Choy, W.-Y.; Muhandiram, D. R.; Davidson, A. R.; Kay, L. E. Identification of a Collapsed Intermediate with Non-Native Long-Range Interactions on the Folding Pathway of a Pair of Fyn SH3 Domain Mutants by NMR Relaxation Dispersion Spectroscopy. *J. Mol. Biol.* **2006**, *363* (5), 958–976.

(129) Neudecker, P.; Zarrine-Afsar, A.; Davidson, A. R.; Kay, L. E. Value Analysis of a Three-State Protein Folding Pathway by NMR Relaxation Dispersion Spectroscopy. *Proc. Natl. Acad. Sci.* **2007**, *104* (40), 15717–15722.

(130) Dubois, B. W.; Evers, A. S. ^{19}F-NMR Spin-Spin Relaxation (T_2) Method for Characterizing Volatile Anesthetic Binding to Proteins. Analysis of Isoflurane Binding to Serum Albumin. *Biochemistry* **1992**, *31* (31), 7069–7076.

(131) Sugase, K.; Dyson, H. J.; Wright, P. E. Mechanism of Coupled Folding and Binding of an Intrinsically Disordered Protein. *Nature* **2007**, *447* (7147), 1021–1025.

(132) Peuker, S.; Cukkemane, A.; Held, M.; Noé, F.; Kaupp, U. B.; Seifert, R. Kinetics of Ligand-Receptor Interaction Reveals an Induced-Fit Mode of Binding in a Cyclic Nucleotide-Activated Protein. *Biophys. J.* **2013**, *104* (1), 63–74.

(133) Demers, J.-P.; Mittermaier, A. Binding Mechanism of an SH3 Domain Studied by NMR and ITC. *J. Am. Chem. Soc.* **2009**, *131* (12), 4355–4367.

(134) Tolkatchev, D.; Xu, P.; Ni, F. Probing the Kinetic Landscape of Transient Peptide−Protein Interactions by Use of Peptide ^{15}N NMR Relaxation Dispersion Spectroscopy: Binding of an Antithrombin Peptide to Human Prothrombin. *J. Am. Chem. Soc.* **2003**, *125* (41), 12432–12442.

(135) Jóhannesson, H.; Denisov, V. P.; Halle, B. Dimethyl Sulfoxide Binding to Globular Proteins: A Nuclear Magnetic Relaxation Dispersion Study. *Protein Sci.* **1997**, *6* (8), 1756–1763.

(136) Kim, Y.; Liu, M.; Hilty, C. Parallelized Ligand Screening Using Dissolution Dynamic Nuclear Polarization. *Anal. Chem.* **2016**, *88* (22), 11178–11183.

(137) Lee, Y.; Zeng, H.; Ruedisser, S.; Gossert, A. D.; Hilty, C. Nuclear Magnetic Resonance of Hyperpolarized Fluorine for Characterization of Protein–Ligand Interactions. *J. Am. Chem. Soc.* **2012**, *134* (42), 17448–17451.

(138) Krieger, M.; Kay, L. M.; Stroud, R. M. Structure and Specific Binding of Trypsin: Comparison of Inhibited Derivatives and a Model for Substrate Binding. *J. Mol. Biol.* **1974**, *83* (2), 209–230.

(139) Koeppe, R. E.; Stroud, R. M. Mechanism of Hydrolysis by Serine Proteases: Direct Determination of the PKa's of Aspartyl-102 and Aspartyl-194 in Bovine Trypsin Using Difference Infrared Spectroscopy. *Biochemistry* **1976**, *15* (16), 3450–3458.

(140) Olaru, A. M.; Burns, M. J.; Green, G. G. R.; Duckett, S. B. SABRE Hyperpolarisation of Vitamin B3 as a Function of PH. *Chem. Sci.* **2017**, *8* (3), 2257–2266.

(141) Ban, D.; Mazur, A.; G. Carneiro, M.; Sabo, T. M.; Giller, K.; Koharudin, L. M. I.; Becker, S.; Gronenborn, A. M.; Griesinger, C.; Lee, D. Enhanced Accuracy of Kinetic Information from CT-CPMG Experiments by Transverse Rotating-Frame Spectroscopy. *J. Biomol. NMR* **2013**, *57* (1), 73–82.

(142) Liu, M.; Zhang, G.; Mahanta, N.; Lee, Y.; Hilty, C. Measurement of Kinetics and Active Site Distances in Metalloenzymes Using Paramagnetic NMR with ^{13}C Hyperpolarization. *J. Phys. Chem. Lett.* **2018**, *9* (9), 2218–2221.

(143) Ardenkjaer-Larsen, J.-H.; Boebinger, G. S.; Comment, A.; Duckett, S.; Edison, A. S.; Engelke, F.; Griesinger, C.; Griffin, R. G.; Hilty, C.; Maeda, H.; et al. Facing and Overcoming Sensitivity Challenges in Biomolecular NMR Spectroscopy. *Angew. Chem. Int. Ed.* **2015**, *54* (32), 9162–9185.

(144) Bowen, S.; Hilty, C. Time-Resolved Dynamic Nuclear Polarization Enhanced NMR Spectroscopy. *Angew. Chem. Int. Ed.* **2008**, *47* (28), 5235–5237.

(145) Iwahara, J.; Schwieters, C. D.; Clore, G. M. Characterization of Nonspecific Protein−DNA Interactions by ^{1}H Paramagnetic Relaxation Enhancement. *J. Am. Chem. Soc.* **2004**, *126* (40), 12800–12808.

(146) Iwahara, J.; Schwieters, C. D.; Clore, G. M. Ensemble Approach for NMR Structure Refinement against ^{1}H Paramagnetic Relaxation Enhancement Data Arising from a Flexible Paramagnetic Group Attached to a Macromolecule. *J. Am. Chem. Soc.* **2004**, *126* (18), 5879–5896.

(147) Ubbink, M.; Worrall, J. A. R.; Canters, G. W.; Groenen, E. J. J.; Huber, M. Paramagnetic Resonance of Biological Metal Centers. *Annu. Rev. Biophys. Biomol. Struct.* **2002**, *31* (1), 393–422.

(148) Bertini, I.; Luchinat, C.; Parigi, G.; Pierattelli, R. NMR Spectroscopy of Paramagnetic Metalloproteins. *ChemBioChem* **2005**, *6* (9), 1536–1549.

(149) Valdez, C. E.; Smith, Q. A.; Nechay, M. R.; Alexandrova, A. N. Mysteries of Metals in Metalloenzymes. *Acc. Chem. Res.* **2014**, *47* (10), 3110–3117.

(150) Schmitz, R. A.; Albracht, S. P. J.; Thauer, R. K. A Molybdenum and a Tungsten Isoenzyme of Formylmethanofuran Dehydrogenase in the Thermophilic Archaeon Methanobacterium Wolfei. *Eur. J. Biochem.* **1992**, *209* (3), 1013–1018.

(151) Huang, S.; Mahanta, N.; Begley, T. P.; Ealick, S. E. Pseudouridine Monophosphate Glycosidase: A New Glycosidase Mechanism. *Biochemistry* **2012**, *51* (45), 9245–9255.

(152) Preumont, A.; Snoussi, K.; Stroobant, V.; Collet, J.-F.; Van Schaftingen, E. Molecular Identification of Pseudouridine-Metabolizing Enzymes. *J. Biol. Chem.* **2008**, *283* (37), 25238–25246.

(153) Gasteiger, E.; Hoogland, C.; Gattiker, A.; Duvaud, S.; Wilkins, M. R.; Appel, R. D.; Bairoch, A. Protein Identification and Analysis Tools on the ExPASy Server.

In *The Proteomics Protocols Handbook*; Walker, J. M., Ed.; Humana Press: Totowa, NJ, 2005; pp 571–607.

(154) Kruk, D.; Kowalewski, J. Vibrational Motions and Nuclear Spin Relaxation in Paramagnetic Complexes: Hexaaquonickel(II) as an Example. *J. Chem. Phys.* **2002**, *116* (10), 4079–4086.

(155) Reuben, J.; Cohn, M. Magnetic Resonance Studies of Manganese (II) Binding Sites of Pyruvate Kinase. Temperature Effects and Frequency Dependence of Proton Relaxation Rates of Water. *J. Biol. Chem.* **1970**, *245* (24), 6539–6546.

(156) Powell, D. H.; Dhubhghaill, O. M. N.; Pubanz, D.; Helm, L.; Lebedev, Y. S.; Schlaepfer, W.; Merbach, A. E. Structural and Dynamic Parameters Obtained from ^{17}O NMR, EPR, and NMRD Studies of Monomeric and Dimeric Gd^{3+} Complexes of Interest in Magnetic Resonance Imaging: An Integrated and Theoretically Self-Consistent Approach[1]. *J. Am. Chem. Soc.* **1996**, *118* (39), 9333–9346.

(157) Liu, M.; Hilty, C. Metabolic Measurements of Nonpermeating Compounds in Live Cells Using Hyperpolarized NMR. *Anal. Chem.* **2018**, *90* (2), 1217–1222.

(158) Larive, C. K.; Barding, G. A.; Dinges, M. M. NMR Spectroscopy for Metabolomics and Metabolic Profiling. *Anal. Chem.* **2015**, *87* (1), 133–146.

(159) Shestov, A. A.; Mancuso, A.; Lee, S.-C.; Guo, L.; Nelson, D. S.; Roman, J. C.; Henry, P.-G.; Leeper, D. B.; Blair, I. A.; Glickson, J. D. Bonded Cumomer Analysis of Human Melanoma Metabolism Monitored by ^{13}C NMR Spectroscopy of Perfused Tumor Cells. *J. Biol. Chem.* **2016**, *291* (10), 5157–5171.

(160) Cavallari, E.; Carrera, C.; Aime, S.; Reineri, F. ^{13}C MR Hyperpolarization of Lactate by Using ParaHydrogen and Metabolic Transformation in Vitro. *Chem. - Eur. J.* **2017**, *23* (5), 1200–1204.

(161) Brindle, K. M. Imaging Metabolism with Hyperpolarized ^{13}C-Labeled Cell Substrates. *J. Am. Chem. Soc.* **2015**, *137* (20), 6418–6427.

(162) Golman, K.; in 't Zandt, R.; Thaning, M. Real-Time Metabolic Imaging. *Proc. Natl. Acad. Sci.* **2006**, *103* (30), 11270–11275.

(163) Lerche, M. H.; Jensen, P. R.; Karlsson, M.; Meier, S. NMR Insights into the Inner Workings of Living Cells. *Anal. Chem.* **2015**, *87* (1), 119–132.

(164) Lumata, L.; Yang, C.; Ragavan, M.; Carpenter, N.; DeBerardinis, R. J.; Merritt, M. E. Hyperpolarized ^{13}C Magnetic Resonance and Its Use in Metabolic Assessment of Cultured Cells and Perfused Organs. In *Methods in Enzymology*; Elsevier, 2015; Vol. 561, pp 73–106.

(165) Günther, U. L. Dynamic Nuclear Hyperpolarization in Liquids. In *Modern NMR Methodology*; Springer Berlin Heidelberg, 2011; Vol. 335, pp 23–69.

(166) Noinaj, N.; Buchanan, S. K. Structural Insights into the Transport of Small Molecules across Membranes. *Curr. Opin. Struct. Biol.* **2014**, *27*, 8–15.

(167) Karlsson, M.; Ardenkjær-Larsen, J. H.; Lerche, M. H. Hyperpolarized ^{133}Cs Is a Sensitive Probe for Real-Time Monitoring of Biophysical Environments. *Chem Commun* **2017**, *53* (49), 6625–6628.

(168) Casal, M.; Paiva, S.; Queirós, O.; Soares-Silva, I. Transport of Carboxylic Acids in Yeasts. *FEMS Microbiol. Rev.* **2008**, *32* (6), 974–994.

(169) Ruiz-Amil, M.; Fern□ndez, Ma. J.; Medrano, L.; Losada, M. Cellular Distribution of Yeast Pyruvate Decarboxylase, and Its Induction by Glucose. *Arch. F□r Mikrobiol.* **1966**, *55* (1), 46–53.

(170) Ozcan, S.; Johnston, M. Function and Regulation of Yeast Hexose Transporters. *Microbiol. Mol. Biol. Rev. MMBR* **1999**, *63* (3), 554–569.

(171) Meier, S.; Karlsson, M.; Jensen, P. R.; Lerche, M. H.; Duus, J. Ø. Metabolic Pathway Visualization in Living Yeast by DNP-NMR. *Mol. Biosyst.* **2011**, *7* (10), 2834.

(172) Pronk, J. T.; Yde Steensma, H.; Van Dijken, J. P. Pyruvate Metabolism in Saccharomyces Cerevisiae. *Yeast* **1996**, *12* (16), 1607–1633.

(173) Menichetti, L.; Frijia, F.; Flori, A.; Wiesinger, F.; Lionetti, V.; Giovannetti, G.; Aquaro, G. D.; Recchia, F. A.; Ardenkjaer-Larsen, J. H.; Santarelli, M. F.; et al. Assessment of Real-Time Myocardial Uptake and Enzymatic Conversion of Hyperpolarized [1-^{13}C]Pyruvate in Pigs Using Slice Selective Magnetic Resonance Spectroscopy. *Contrast Media Mol. Imaging* **2012**, *7* (1), 85–94.

(174) Yang, C.; Harrison, C.; Jin, E. S.; Chuang, D. T.; Sherry, A. D.; Malloy, C. R.; Merritt, M. E.; DeBerardinis, R. J. Simultaneous Steady-State and Dynamic ^{13}C NMR Can Differentiate Alternative Routes of Pyruvate Metabolism in Living Cancer Cells. *J. Biol. Chem.* **2014**, *289* (9), 6212–6224.

(175) Kokina, A.; Kibilds, J.; Liepins, J. Adenine Auxotrophy - Be Aware: Some Effects of Adenine Auxotrophy in *Saccharomyces Cerevisiae* Strain W303-1A. *FEMS Yeast Res.* **2014**, *14* (5), 697–707.

(176) Chattergoon, N.; Martínez-Santiesteban, F.; Handler, W. B.; Ardenkjaer-Larsen, J. H.; Scholl, T. J. Field Dependence of T_1 for Hyperpolarized [1-^{13}C]Pyruvate. *Contrast Media Mol. Imaging* **2013**, *8* (1), 57–62.

(177) Moret, S.; Dyson, P. J.; Laurenczy, G. Direct, in Situ Determination of PH and Solute Concentrations in Formic Acid Dehydrogenation and CO_2 Hydrogenation in Pressurised Aqueous Solutions Using ^{1}H and ^{13}C NMR Spectroscopy. *Dalton Trans.* **2013**, *42* (13), 4353.

(178) Seravalli, J.; Ragsdale, S. W. ^{13}C NMR Characterization of an Exchange Reaction between CO and CO_2 Catalyzed by Carbon Monoxide Dehydrogenase. *Biochemistry* **2008**, *47* (26), 6770–6781.

(179) Gietz, R. D.; Schiestl, R. H. High-Efficiency Yeast Transformation Using the LiAc/SS Carrier DNA/PEG Method. *Nat. Protoc.* **2007**, *2* (1), 31–34.

(180) Aune, T. E. V.; Aachmann, F. L. Methodologies to Increase the Transformation Efficiencies and the Range of Bacteria That Can Be Transformed. *Appl. Microbiol. Biotechnol.* **2010**, *85* (5), 1301–1313.

(181) Wang, Y.; Kahane, S.; Cutcliffe, L. T.; Skilton, R. J.; Lambden, P. R.; Clarke, I. N. Development of a Transformation System for Chlamydia Trachomatis: Restoration of Glycogen Biosynthesis by Acquisition of a Plasmid Shuttle Vector. *PLoS Pathog.* **2011**, *7* (9), e1002258.

(182) Li, Z.; Xu, J.; Jiang, T.; Ge, Y.; Liu, P.; Zhang, M.; Su, Z.; Gao, C.; Ma, C.; Xu, P. Overexpression of Transport Proteins Improves the Production of 5-Aminovalerate from l-Lysine in Escherichia Coli. *Sci. Rep.* **2016**, *6* (1).

(183) Wu, M.; Zhao, D.; Zhong, W.; Yan, H.; Wang, X.; Liang, Z.; Li, Z. High-Density Distributed Electrode Network, a Multi-Functional Electroporation Method for Delivery of Molecules of Different Sizes. *Sci. Rep.* **2013**, *3* (1).

(184) Wang, W.; Foley, K.; Shan, X.; Wang, S.; Eaton, S.; Nagaraj, V. J.; Wiktor, P.; Patel, U.; Tao, N. Single Cells and Intracellular Processes Studied by a Plasmonic-Based Electrochemical Impedance Microscopy. *Nat. Chem.* **2011**, *3* (3), 251–257.

(185) Van Nevel, S.; Koetzsch, S.; Weilenmann, H.-U.; Boon, N.; Hammes, F. Routine Bacterial Analysis with Automated Flow Cytometry. *J. Microbiol. Methods* **2013**, *94* (2), 73–76.

(186) Delorme, E. Transformation of Saccharomyces Cerevisiae by Electroporation. *Appl. Environ. Microbiol.* **1989**, *55* (9), 2242–2246.

(187) Ho, S. Y.; Mittal, G. S. Electroporation of Cell Membranes: A Review. *Crit. Rev. Biotechnol.* **1996**, *16* (4), 349–362.

(188) Thrivikraman, G.; Boda, S. K.; Basu, B. Unraveling the Mechanistic Effects of Electric Field Stimulation towards Directing Stem Cell Fate and Function: A Tissue Engineering Perspective. *Biomaterials* **2018**, *150*, 60–86.

(189) Dobson, C. M.; Hore, P. J. Kinetic Studies of Protein Folding Using NMR Spectroscopy. *Nat. Struct. Mol. Biol.* **1998**, *5*, 504–507.

(190) Hore, P. J.; Winder, S. L.; Roberts, C. H.; Dobson, C. M. Stopped-Flow Photo-CIDNP Observation of Protein Folding. *J. Am. Chem. Soc.* **1997**, *119* (21), 5049–5050.

(191) Foley, D. A.; Dunn, A. L.; Zell, M. T. Reaction Monitoring Using Online vs Tube NMR Spectroscopy: Seriously Different Results. *Magn. Reson. Chem.* **2016**, *54* (6), 451–456.

(192) Küster, S. K.; Danieli, E.; Blümich, B.; Casanova, F. High-Resolution NMR Spectroscopy under the Fume Hood. *Phys. Chem. Chem. Phys. PCCP* **2011**, *13* (29), 13172–13176.

(193) Khajeh, M.; Bernstein, M. A.; Morris, G. A. A Simple Flowcell for Reaction Monitoring by NMR. *Magn. Reson. Chem. MRC* **2010**, *48* (7), 516–522.

(194) Kakuta, M.; Jayawickrama, D. A.; Wolters, A. M.; Manz, A.; Sweedler, J. V. Micromixer-Based Time-Resolved NMR: Applications to Ubiquitin Protein Conformation. *Anal. Chem.* **2003**, *75* (4), 956–960.

(195) Frydman, L.; Lupulescu, A.; Scherf, T. Principles and Features of Single-Scan Two-Dimensional NMR Spectroscopy. *J. Am. Chem. Soc.* **2003**, *125* (30), 9204–9217.

(196) Villalonga, M. L.; Reyes, G.; Fragoso, A.; Cao, R.; Fernández, L.; Villalonga, R. Chemical Glycosidation of Trypsin with O-Carboxymethyl-Poly-β-Cyclodextrin: Catalytic and Stability Properties. *Biotechnol. Appl. Biochem.* **2005**, *41* (3), 217.